Multinucleon transfer reactions in the 238U+238U system studied with the VAMOS + AGATA + ID-Fix

Ablaihan Utepov

Normandie Université

THÈSE

Pour obtenir le diplôme de doctorat

Spécialité PHYSIQUE

Préparée au sein de l'Université de Caen Normandie

Multinucleon transfer reactions in the 238U+238U system studied with the VAMOS + AGATA + ID-Fix

Présentée et soutenue par
ABLAIHAN UTEPOV

Thèse soutenue le 21/04/2023 devant le jury composé de		
MME GIOVANNA MONTAGNOLI	Professeur des universités, PADOUE -UNIVERSITA DEGLI STUDI DI PADOVA	Rapporteur du jury
M. PETER REITER	Professeur des universités, KOLN UNIVERSITAT	Rapporteur du jury
M. DIEGO RAMOS	Chercheur, 14 GANIL de CAEN	Membre du jury
MME CHRISTELLE STODEL	Chargé de recherche, 14 GANIL de CAEN	Membre du jury Co-encadrante
MME BARBARA SULIGNANO	Chercheur HDR, CEA Paris-Saclay	Président du jury
M. DIETER ACKERMANN	Directeur de recherche, 14 GANIL de CAEN	Directeur de thèse

Thèse dirigée par DIETER ACKERMANN (Grand accélérateur national d'ions lourds)

UNIVERSITÉ CAEN NORMANDIE

ED 591 PSIME

GANIL laboratoire commun CEA/DRF spiral2 CNRS/IN2P3

Multinucleon transfer reactions in the ^{238}U + ^{238}U system studied with the VAMOS + AGATA + ID-Fix

Ablaihan Utepov

GANIL | University of Caen-Normandie

Contents

List of Figures

List of Tables

Acknowledgements

I am grateful to all of the people who have supported me throughout the period of my Ph.D. and contributed to the success of my work. First of all, I would like to express my deepest appreciation to my supervisors Dieter Ackermann and Christelle Stodel. I started working with them during the internship for my master degree. Their supervision, experience and personal approach during this time made me decide to apply for a Ph.D. at GANIL. There are no words to thank them enough for guiding me throughout all these years, for giving such a great opportunity to work on the subject, for an invaluable contribution to my practical skills and theoretical knowledge, for their enormous support and especially the times when it was not easy. I don't believe that one can find better supervisors than they are. I would also like to thank all the members of the jury, Giovanna Montagnoli, Peter Reiter, Barbara Sulignano and Diego Ramos Doval, for the time spent reading my manuscript and for agreeing to referee me. In particular, I would like to thank Giovanna and Peter for agreeing to be the reviewers of my manuscript. I am very grateful to the colleagues from the VAMOS and AGATA collaboration without whom the experiment would not be possible. I would like to thank, in particular, Diego for laying the foundation to my understanding of VAMOS++ and its data analysis. I would also like to thank Youngju for many fruitful discussions on analysis of the data. I am very thankful to the DAQ team, Charles, Fred, Patrice and Luc, for helping me with the NUMEXO2 digitizer and the data acquisition. My gratitude to Suzana Szilner for performing theoretical calculations for the interpretation of my data and I am thankful to Emily Lamour for transporting the targets for our experiment from GSI to GANIL. My special thanks to all the previous and current Ph.D. students and postdocs, Sylvain, Blaise-Maël, Panos, Valerian, Chloe, Armel, Julien, Quentin, Nishu, Hope, Jekabs, Alejandro, Vincent, Tom, Alexis, Jose, Anjali, Antoine, Marius, Abhilasha, Shayan. The last but not least, I would like to thank my parents and my wife for a continuous support throughout the Ph.D. period.

Chapter 1

Introduction

Since the middle of the last century many efforts have been devoted to investigate the region of heaviest nuclei and to explore the limits of the nuclear existence. Thanks to the advance of particle accelerators as well as detection techniques, experimental investigations turned out to be successful in the synthesis of new elements pushing the limits of the nuclide chart up to Z = 118. From the theoretical point of view, the existence of nuclei with a proton number higher than ∼100 is solely due to the underlying quantum shell structure, usually expressed as "shell effects", providing an enhanced stability to the nuclei. Without shell effects, these nuclei would undergo fission as the short range attractive nuclear force is not sufficiently strong to compensate the long range Coulomb repulsion.

The major success of the nuclear shell model was, being able to describe the occurrence of "magic" numbers or shell closures (2, 8, 20, 28, 50, 82, 126[1]) which are the numbers of protons or neutrons at which the nuclei have an increased binding energy with respect to the neighboring nuclei. Searching for the next magic or doubly-magic nuclei, various models predict the existence of the so-called "island of stability" of spherical superheavy nuclei (SHN). The predicted location, however, varies between models, such as microscopic-macroscopic and self-consistent models, having a large number of different parameterizations [AT17]. To constrain them, detailed spectroscopic studies of lighter deformed nuclei, serving as a gateway to SHN, could provide valuable information on the properties of the heaviest nuclei. In particular, spectroscopic studies of nuclei in the region of neutron-rich light actinides would allow to understand better the properties of the N = 152 deformed shell gap and could shed light on its possible termination for atomic charges below Z = 96 which could not be addressed so far.

The main obstacle in experimental studies of neutron-rich light actinide nuclei, and also the

[1] the shell closure at 126 was observed for neutrons only

neutron-rich ones in the region of SHN, is the production mechanism. The fusion-evaporation reaction, being so far successful in synthesis of SHN, faces significant limitations caused by low production cross sections, which tend to decrease with increasing Z, and the lack of sufficiently neutron-rich projectile-target combinations. An alternative way to approach this region has been proposed via the employment of multinucleon transfer (MNT) reactions for which rather high cross sections were predicted in deep-inelastic collisions of heavy ions at energies near the Coulomb barrier [ZOIG06, ZG13]. In an early investigation of MNT processes, the production of isotopes from Pu to Fm was observed in ^{238}U + ^{238}U/^{248}Cm reactions via radiochemical separation techniques with cross section values ranging from mbarn to nbarn [SKA+78, SBG+82, KSG13]. The neutron-rich part of these isotopes reaches into close vicinity of N = 152. In 2006, MNT investigations in the ^{238}U + ^{238}U reaction were performed with the VAMOS magnetic spectrometer [GHM+10]. The measurement at five different beam energies indicated the observation of a massive transfer of nucleons. However, no reaction products heavier than uranium were identified, due to the limited resolving power in mass and atomic charge.

Motivated by the refined experimental conditions, i.e. improved mass resolution of $\Delta A/A \simeq 1/263$ [RGS+17] achieved recently at the magnetic spectrometer VAMOS++, the present thesis addresses the experimental challenges related to the production as well as the identification of neutron-rich light actinide nuclei near the N = 152 deformed shell gap. It aims, in particular, at the measurement of MNT cross sections in the ^{238}U + ^{238}U reaction, which is intended to serve as a basis for possible future nuclear structure studies. VAMOS++ was used to identify the atomic mass of the products [RLN+11, RGS+17]. To determine the atomic number of the products, coincident x-rays were detected with the γ-ray spectrometer AGATA [AAA+12, CMd+17, KL19] together with the x-ray detector array of 3 LEPS detectors named as ID-Fix. This thesis is organized in the following way:

Chapter 1 Introduction The scope of the present work is defined, presenting an overview of the main points of the thesis.

Chapter 2 Physics Background Different theoretical models are introduced employed for the description of nuclear structure. Various processes taking place in nuclear reactions near the Coulomb barrier are described, particularly focusing on MNT reactions. The current knowledge on the neutron-rich light actinide nuclei along N = 152 is discussed, outlining the physical motivations for the experiment.

Chapter 3 Experimental Devices The details of the experiment are presented, including the properties of the beam, the targets and the employed detection setup consisting of the unique combination of VAMOS, AGATA and ID-Fix.

Chapter 4 Tests of the ID-Fix array The work done for preparation of the ID-Fix array is reported, in terms of absorber studies for an efficient photon background suppression, stem-

ming from the ^{238}U+^{238}U reaction, and optimization of the digital pulse processing for an efficient x-ray spectroscopy.

Chapter 5 Data Analysis The analysis of the collected data is described together with the calibration of the detectors and determination of the atomic mass and the atomic charge of the reaction products.

Chapter 6 Results and Discussion The obtained results are discussed based on the extracted yields of the products.

Chapter 7 Conclusion and Outlook The present work is concluded, presenting an outlook for future experiments.

Introduction (version française)

Depuis le milieu du siècle dernier, de nombreux efforts ont été consacrés à l'étude de la région des noyaux les plus lourds et à l'exploration des limites de l'existence nucléaire. Grâce aux progrès des accélérateurs de particules et des techniques de détection, les recherches expérimentales se sont avérées fructueuses pour la synthèse de nouveaux éléments repoussant les limites du tableau des nucléides jusqu'à Z = 118. D'un point de vue théorique, l'existence de noyaux dont le nombre de protons est supérieur à $\sim$100 est uniquement due à la structure quantique en couche sous-jacente, généralement exprimée par les "effets de couche", qui confère une stabilité accrue aux noyaux. Sans les effets de couche, ces noyaux se désintégreraient par fission car la force nucléaire attractive à courte portée n'est pas suffisamment forte pour compenser la répulsion de Coulomb à longue portée.

Le principal succès du modèle en couches nucléaires a été de pouvoir décrire l'apparition de nombres "magiques" ou de fermetures de couches (2, 8, 20, 28, 50, 82, 126[2]), qui sont les nombres de protons ou de neutrons pour lesquels les noyaux ont une énergie de liaison accrue par rapport aux noyaux voisins. À la recherche des prochains noyaux magiques ou doublement magiques, divers modèles prédisent l'existence de ce que l'on appelle "ilôt de stabilité" des noyaux superlourds sphériques (SHN). Sa localisation prédite varie toutefois d'un modèle à l'autre, tels les modèles microscopiques-macroscopiques et auto-cohérents, qui présentent un grand nombre de paramétrisations différentes [AT17]. Pour les contraindre, des études spectroscopiques détaillées de noyaux déformés plus légers, servant de portail vers les SHN, pourraient fournir des informations précieuses sur les propriétés des noyaux les plus lourds. En particulier, les études spectroscopiques des noyaux dans la région des actinides légers riches en neutrons permettraient de mieux comprendre les propriétés de la couche déformée N = 152 et pourraient mettre en lumière son éventuelle disparition pour les charges atomiques inférieures à Z = 96, ce qui n'a pas pu être étudié jusqu'à présent.

Le principal obstacle aux études expérimentales des noyaux d'actinides légers riches en neutrons, ainsi que des noyaux riches en neutrons dans la région des SHN, est le mécanisme de pro-

[2]la fermeture de couche à 126 a été observée pour les neutrons uniquement

duction. La réaction de fusion-évaporation, qui a jusqu'à présent permis de synthétiser des SHN, est confrontée à des limitations importantes dues à des sections efficaces de production faibles, qui tendent à diminuer avec l'augmentation de Z, et au manque de combinaisons projectile-cible suffisamment riches en neutrons. Une autre façon d'approcher cette région a été proposée en utilisant des réactions de transfert de multinucléons (MNT) pour lesquelles des sections efficaces assez élevées ont été prédites dans des collisions inélastiques profondes d'ions lourds à des énergies proches de la barrière de Coulomb [ZOIG06, ZG13]. Lors d'une première étude des processus MNT, la production d'isotopes de Pu à Fm a été observée dans des réactions ^{238}U + ^{238}U/^{248}Cm via des techniques de séparation radiochimique avec des valeurs de section efficace allant du mbarn à nbarn [SKA+78, SBG+82, KSG13]. La région riche en neutrons de ces isotopes est proche de N = 152. En 2006, des études sur les MNT dans la réaction ^{238}U + ^{238}U ont été réalisées avec le spectromètre magnétique VAMOS [GHM+10]. Les mesures effectuées à cinq énergies de faisceau différentes ont permis d'observer un transfert massif de nucléons. Cependant, aucun produit de réaction plus lourd que l'uranium n'a été identifié, en raison du pouvoir de résolution limité en masse et charge atomique.

Motivé par les conditions expérimentales perfectionnées, i.e. résolution en masse améliorée à $\Delta A/A \simeq 1/263$ [RGS+17] obtenue récemment avec le spectromètre magnétique VAMOS++, La présente thèse aborde les défis expérimentaux liés à la production et à l'identification de noyaux d'actinides légers riches en neutrons près de la couche déformée N = 152. Elle vise notamment à mesurer les sections efficaces des MNT dans la réaction ^{238}U + ^{238}U, ce qui devrait servir de base à d'éventuelles futures études de structure nucléaire. VAMOS++ a été utilisé pour identifier la masse atomique des produits [RLN+11, RGS+17]. Pour déterminer le numéro atomique des produits, des rayonnements X en coïncidence ont été détectés avec le spectromètre AGATA [AAA+12, CMd+17, KL19] et l'ensemble de 3 détecteurs LEPS appelé ID-Fix. Cette thèse est organisée de la manière suivante :

Chapter 1 Introduction Le cadre de ce travail est défini, présentant une vue d'ensemble des principaux points de la thèse.

Chapter 2 Contexte Physique Différents modèles théoriques sont présentés pour décrire la structure nucléaire. Divers processus se déroulant dans les réactions nucléaires près de la barrière de Coulomb sont décrits, avec un accent particulier sur les réactions MNT. Les connaissances actuelles sur les noyaux d'actinides légers riches en neutrons le long de N = 152 sont discutées, en soulignant les motivations physiques de l'expérience.

Chapter 3 Dispositifs Experimentaux Les détails de l'expérience sont présentés, y compris les propriétés du faisceau, les cibles et le dispositif de détection utilisé, qui consiste en une combinaison unique de VAMOS, AGATA et ID-Fix.

Chapter 4 Tests du dispositif ID-Fix Le travail effectué pour la préparation du dispositif ID-Fix est rapporté, en termes d'études d'absorbeurs pour une suppression efficace du bruit de fond

des photons, provenant de la réaction ^{238}U + ^{238}U, et l'optimisation du traitement numérique des signaux pour une spectroscopie des rayonnements X performante.

Chapter 5 Analyse des données L'analyse des données recueillies est décrite, ainsi que l'étalonnage des détecteurs et la détermination en masse et charge atomique des produits de la réaction.

Chapter 6 Résultats et Discussion Les résultats obtenus sur les taux de production des produits sont discutés.

Chapter 7 Conclusion et perspectives Après une conclusion sur le présent travail, des perspectives sur de futures expériences sont présentées

Chapter 2

Physics Background

Contents

2.1 Introduction

In this chapter, the physics background of the present work is presented. Firstly, the theoretical background in terms of models describing the structure of the nucleus is discussed. Secondly, general features of nuclear reactions taking place in collisions of heavy nuclei at energies near the Coulomb barrier are presented. In particular, the previous investigations of multinucleon transfer reactions will be discussed.

2.2 Nuclear structure models

A number of various theoretical models were developed for the description of the properties of the nucleus. These include the liquid drop model accounting for the macroscopic nature of nuclei like binding energy and shape, the shell model explaining the microscopic features such as single particle energies and mean-field models which come in forms of macroscopic-microscopic models and self-consistent mean-field models. This section provides a brief overview of each of these models.

2.2.1 Liquid-drop model

The liquid-drop model (LDM) is one of oldest models used to describe the atomic nucleus. The LDM was first proposed by Gamow in 1930 [Gam30], and was further extended over years. It treats the nucleus as a charged sphere of high-density incompressible fluid. It can predict the binding energy, given by the difference between the mass of the nucleus and the total mass of each of its constituents, and the fission barriers to a certain extent.

The binding energy (BE(A,Z)) of the nucleus with the atomic mass A, the atomic charge Z and the neutron number N is calculated using the Bethe-Weizsäcker semi-empirical mass formula [Wei35] as follows

$$\mathrm{BE(A,Z)} = \mathrm{a_V A} - \frac{\mathrm{a_C Z^2}}{\mathrm{A^{1/3}}} - \mathrm{a_S A^{2/3}} - \frac{\mathrm{a_A (N-Z)^2}}{\mathrm{A}} + \delta(\mathrm{A,Z}) \tag{2.1}$$

with

$$\delta(\mathrm{A,Z}) = \begin{cases} +\delta & \text{for even Z, N} \\ 0 & \text{for odd A} \\ -\delta & \text{for odd Z, N} \end{cases} \tag{2.2}$$

where

- $\mathrm{a_V A}$ is the volume term which stands for the short range strong nuclear force attracting equally all the involved nucleons A,

- $\frac{a_C Z^2}{A^{1/3}}$ is the Coulomb term which is due to the electrostatic repulsion of the positively charged protons,
- $a_S A^{2/3}$ is the surface term which refers to the correction, to the volume term $a_V A$, required since the surface nucleons are not equally attracted and only weakly bound together from the inside,
- $\frac{a_A (N-Z)^2}{A}$ is the assymetry term which accounts for the quantum nature of the nucleons associated with the Pauli exclusion principle,
- $\delta(A, Z)$ is the pairing term which corresponds to the pairing of the nucleons.

The LDM succeeded in describing the deviation of the valley of stability from the N = Z to more neutron rich nuclei. However, it failed to describe the experimental data in the region near the shell closures and for heavy nuclei for which the fission barrier vanishes.

2.2.2 Nuclear shell model

The development of the nuclear shell model was motivated by the observation of the "magic" numbers of nucleons (2, 8, 20, 28, 50, 82, 126[3]) for which nuclei exhibit an enhanced stability compared to their neighbors, which the LDM described in the previous section fails to reproduce. The model was developed in analogy of the atomic shell model which describes the properties of an atom, experiencing an enhanced stability if its electronic shell is filled, based on the configuration of its electrons orbiting in external potential created by the nucleus. In contrast, the nuclear shell model, using the Pauli exclusion principle, treats the nucleons that are moving independently in a mean central potential ($V(r)$) generated by themselves. However, these early assumptions were unable to account for the occurence of the "magic" numbers and only in 1949 M. Goeppert-Mayer, E. P. Wigner, and J. Hans D. Jensen [May49, May50, HJS49] could explain them by introducing a strong spin-orbit splitting term ($\vec{l} \cdot \vec{s}$) in the mean central potential $V(r)$:

$$V = V(r) + V_{ls}(r)(\vec{l} \cdot \vec{s}) \tag{2.3}$$

In this way, the model was able to predict the properties of the spherical nuclei including ground-state and excited-state spin and parities, isomeric states, magnetic moments. However, it could not predict the behavior of nuclei with permanent deformation which are far from the shell closures. The properties of the deformed nuclei was later explained by Nilsson in 1955 which was a major step towards understanding the entire nuclide chart [Nil55].

2.2.3 Microscopic-macroscopic model

The models described in the previous two sections have their advantages and shortcomings. The LDM allows to calculate the bulk (macroscopic) properties of the nucleus in terms of binding en-

[3] the shell closure at 126 was observed for neutrons only

ergies, masses and fission barriers but it cannot account for the single particle energies while the shell model allows to reproduce the single particle (microscopic) energies but it is too complicated to describe the bulk properties of the nucleus with many nucleons due to the high computational effort needed. To account properly for both microscopic and macroscopic parts, hence the microscopic-macroscopic model, Strutinsky combined these two models [Str67]. In this model, the total energy of the nucleus is calculated as

$$\mathrm{E_{tot}} = \mathrm{E_{LD}} + \mathrm{E_{sh}(protons)} + \mathrm{E_{sh}(neutrons)} \tag{2.4}$$

where $\mathrm{E_{LD}}$ is an average total energy obtained using the LDM, $\mathrm{E_{sh}}$ is a shell correction energies for protons and neutrons which is determined by the difference between the sum over discrete energy levels (g) of the shell model and a smeared ($\tilde{\mathrm{g}}$) energy function of the LDM in the same energy range which are given by

$$\mathrm{g(e)} = \sum_{\mathrm{i}} \delta(\mathrm{e} - \mathrm{e_i}) \tag{2.5}$$

and

$$\tilde{\mathrm{g}}(\mathrm{e}) = \frac{1}{\gamma\pi} \sum_{\mathrm{i}} \mathrm{f_{corr}}(\frac{\mathrm{e} - \mathrm{e_i}}{\gamma}) \mathrm{exp}(-\frac{(\mathrm{e} - \mathrm{e_i})^2}{\gamma^2}) \tag{2.6}$$

where e is the single particle energies, $\mathrm{e_i}$ is the average behavior of the nucleus, $\gamma = \hbar\omega_0$ denotes the value for the Fermi energy and is the shell spacing with the oscillator frequency for the spherical harmonic oscillator ω_0, and $\mathrm{f_{corr}}$ is a correction function keeping the long range variations unchanged. Finally, the shell correction energy $\mathrm{E_{sh}}$ is given as

$$\mathrm{E_{sh}} = 2\sum \mathrm{e_i} - 2\int \mathrm{e}\tilde{\mathrm{g}}\mathrm{de}. \tag{2.7}$$

A negative shell correction energy leads to the decreased total energy of the nucleus and an increased binding energy resulting in a more stable nucleus. The shell corrections across the whole nuclide chart is shown in Figure 2.1. One can note that the shell correction energies for the spherical nuclei is negative. Most macroscopic-microscopic calculations predict the next spherical magic numbers to be Z = 114 and N = 184 [SP07]. However, the modification of calculations parameters for single-particle energies can close the Z = 114 gap and open up a gap at 126 instead [BH13].

For deformed nuclei, the calculations show clear effects of shell stabilization at N = 152 and 162 [SMP01, PSAS89]. In particular for N = 152, which lies in the region of our interest, the effects of the deformed subshell closure can be observed from systematics of the first excited 2^+ state energies, which is a good probe to reveal the shell effects of deformed nuclei, of even-even nuclei from U to No from both experimental and theoretical points of view as shown in Figure 2.2. One has to note that for several isotopes the 2^+ state energies were determined via a "Harris" fit to the extracted moments of inertia of higher spin data of the rotational band as it is not possible to directly measure the energies due to internal conversion [TGK+15]. From the theoretical values,

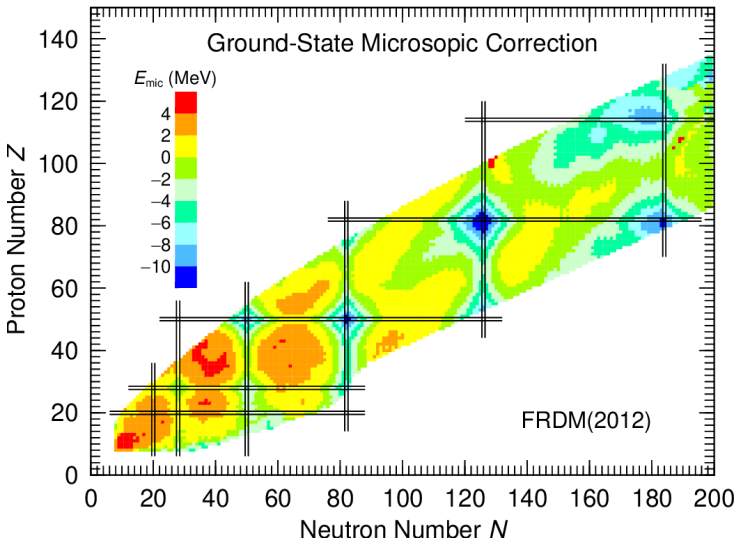

Figure 2.1: Ground-state shell (microscopic) corrections [MSIS16]. Most macroscopic-microscopic models predict the magic numbers of Z = 114 and N = 184 for the island of stability of superheavy nuclei [SP07].

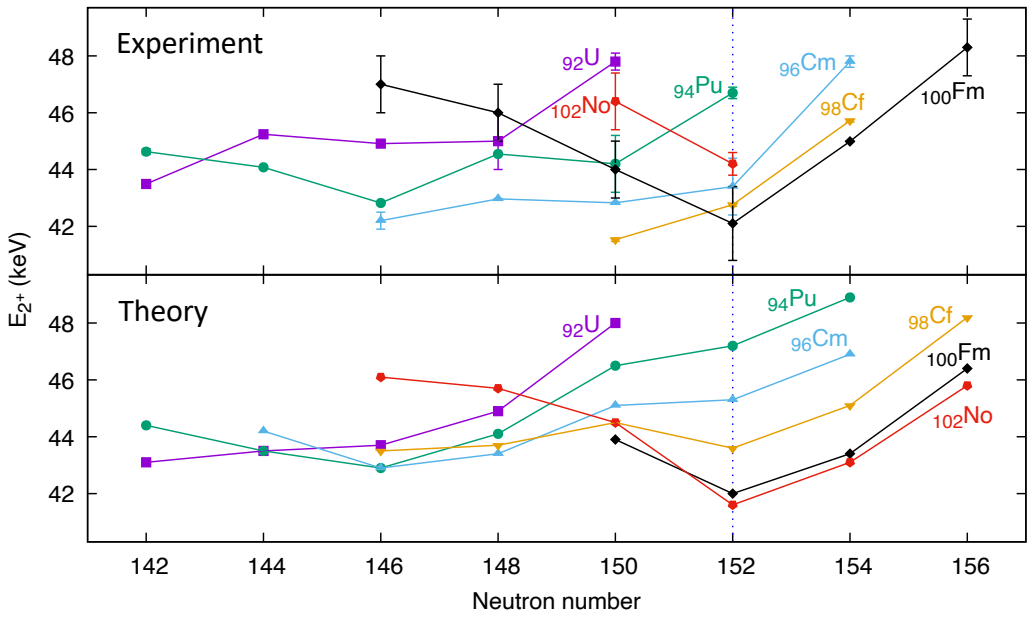

Figure 2.2: Experimental [nnd, ATK+16] (top) and calculated [SMP01] (bottom) energies of the first excited 2^+ states of even-even isotopes of actinide nuclei from U to No. The lines are drawn to guide the eye.

the behavior is rather regular with a decrease in energy at N = 152 indicating the shell stabilization. From the experimental values, the character of the double deformed shell closure is indicated at Z = 100 and N = 152. The values for isotopes from Cm to No are pulled down to lower energies at N = 152. In contrast, the values for Pu isotopes increase gradually with neutron number. This suggests, as discussed in Ref. [MIA+07] by H. Makii *et al.*, that the deformed shell-gap size at N = 152 is considerably reduced for Pu isotopes. For U isotopes, there is no data available at N = 152 which would help to clarify the situation and would allow to shed light on the possible termination of the N = 152 deformed subshell closure.

2.2.4 Self-consistent mean-field models

Self-consistent mean-field models provide powerful tools to study the properties of nuclei. In contrast to the shell model, these models are unprejudiced self-consistent concerning the structure or shape of nuclei without using any phenomenological potential. They, instead, determine the mean field of a nucleus by employing an effective interaction and a self-consistent approach like the Hartree-Fock or the Hartree-Fock-Bogoliubov method. Detailed description of the models can be found in the review of M. Bender *et al.* [BHR03].

Various effective interactions are chosen for the description of nuclear properties over the whole nuclear chart. The most widely used ones are the non-relativistic contact Skyrme and finite-range Gogny interactions as well as relativistic mean-fields (RMF) that are also called covariant density functional theory (CDFT) [BH13, BHR03, VALR05]. Within each of them a large number of parameterizations of the effective interactions are used, predicting a more extended shell stabilization region, as shown in Figure 2.3, centered around Z = 114 - 126 and N = 172/184 [BNR01].

Within the CDFT framework, A. Afanasjev *et al.* [Afa14] performed systematic investigations of pairing and normally deformed rotational bands of even-even and odd-mass actinide and trans-actinide nuclei and could observe the occurrence of an alignment which takes place when a few nucleon pairs, having an angular momentum of zero, are broken under the influence of rotation. In particular, the alignment is observed for ^{242,244}Pu, ^{246,250}Cm and ^{250}Cf as shown in Figure 2.4 (top). For the heaviest uranium isotopes, this feature was also observed for ^{240}U as shown in Figure 2.4 (bottom), for which B. Birkenbach *et al.* [BVG+15] could measure a rotational band up to 20^+ level. For ^{242}U, although T. Ishii *et al.* [IMA+07] could establish a rotational band up to 8^+ level, to draw any conclusions high spin data is necessary and is still missing. Moreover, for ^{248}Cm, Th, and light U and Pu isotopes the alignment is not present, not allowing to identify any systematic trends.

A summary of the current knowledge of neutron-rich light actinide nuclei from U to Lr is provided in Figure 2.5. The color code indicates the amount of knowledge for a particular isotope. The region of neutron-rich light actinide nuclei along N = 152 of interest of the present work is

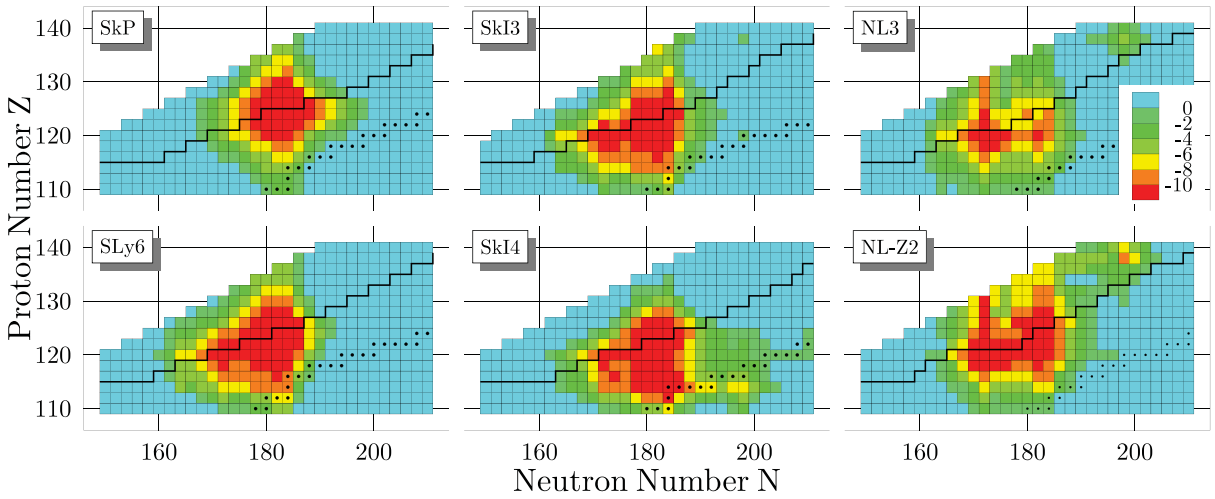

Figure 2.3: Total shell correction (sum of proton and neutron shell corrections; in MeV) calculated, with different parametrizations of effective interactions, for spherical even–even nuclei. Shell stabilitization extending in a large region around magic numbers indicate that the island of stability is soft [BNR01].

indicated. As one can see a rather limited amount of information is available for the nuclei in this region. Therefore, it is highly desirable to perform spectroscopic studies of these nuclei and to understand their properties which could serve as a valuable input for both theoretical and experimental investigations. However, one first has to answer the question of how to produce these difficult to access neutron-rich nuclei.

2.3 Nuclear reactions near the Coulomb barrier

Nuclear reactions represent a complex quantum mechanical process which occurs in collisions of two nuclei. The first nuclear reaction experiment in the laboratory was conducted in 1919 by E. Rutherford [F.R19]. In this experiment, a gas of ^{14}N was bombarded with α particles which, as inferred by Rutherford, resulted in a disruption of ^{14}N emitting ^{1}H nuclei and α particles. Only later in 1925, P. M. S. Blackett and E. Rutherford demonstrated through condensation chamber photographs that the α particles were absorbed by the ^{14}N nuclei leading to the emission of ^{1}H and ^{16}O instead [BR25]. In this way, the reaction mechanism of the first nuclear reaction was revealed. Since then, both experimental and theoretical research of nuclear reactions evolved attracting the interest of many physicists into understanding the reaction mechanism of collisions of heavy-ions with masses up to uranium.

Depending on the observable, nuclear reactions can be classified by involved masses, kinetic

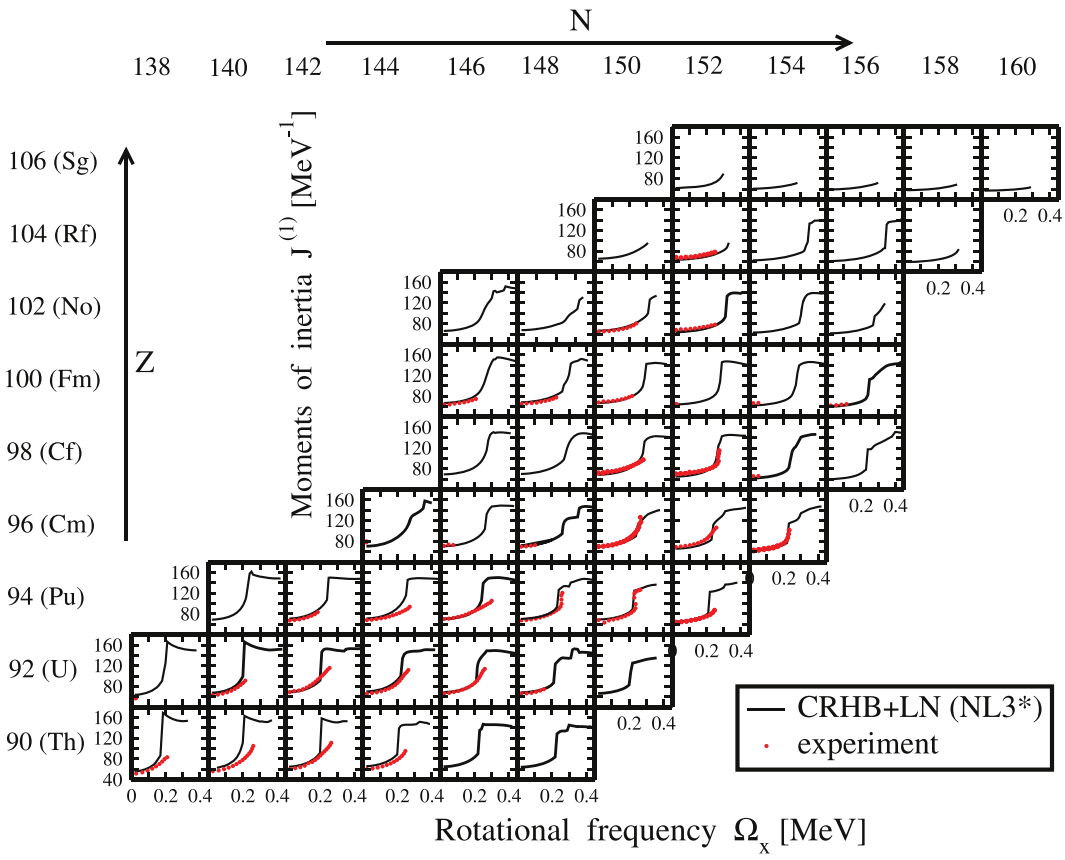

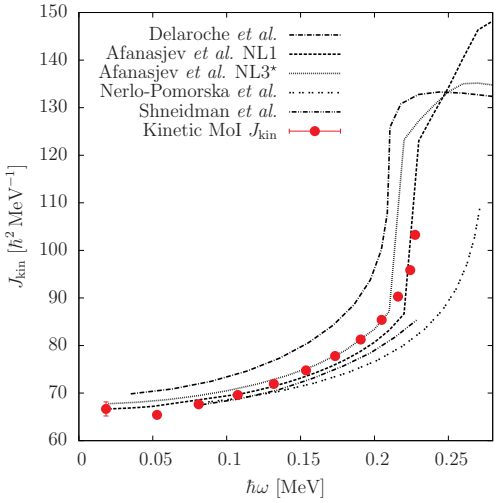

Figure 2.4: Evolution of the calculated and measured moments of inertia as a function of rotational frequency for even–even nuclei from Th-Sg [Afa14] (top) and for ^{240}U nuclei Bottom: [BVG+15] (bottom).

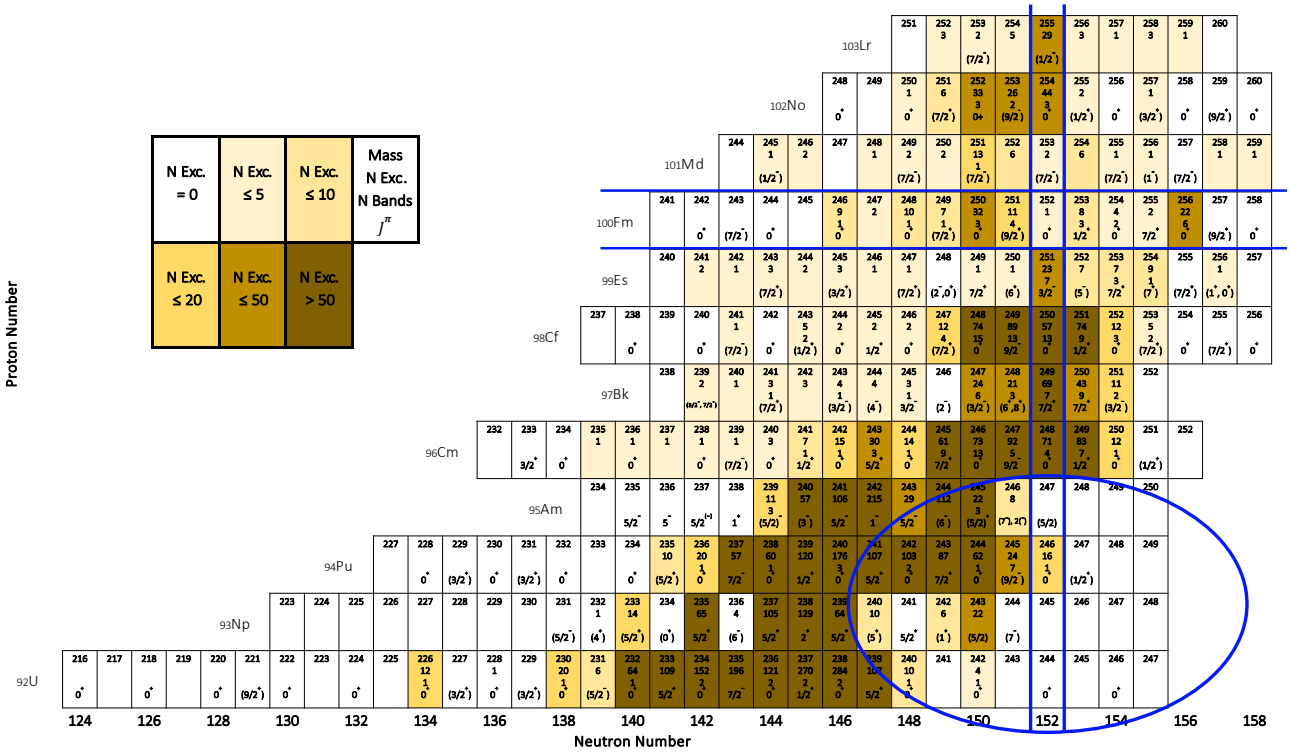

Figure 2.5: Currently available experimental data for actinide nuclei from U to Lr. For each of the isotopes, the values in the first, the second, the third and the forth rows stand for the mass number, the number of known excited levels, the number of assigned rotational bands and the ground state spin, respectively. The color code indicates the amount of knowledge for a particular isotope. The blue straight lines outline the deformed shell closures. The region in blue circle is a region of interest of the present work. The figure is an updated and extended, with Am to U [nnd], version of Figure 1 from Ref. [TGK+15].

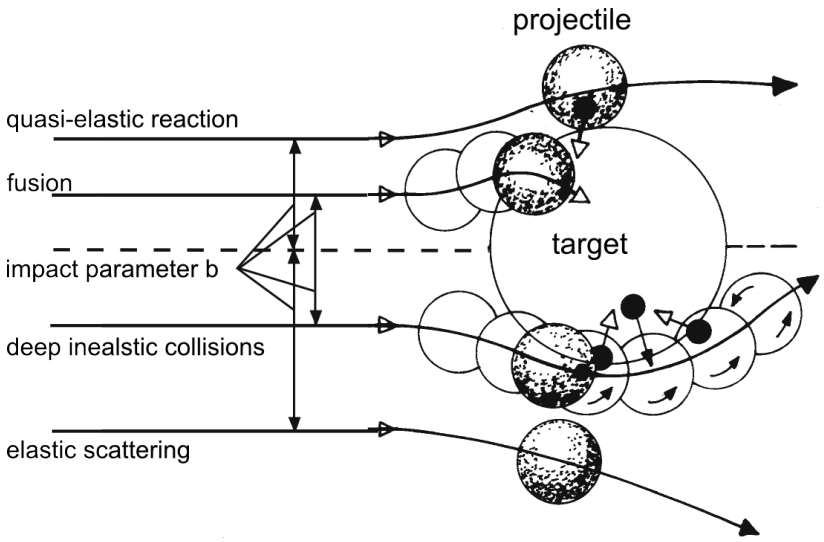

Figure 2.6: Classification of the reaction mechanisms in collisions of heavy-ions at energies around the Coulomb barrier as a function of impact parameter [BWW08]. Increasing the impact parameter, the interaction of heavy-ions evolves from fusion reactions, through deep inelastic processes, to quasi-elastic reactions. The elastic scattering dominates for distant collisions where nuclei feel only the Coulomb force.

energies, interaction times, impact parameters and transferred angular momentum [Bas80]. A simplified illustration of the various reaction mechanisms in heavy-ion collisions at energies in the vicinity of the Coulomb barrier as a function of impact parameter is shown in Figure 2.6. As the impact parameter increases, the evolution of the interaction between heavy-ions proceeds from fusion reactions, through deep inelastic processes, to quasi-elastic reactions with the elastic scattering dominating at distant collisions. In the following, the main properties of each of them will be described.

In **elastic** scattering reactions, the internal structure of the projectile and the target remains unchanged. The kinetic energy of the nuclei in the center-of-mass-frame is preserved. Among the different open reaction channels, the elastic scattering is typically the dominant one. It follows the Rutherford scattering, which is the elastic scattering of charged particles due to the Coulomb interaction, up to a certain angle of emission called the grazing angle. At the grazing angle the deviation from the Rutherford scattering starts indicating that the nuclear interaction becomes predominant with respect to the Coulomb interaction. With the same identity of the projectile and the target, one should consider the Mott scattering which is the elastic scattering due to the nuclear interaction leading to the interference of the cross section as a function of scattering angle caused by the quantum effects as shown in Figure 2.7. The aforementioned grazing angle is defined as the scattering angle when the distance

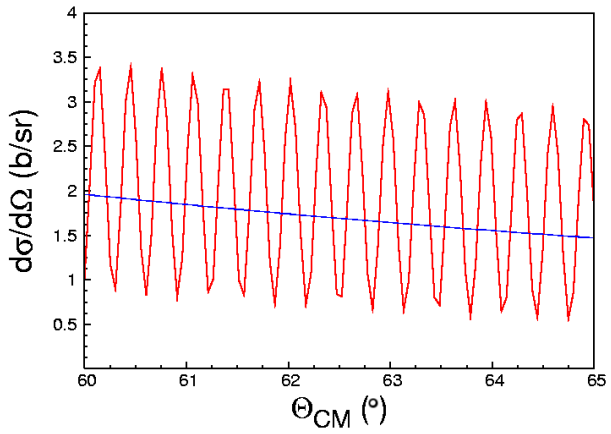

Figure 2.7: Calculated differential cross section for Mott elastic scattering (red) and Rutherford scattering (blue) for the reaction ^{238}U + ^{238}U at 7.35 MeV/A as a function of scattering angle in the center of mass frame [Gol06].

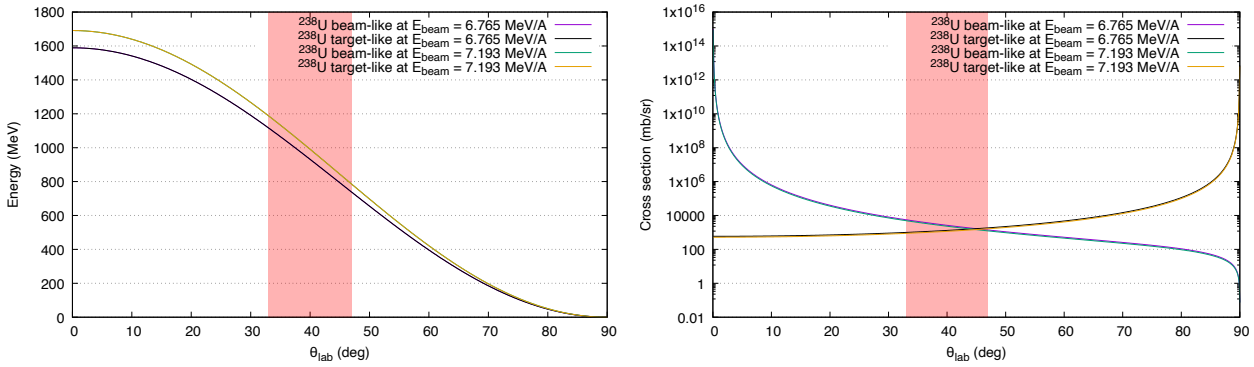

Figure 2.8: Calculated, using the LISE++ program [TB], kinematics (left) and cross sections (right) of the elastically scattered beam-like and target-like recoils from ^{238}U + ^{238}U reaction, following Rutherford's scattering, as a function of scattering angle for the energies of the beam utilized in the experiment of the present thesis. The red shaded area represents the region covered by the VAMOS++ spectrometer placed at 40°, see Section 3.4.1.

of closest approach between two nuclei is very close to the sum of their radii. The energies and the Rutherford cross sections calculated, using the LISE++ program [TB], for elastic scattering recoils for the ^{238}U + ^{238}U reaction are shown in Figure 2.8.

Quasi-elastic reaction refers to the reaction type associated with the rather low excitation with well-defined quantum states and a high degree of selectivity of the reaction products [Bas80]. In this reaction, the mass partition of interacting nuclei changes slightly with the projectile exchanging only few nucleons with the target. The projectile loses a moderate amount of kinetic energy and interacts at the surface of the target.

In the **deep-inelastic** reaction, a complex internal rearrangement takes place between the involved nuclei transferring a large number of nucleons [Bas80]. The projectile dissipates a large amount of energy which is converted into the intrinsic excitation of the reaction products, transferring a high angular momentum. The angular distribution of the reaction products exhibits a broad bell shape with a peak close to the grazing angle which indicates that the process is very fast. Large energy dissipations indicate that the two nuclei, before the emerging point, acquire large deformations. Based on observed fast interaction times and large energy dissipations, it was suggested by L. Corradi *et al.* [CPS09] that in the evolution of the reaction the excitation of surface modes plays an important role, with the low-lying modes being the main source for the formation of the large deformations.

In **fusion** reactions, the projectile and the target form a compound nucleus. This reaction occurs over a long time scale of the order of 10^{-18}-10^{-16} s during which a significant redistribution of the projectile energy takes place among the nucleons of the collision particles. This leads to a large number of degrees of freedom leaving the compound nucleus in a highly excited state. The de-excitation of the compound nucleus proceeds typically through the emission of particles (fusion-evaporation), γ-rays, conversion electrons (CE) and fission fragments.

2.3.1 Multinucleon transfer reactions

Multinucleon transfer (MNT) reactions in collisions of heavy-ions at Coulomb barrier energies are characterized by the exchange of several nucleons between the projectile and the target with population of relatively low excitation energy and of relatively high spins [CPS09, Mij22]. The amount of transferred nucleons define the evolution of the reaction type from quasi-elastic to the more complex deep-inelastic regime.

Due to the limitations of other reaction mechanisms like fusion-evaporation, MNT reactions can be an alternative path for the production of neutron-rich nuclei far from stability. One of the first investigations of the MNT reaction was performed using the ^{238}U + ^{238}U reaction by M. Schädel *et al.* at GSI in 1978 [SKA+78, KSG13]. From the yields identified using radiochemical

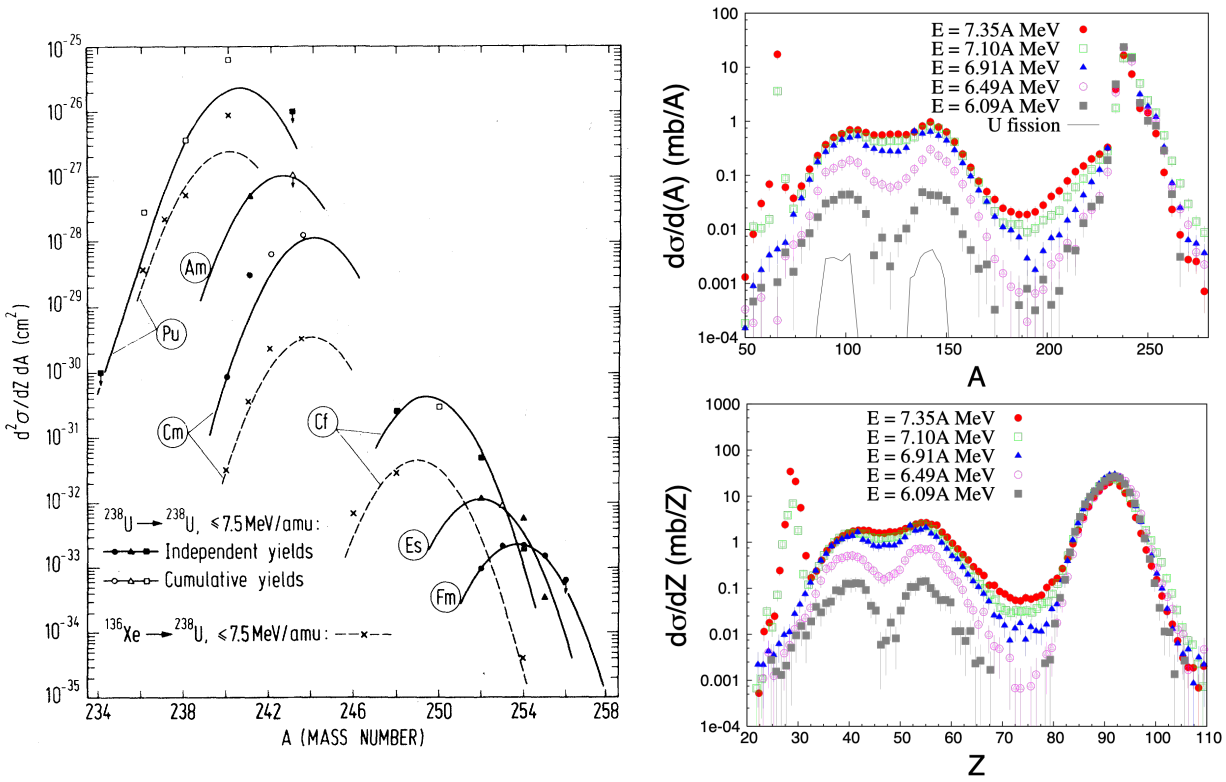

Figure 2.9: Left: The cross sections for the MNT products in the ^{238}U + ^{238}U and the ^{136}Xe + ^{238}U reactions measured via radiochemical separtion techniques at GSI. The enhancement of cross sections in the U+ U reaction is obvious [SKA+78]. Right: The mass (A) and atomic charge (Z) distributions of the ^{238}U + ^{238}U reaction products measured with VAMOS at GANIL in 2006 [GHM+10]. The used beam energies are indicated.

separation techniques, rather high production cross sections ranging from mbarn to nbarn were observed for the population of isotopes from Pu to Fm as shown in Figure 2.9 (left). In 2006, C. Golabek *et al.* carried out MNT studies using the ^{238}U + ^{238}U reaction with the VAMOS magnetic spectrometer [GHM+10]. It indicated that a massive nucleon transfer was observed at five different bombarding energies as shown in Figure 2.9 (right). However, these studies were hampered by the limited mass and atomic charge resolution ($\Delta A/A \simeq 1/40$, $\Delta Z/Z \simeq 1/17$) which restricted the identification of heavy nuclei.

Recently, V. I. Zagrebayev *et al.* using the Langevin-type equations based model [ZKG15] predicted that with the ^{238}U + ^{248}Cm reaction one can reach cross section values of around 1 μbarn to access neutron-rich actinide nuclei via MNT processes as shown in Figure 2.10. For the ^{238}U + ^{238}U reaction, the GRAZING [Win94, Win] and Langevin models predict cross sections of the order of a few μbarn for the production of +5 nucleon transfer channels of uranium-like nuclei [Kar16]. These values, being promising for both reaction mechanism and possible future

nuclear structure studies, awaits experimental verification.

Relying on the improved mass resolution performance of $\Delta A/A \simeq 1/263$ [RGS+17] achieved recently in the measurement of ^{208}Pb + ^{100}Mo at 6.25 MeV/A at VAMOS++, an experiment was performed at GANIL using a beam of ^{238}U at energies of 6.765 and 7.193 MeV/A impinging on a 615 μg/cm^2 ^{12}C-sandwiched metallic uranium target. VAMOS++ [RGS+17, RLN+11] was used to identify the atomic mass of the products while to determine the atomic number of the products, coincident x-rays were detected with the γ-ray spectrometer AGATA [CMd+17, KL19] together with the x-ray detector array named as ID-Fix. To slow down the reaction products and improve the time of flight (TOF) resolution in VAMOS++, which in turn would improve the resolution in mass, an aluminum degrader with a thickness of 20 μm was placed behind the target.

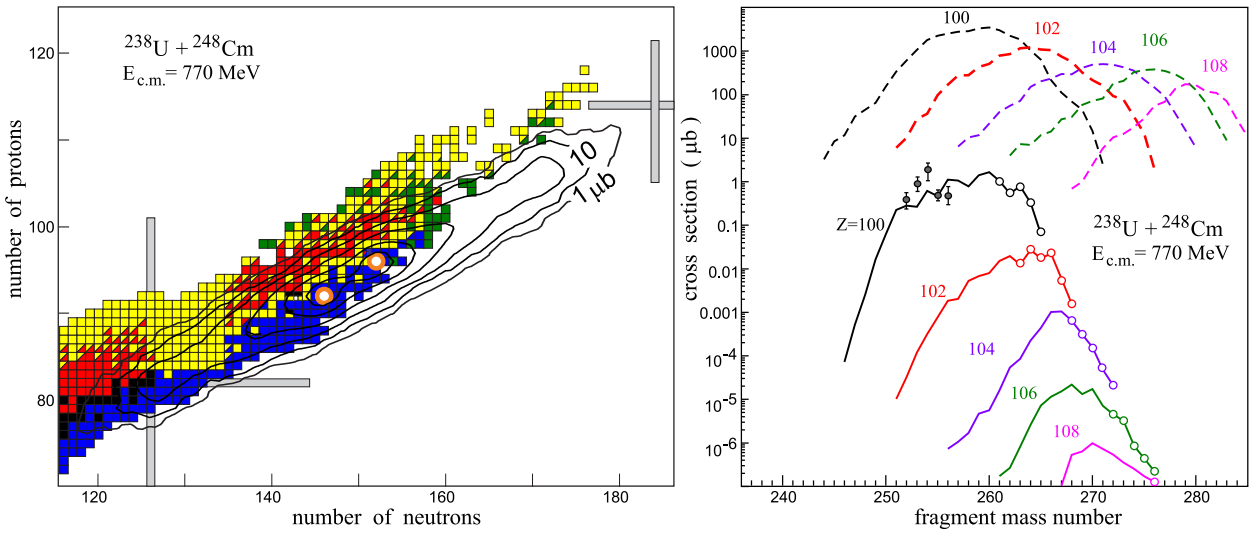

Figure 2.10: Calculated MNT cross sections, using the model based on the Langevin-type dynamical equations of motion, for the products of ^{238}U + ^{248}Cm reaction at $E_{c.m.}$ = 770 MeV [ZKG15]. Right: the primary distribution of the products. Left: primary and secondary or surviving distribution illustrated with the dashed and solid lines, respectively. Experimental data for Fm isotopes are represented by the closed circles and are taken from Ref. [SBG+82]. Open circles indicate new isotopes of transfermium elements that are predicted to be produced.

Chapter 3

Experimental Devices

Contents

3.1 Introduction

All of the experimental work of this thesis, from source and in-beam tests to the experiment, was carried out at GANIL. The experiment took place in May 2021. It was devoted to the investigation of the production cross sections of the exotic neutron-rich light actinide nuclei in the multinucleon transfer reaction of ^{238}U + ^{238}U. The measurement of the reaction products was performed employing the VAMOS++ magnetic spectrometer for the atomic mass A identification, the AGATA γ-ray spectrometer and the ID-Fix x-ray detection array for the atomic charge Z identification and (AGATA) the detection of coincident gamma transitions.

In this chapter, the setup used in this work is described. First, it starts by introducing the accelerator complex including the production and acceleration of the ^{238}U beam, and summarizes the beam time utilisation. Then, it presents the details of the targets and the target chamber which was designed and produced specially for this experiment. Finally, it gives a detailed description of VAMOS++, whose detection system was recently modified, AGATA and ID-Fix, together with their electronic and data acquisition scheme.

3.2 Accelerator complex

On September 4, 1975 two research organizations, CNRS/IN2P3 and CEA/DSM, with support from the Normandy[4] region as well as the European Union decided to build the Grand Accélérateur National d'Ions Lourds[5] (GANIL) in Caen, France. Today, it is one of the largest laboratories in the world focused on cutting edge research in nuclear physics, atomic physics, radiobiology, astrophysics, condensed matter physics and industrial applications via acceleration of heavy ion beams. The first beam, ^{40}Ar at 44 MeV/A, was extracted on November 19, 1982. The first experiment was carried out on January 18, 1983 [IN2]. The first publication reporting on the discovery of ^{23}N, ^{29}Ne and ^{30}Ne was published two years later [LQB+85]. It was made possible thanks to the performance of the doubly achromatic Ligne d'Ions Super Epluchés[6] (LISE) spectrometer which was designed for the production and identification of Radioactive Ion Beams (RIBs) produced by in-flight fragmentation of intermediate-energy heavy-ion beams [DDE+86]. Between 1983 and 1990, the facility was operating with a cascade of one Compact Cyclotron C01 used as an injector and for pre-acceleration of the beam up to 1 MeV/A, and two Separated-Sector Cyclotrons CSS1 and CSS2 to accelerate the beam up to 95 MeV/A. Subsequently, the second injector C02 was added. Since then, continuous progress has been made in developing various techniques to increase the performance of the facility in terms of beam currents, energies and the number of isotopes. In

[4] formerly Basse-Normandie; English: Lower Normandy
[5] National Large Heavy Ion Accelerator
[6] Super-Stripped Ion Line

September 2001, the new facility Systeme de Production d'Ions Radioactifs Accélérés en Ligne[7] (SPIRAL1) for producing RIBs was installed. It complements the available facilities and operates by the Isotope Separation On Line (ISOL) technique. In this technique, radioactive beams are produced in a thick target interacting with high-energy stable beams from the cyclotrons. Then, they are thermalized in the target, effuse up to its surface with thermal energy and diffuse out to an Electron Cyclotron Resonance (ECR) ion source to be ionized. Then, they are reaccelerated by the Cyclotron pour Ions de Moyenne Energie[8] (CIME) up to 25 MeV/A, selected by the ALPHA spectrometer based on their magnetic rigidity and sent to the experimental area [ABB+08]. In July 2005, the SPIRAL2 project was launched. This project is a major extension of the SPIRAL1. It aims to deliver, compared to SPIRAL1, much heavier ($60 < A < 140$) and much higher intensity (10^6 - 10^{11} pps) radioactive beams thanks to a new high-power superconducting linear accelerator (LINAC) [Pet11]. The LINAC serves three large halls for experiments using a high flux of fast neutrons at Neutrons For Science facility (NFS) [LAA+17], very high intensity beams of heavy-ions at the Super Separator Spectrometer facility (S^3) [SDD+15] and low-energy exotic nuclei at Désintégration, Excitation et Stockage d'Ions Radioactifs[9] facility (DESIR) [Bla10] produced at S^3 or SPIRAL1. The LINAC together with NFS are fully operational since December 19, 2021 [GANc] while the experimental program at S^3 is foreseen to start in 2024 and at DESIR early operation is envisaged in 2026. Presently, the LINAC is equipped with a single injector composed of two ion sources providing beams of protons, deuterons and ions with A/q = 3. The performance of this injector, however, is limited to medium masses with moderate intensity. To produce heavy-ion beams with substantially increased intensity the NEW GAnil INjector (NEWGAIN) project [ABC+21] aiming at developing a second injector with a source of ions with A/q = 7 was funded by EQUIPEX+ in January 2021 [UNI, IN2]. Its construction is planned to begin in January 2023. Figure 3.1 and 3.2 shows an overview of the GANIL/SPIRAL2 facility.

At the present time, the LINAC delivers high intensity beams up to ^{40}Ar as well as neutron beams. The cyclotron complex provides stable beams ranging from ^{12}C to ^{238}U with energies of 1 - 95 MeV/A, and with intensities up to 3000 pnA for ^{12}C ions and with intensities up to 8 pnA for ^{238}U ions, fragmentation beams spanning from light to medium mass nuclei up to 50 MeV/A and reaccelerated SPIRAL1 beams of 1.2 - 25 MeV/A for around 43 isotopes [GANb].

In the present experiment, the stable beam of ^{238}U was used. It was produced using the sputtering technique [BFD+98, LBC+04]. This technique makes use of the ECR ion source containing a plasma, confined by a magnetic field, and a metallic uranium sample. Positive ions of neon or oxygen from the plasma are accelerated toward the negatively biased sample. The atoms of the sample, as a result of the impact, are evaporated into the plasma, ionized and extracted from the source. Then, the ions are accelerated by the injector cyclotron C02 and CSS1. Finally, the beam

[7] System for On-line Production of Accelerated Radioactive Ions
[8] Cyclotron for Medium Energy Ions
[9] Decay, Excitation and Storage of Radioactive Ions

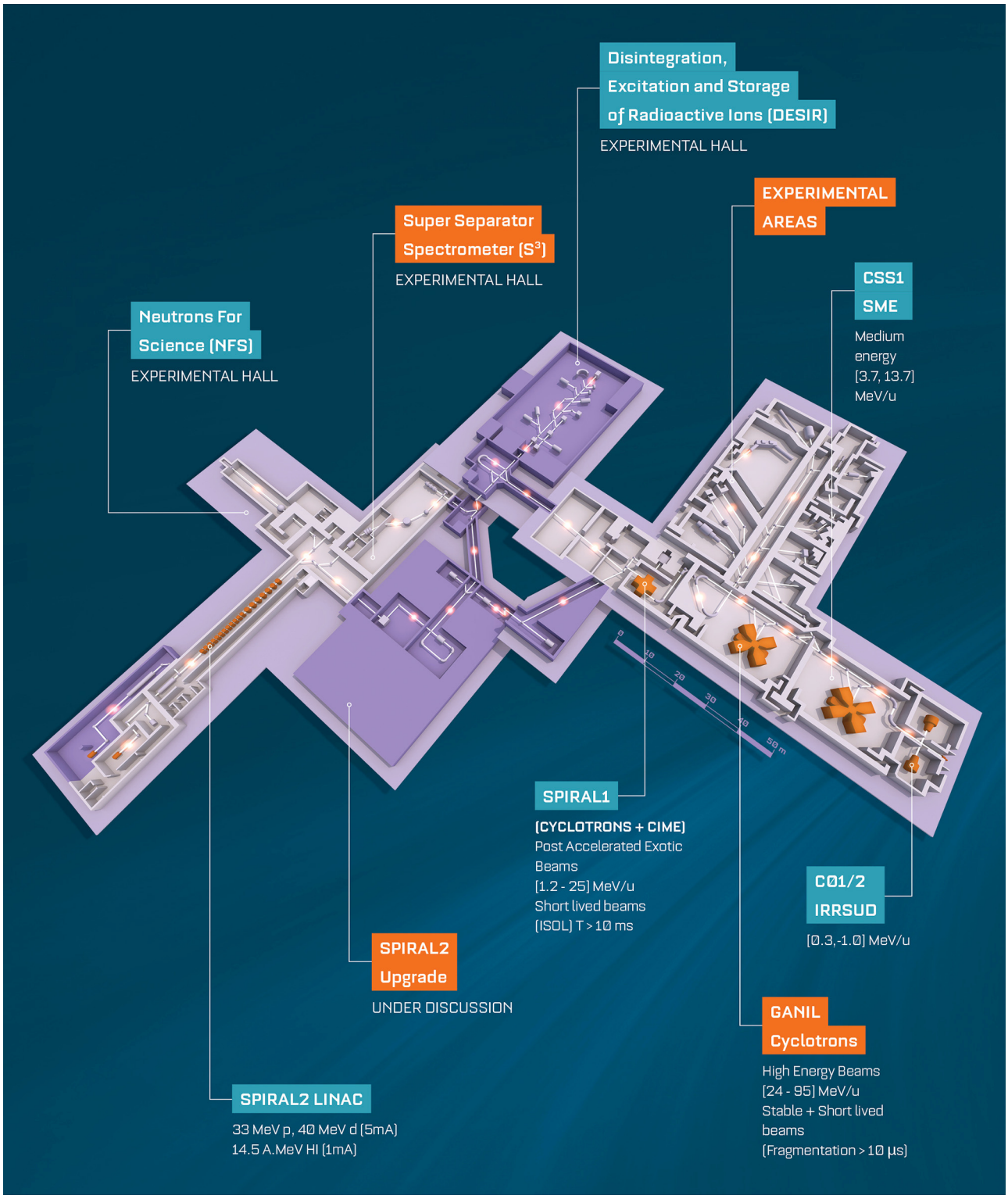

Figure 3.1: Layout of accelerator and instrumental installations at GANIL/SPIRAL2 [PPA+20].

is sent to the target chamber in the experimental hall G1, where the detection system was placed, passing through the ALPHA spectrometer which has dipole magnets allowing an efficient selection of the beam.

During the experiment there was a leak of the vacuum in the injector cyclotron C02. It resulted in a beam intensity lower than the requested 1 pnA by a factor of 15. In addition, a cryopump filling up the vacuum was regenerated several times to clean out the rest gas. However, this provided the beam still at low intensity, and later the vacuum became very unstable leading to an even lower beam intensity which made an intervention mandatory. After the intervention, during which the GANIL accelerator team worked on a reparation of the C02, the leak had vanished and the beam was back with a decent intensity of up to 1 pnA. Nevertheless, the beam intensity was reduced to about 0.4 pnA due to the count rate limitation of the detection system. As a consequence, it was possible to perform the experiment at two out of three (E_{beam} = 7.20, 6.77 and 6.35 MeV/A) planned beam energies and accumulate a beam dose of around 19% with respect to the requested amount. The energies, the intensities and the irradiation time of the uranium beam are summarized in Table 3.1.

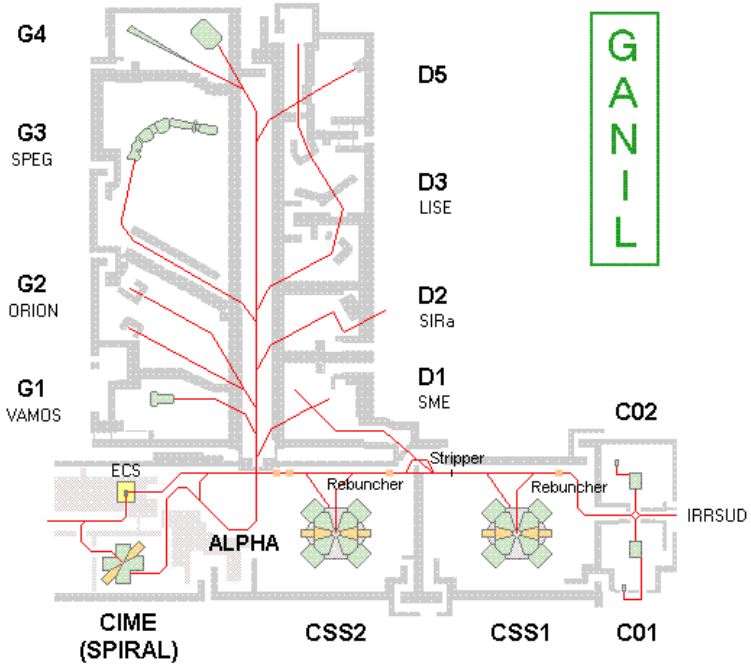

Figure 3.2: Schematic view of the GANIL facility [KCS16]. The lower part represents the accelerators composed of 5 cyclotrons: the injector cyclotrons C01 and C02, the Separated-Sector Cyclotrons CSS1 and CSS2, and the post-accelerator cyclotron of RIBs CIME. The upper part illustrates the experimental area of 8 halls with various detection systems. The experiment took place in G1, see Section 3.4, while the source and the in-beam tests in G2, see Section 4.3 and 4.2, respectively.

3.3 Targets and target chamber

The targets were mounted on a target holder inside the target chamber. The holder and the chamber were designed by Patrice Gangnant specially for our experiment and were produced in-house at GANIL. The holder enables to mount 5 targets. The chamber was designed in such a way that it allows to insert 3 LEPS detectors, see Section 3.4.2, closer to the target position, increasing the geometrical efficiency, through a *doigt de gant*[10]. The *doigt de gant* had an aluminum front window, facing the target, with a thickness of 1.5 mm which was established to be optimum in our previous in-beam test, see Section 4.2. A schematic layout and pictures of the holder and the chamber are shown in Figure 3.3.

In the present experiment, targets of metallic ^{238}U were used. They, together with their frames, were manufactured in sandwich composition between two carbon layers by our collaborators at the GSI Target Laboratory in Germany [KAH+08, LCH+20]. Eightteen targets with an effective surface of 14 x 10 mm^2 on frames with a size of 20 x 13 mm^2 were delivered to GANIL. Figure 3.4 shows the photograph of the metallic ^{238}U targets prepared for transportation. Three of them were mounted on the target holder. In addition, ^{197}Au targets for calibration purposes and a 20 μm aluminum degrader foil to slow down the reaction products were used. Details on the mounted target materials are summarized in Table 3.2. After the interaction of the beam with the target, the products of the reaction were measured by the detection system described in the next section.

[10]English: thimble

Figure 3.3: Left: Schematic illustration of the target holder, and the top and bottom hemispheres of the target chamber with 3 LEPS detectors, described in Section 3.4.2, inserted through the *doigt de gant* (see text for details). The part of the target chamber to which the beam line and the VAMOS++ spectrometer connect is not shown. Middle and right: Photographs of the top hemisphere and the targets mounted on the target holder in and opposite of the beam direction, respectively. Numbering of the targets is from bottom to top. The Al degrader is placed behind the targets #2, #3 and #4.

Table 3.1: Summary of the beam time usage, including the in-beam calibrations and the actual measurement. The beam time in shifts of UT (unit of time) allocated by the GANIL PAC, the requested intensities and yields are compared to the obtained values. One UT is equal to 8 hours. The yield is equivalent to $\frac{\text{Beam dose}_{\text{obtained}}}{\text{Beam dose}_{\text{allocated}}}$.

Beam	Energy (MeV/A)	Allocated			Obtained			Yield
		UT	Intensity (pps)	Beam dose (particles)	UT	Intensity (pps)	Beam dose (particles)	
$^{238}U^{33+}$	7.193	21[11]	6.24×10^{9}	1.89×10^{15}	9.67	7.75×10^{8}	2.16×10^{14}	11 %
$^{238}U^{32+}$	6.765			1.89×10^{15}	8.13[12]	2.18×10^{9}	5.12×10^{14}	27 %

Table 3.2: Position and characteristics of the targets mounted in the chamber. Positions correspond to the numbering of the targets placed on the holder shown in Figure 3.3. ^{197}Au targets are for calibration purposes. A 20 μm aluminum degrader foil was used to reduce the velocity of the reaction products. Targets #1, #3 and #5 were irradiated.

Position	Material	Thickness (μg/cm^2)	Degrader
5	$^{12}C/^{238}U/^{12}C$	50/620/5	-
4	$^{12}C/^{238}U/^{12}C$	50/615/5	20 μm Al
3	$^{12}C/^{238}U/^{12}C$	50/615/5	20 μm Al
2	^{197}Au	90	20 μm Al
1	^{197}Au	90	-

[11] Total of 21 UTs of measurement at two beam energies, with 10.5 UTs each, excluding the beam and the setup tuning 6 UTs

[12] including 0.5 UT of buffer

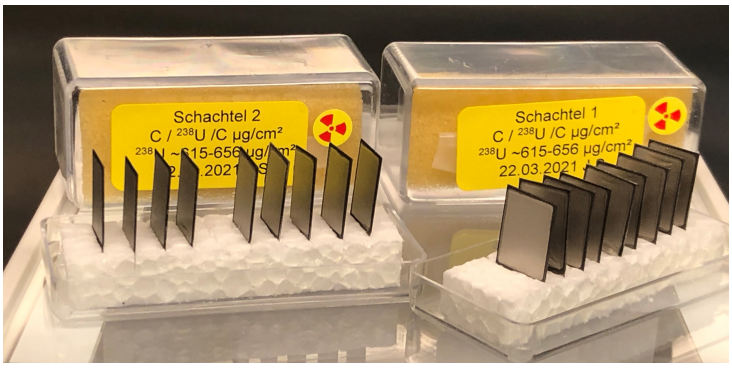

Figure 3.4: The metallic ^{238}U targets sitting in two plastic boxes with dimensions of 70×35×30 mm^3 for transportation. Photograph taken by Bettina Lommel, GSI.

3.4 Detection setup

The present experiment took place in the experimental hall G1 at GANIL, see Figure 3.2. To measure the reaction products it exploited the detection setup composed of the VAMOS++ magnetic spectrometer in combination with the AGATA γ-ray spectrometer and the ID-Fix x-ray detection array. As mentioned previously, VAMOS++ was used to identify the atomic mass A while AGATA and ID-Fix served to determine the atomic charge Z of the products and (AGATA) to measure coincident gamma transitions. Figure 3.5 shows a schematic illustration and a photo of the detection setup. Detailed description of each of them will be presented in the following sections.

3.4.1 The VAMOS++ magnetic spectrometer

The VAriable MOde Spectrometer (VAMOS) is a large acceptance magnetic spectrometer designed for the identification of the reaction products employing a trajectory reconstruction [Sav99, Sav03, PRN+08, PCJ+08]. Its design was started in 1996 in view of the construction of the SPIRAL installation which needed a highly efficient detection system to study reactions induced by the low intensity RIB. It became operational and was under commissioning over the period between 2001 and 2003. In September 2003, the first experiment was carried out using a pure and intense radioactive beam of ^{24}Ne produced by the recently at that time commissioned SPIRAL1 installation [IN2]. Thanks to the combination of VAMOS, a charged particle array TIARA [CTL+03, LCL+10] and an array of segmented clover germanium detectors EXOGAM [SAdF+00] it was possible to study the nuclear structure of ^{25}Ne [CLL+05]. Between 2001 and 2011, the spectrometer was operating with the focal plane detection system, composed of two Drift Chambers (DCs), a Secondary Electron Detector (SED), an Ionization Chamber (IC), a plastic scintillator or an array of silicon detectors, covering an active area of 400×110 mm^2. In 2011, the spectrometer was upgraded to the VAMOS++ version. New detectors covering a larger area of 1000×150 mm^2 were implemented for the focal plane based on calculations [PRN+08] and experimental investigations [RLN+11] showing that doubling the size of the detectors improves significantly the transmission of the particles through the spectrometer and increases the momentum acceptance from $\sim$11% to $\sim$30%. Additionally, Multi-Wire Parallel Plate Avalanche Counters (MWPPACs) were placed at the entrance and at the focal plane of the spectrometer. They provided a time of flight measurement with better time resolution which allowed to achieve the improved mass resolution of $\sim$1/220 compared to the previous one of $\sim$1/170. In 2015, new Dual Position Sensitive Multi-Wire Proportional Counters (DPS-MWPCs) were installed at the entrance of VAMOS++ [VLR+16]. They are used for both timing and tracking measurements. They provide a better precision of the scattering angle at the target, which results in an improved mass resolution of $\sim$1/263 (FWHM) [RGS+17], than the one obtained previously from the trajectory reconstruction of the ions measured at the focal plane. In May 2021, the DCs and the MWPPAC at the focal plane were replaced by two MWPPACs allowing

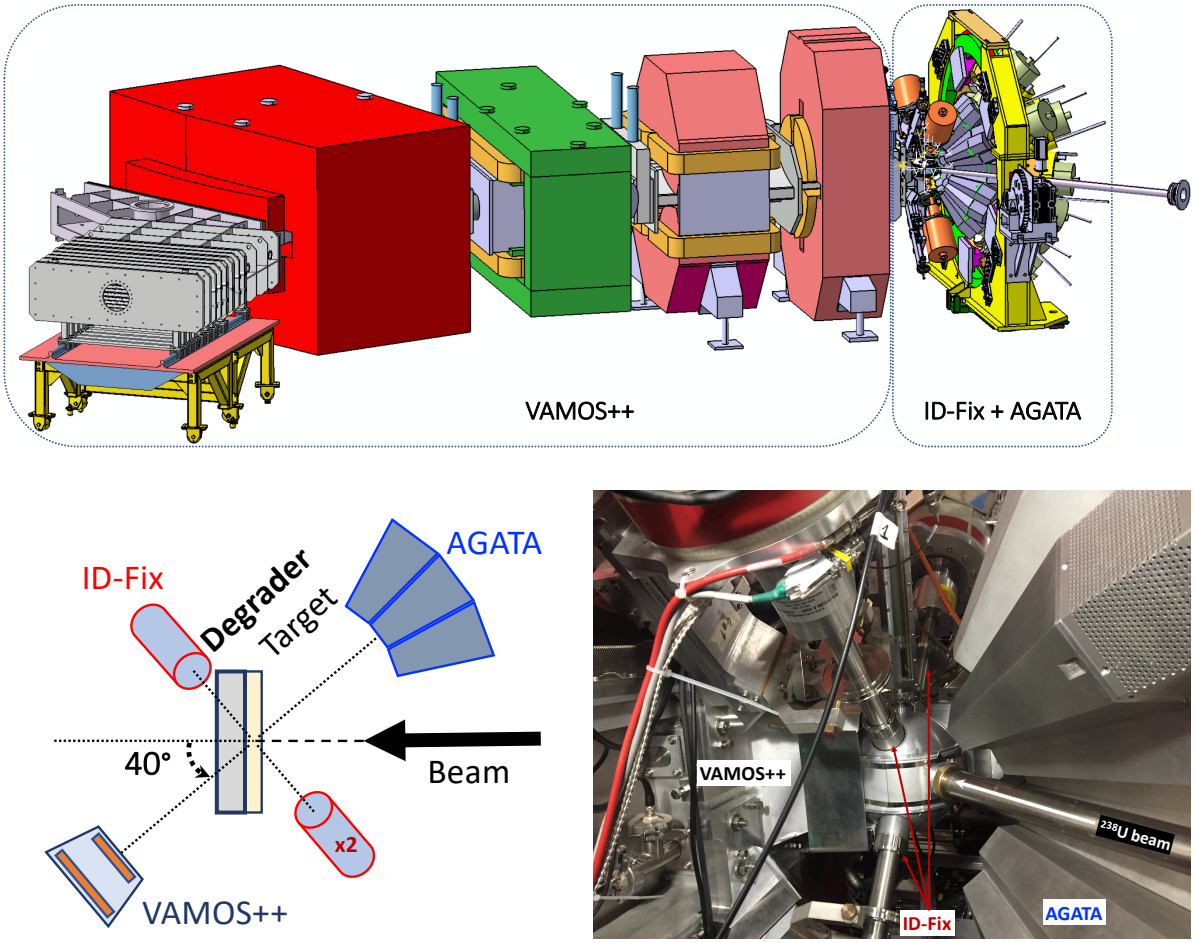

Figure 3.5: Top: Schematic layout of the detection setup consisting of the VAMOS++ spectrometer, the AGATA spectrometer and the x-ray detection array ID-Fix. Bottom: Schematic diagram (left) and photograph (right) of the setup taken in the experimental hall G1 at GANIL. In the photograph, the beam line and the AGATA spectrometer are on the right. The target chamber is in the center. The entrance of the VAMOS++ spectrometer is on the left. ID-Fix composed of 3 LEPS detectors are inserted from the top and the bottom of the target chamber.

to have both tracking and timing measurements which were obtained by the predecessors separately. The use of the new MWPPACs allows to have improved counting rate capabilities, lower energy losses [VLR+16] and possibly a better mass resolution. One of them was tested in-beam previously, the other one was new. In the actual experiment they were used for the first time.

Today, VAMOS++ is the spectrometer having one of the largest acceptances in the world. It is used in various experiments dedicated to heavy ion reactions, such as elastic and inelastic scattering, deep inelastic, transfer, fission and fusion evaporation reactions at energies around the Coulomb barrier, using beams from both the cyclotrons and SPIRAL1. It provides a complete identification of the reaction products in both the atomic charge Z and the mass A. The identification is performed event-by-event by combining the information on reconstructed parameters, such as the magnetic rigidity (Bρ) and the flight path length (L), and on measured quantities, such as the time of flight (TOF), the energy loss (ΔE) and the total energy (E), see Section 5.2. This information is provided by a versatile detection system consisting of the DPS-MWPCs at the entrance, and the two MWPPACs and the IC at the focal plane. The detection system of the spectrometer is shown in Figure 3.6. The main characteristics and the measured quantities of each of the detectors are listed in Table 3.3. The spectrometer has an ion optical system composed of two quadrupole and one dipole magnets configured to operate in different optical modes. It also has a Wien filter which was not used in the present experiment and is generally used when the spectrometer operates as a recoil separator for low energy fusion evaporation residues at 0° [PRN+08]. The spectrometer is mounted on a platform that can be rotated around the target from 0° to 60° relative to the beam direction. In this way, it makes two-body reactions, such as multi-nucleon transfer (MNT), possible to be studied. In the present experiment, the spectrometer was placed at the grazing angle of 40° of the reaction of interest, see Figure 3.6. Its main operational features are given in Table 3.4.

With the new configuration of the modified detection system[13] and with the kinematics of the ^{238}U + ^{238}U reaction products followed by the aluminum degrader[14] the expected mass resolution was evaluated to be $\sim$1/301 (FWHM), making it good enough to resolve the masses of uranium-like nuclei of interest. However, the performance of VAMOS++ in terms of the atomic charge resolution is limited to $\sim$1/66 (FWHM) [RLN+11], provided by the IC detector (see Section 3.4.1.4), which is not sufficient to measure the atomic charges of interest. Therefore, an alternative method was used. This method involves a characteristic x-ray spectroscopy allowing to establish the atomic charge of the detected ions. The x-ray spectroscopy was performed by the ID-Fix and AGATA spectrometer coupled to VAMOS++. In this way, the velocity and angle information provided by

[13]The increase of the distance between the new focal plane MWPPACs allows to improve the angular resolution and, hence, the magnetic rigidity resolution of VAMOS++

[14]The kinematics and the used degrader in the present experiment allow to obtain lower velocity of the products which leads to the improved TOF resolution with respect to the one in the measurement of ^{208}Pb + ^{100}Mo at 6.25 MeV/A where the mass resolution of $\sim$1/263 (FWHM) were achieved [RGS+17]

Table 3.3: Characteristics and measured quantities of the detectors of the VAMOS++ together with their distances relative to the target position. The distances are provided by the mechanics group of GANIL and are defined along the central trajectory of the spectrometer.

Detector/Window	Distance (mm)	Active area/volume	Measurand	
Mylar (0.9 μm)	127			
MWPC$_1$	140.5	40×61 mm^2	X_1^{tp}, Y_1^{tp}, t_1^{tp}	
MWPC$_2$	249.9	65×93 mm^2	X_2^{tp}, Y_2^{tp}, t_2^{tp}	
Mylar (0.9 μm)	263.4			
Mylar (0.9 μm)	7609.9			
MWPPAC$_1$	7681.4	1000×150 mm^2	X_1^{fp}, Y_1^{fp}, t_1^{fp}	
Mylar (0.9 μm)	7759.4			
Mylar (0.9 μm)	8159.9			
MWPPAC$_2$	8204.9	1000×150 mm^2	X_2^{fp}, Y_2^{fp}, t_2^{fp}	
Mylar (1.5 μm)	8327.8			
IC$_1$	8329.9		ΔE_1	} E
IC$_2$	8339.5		ΔE_2	
IC$_3$	8389.9		ΔE_3	
IC$_4$	8449.9	1000×150×578.9 mm^3	ΔE_4	
IC$_5$	8569.8		ΔE_5	
IC$_6$	8689.6		ΔE_6	
IC$_7$	8808.8		ΔE_7	

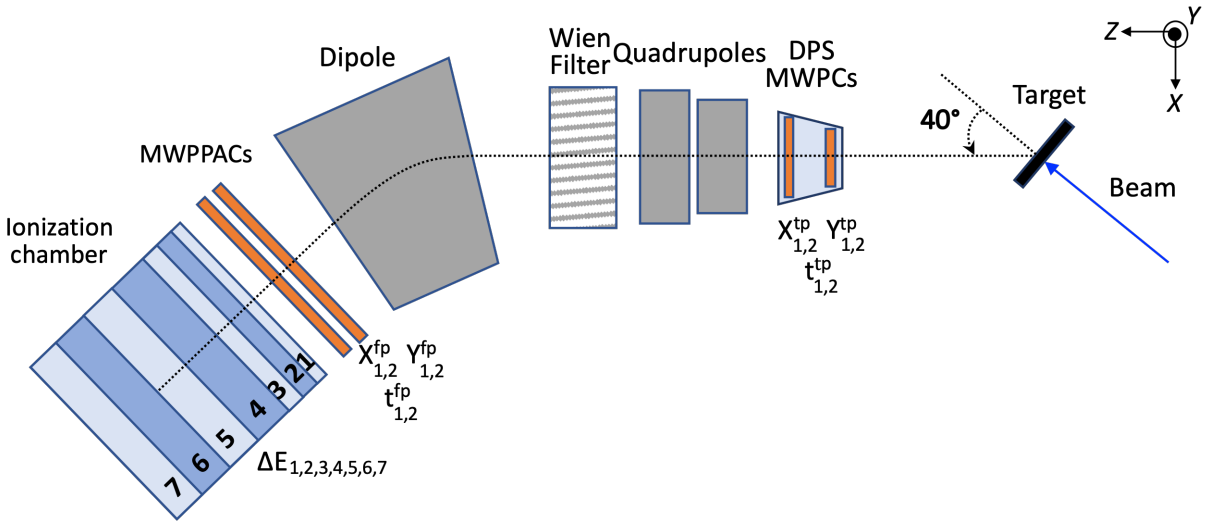

Figure 3.6: Schematic diagram of the optical elements and the detection system of the VAMOS++. The Wien filter was not used in the experiment of this work.

Table 3.4: Operational features of the VAMOS++ magnetic spectrometer [PRN+08, VLR+16]. The spectrometer was placed close to the grazing angle of 40° of the reaction of interest. The magnetic rigidity Bρ for the central trajectory was varied between 0.85 and 1.15 Tm depending on the energy of the beam and the presence of the degrader. The atomic mass resolution given here was obtained previously with the DCs.

Atomic charge resolution (ΔZ/Z)	$\sim$1/66 (FWHM) [RLN+11]
Atomic mass resolution (ΔA/A)	$\sim$1/263 (FWHM) [RGS+17]
Horizontal acceptance ($\Delta\theta$)	$\pm$7°
Vertical acceptance ($\Delta\phi$)	$\pm$11°
Maximum rigidity (Bρ)	1.6 Tm
Flight path length (L)	$\sim$7.6 m
Angular rotation	0 - 60°

VAMOS++ allows to apply the Doppler correction for coincident x-rays energies.

The ion optical and the detection system of the spectrometer including its electronic scheme will be described in the following sections.

3.4.1.1 Entrance DPS-MWPCs

Since the last decade continuous upgrades have been made in order to improve the performance of the VAMOS++ spectrometer. One of the recent upgrades is a detector assembly consisting in a pair of Dual Position Sensitive Multi-Wire Proportional Counters (DPS-MWPCs) placed at the entrance of the spectrometer. It provides the measurement of the scattering angle and interaction point on the target. It also provides a timing information allowing to obtain the velocity of the reaction products. The resulting resolution in position, angle and time allows to obtain an improved mass resolution and leads to a superior Doppler correction.

The products entering the spectrometer are measured by the detector assembly of two DPS-MWPCs [VLR+16]. The assembly is placed at a nominal distance of 174 mm from the target. It covers the full acceptance of the spectrometer with the front and back MWPCs having a sensitive area of 40×61 mm^2 and 65×93 mm^2, respectively. Each of the detectors is composed of three electrodes: two orthogonally oriented anode wire planes for $X^{tp}_{1,2}$ and $Y^{tp}_{1,2}$ positions, and a central cathode wire plane for $t^{tp}_{1,2}$ timing information. The cathodes of the two detectors are separated by 105 mm. The cathode and anode planes of each of the detectors are separated by 2.4 mm, see Figure 3.7 (a). All of the electrodes are composed of 20 μm gold plated tungsten wires. The wires of the cathodes and the anodes are separated by 0.5 mm and 1 mm, respectively. The difference in distance between the cathode and the anode wires were chosen to obtain the required avalanche

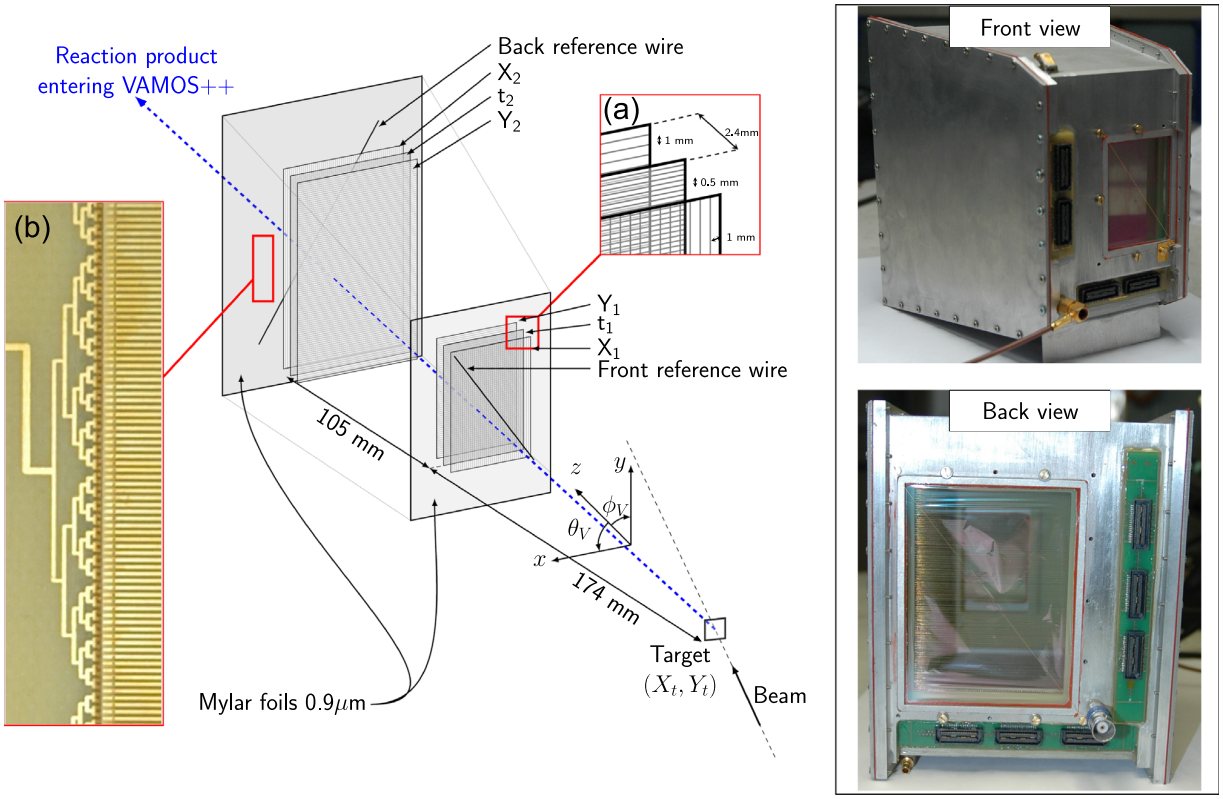

Figure 3.7: Left: Schematic layout of the DPS-MWPC detector assembly consisting of a pair of position sensitive MWPCs. Inset (a): Closer view at the three wire planes illustrating the wire plane orientation and spacings. Inset (b): Picture of the time plane signal route having equal path length which makes the signal path length independent of the Y position, to avoid a dispersion in the measurement of the time signal due to the propagation of the signal along the different wires. The remaining dispersion due to the varying X position is corrected via software on an event-by-event basis. Right: Front and back views of the detector assembly [VLR+16].

amplification gain. To align the detector assembly and obtain the position resolution two reference wires made of gold plated tungsten with a diameter of 100 μm are placed diagonally 1 cm upstream and downstream of the front and back MWPCs, respectively. The two detectors are placed in a common gas volume isolated at the entrance and the exit with 0.9 μm thick Mylar windows. They typically operate using isobutane gas (C_4H_{10}) at pressures of 2 - 6 mbar. The cathodes are typically polarized at negative potentials ranging from -415 V to -475 V and the anodes are grounded. In the present experiment, the pressure of the gas was initially set to 3 mbar, was later increased to 6 mbar and then set back to 3 mbar (due to the decrease of the beam energy from 7.193 to 6.765 MeV/A), the voltages of the cathodes were kept between -410 and -418 V. Figure 3.7 shows a schematic view and pictures of the detector assembly.

Table 3.5: Nominal performances of the DPS-MWPC detector.

Measurand	Resolution (σ)
X_1^{tp}, Y_1^{tp}	73(9) μm
X_2^{tp}, Y_2^{tp}	84(11) μm
t_1^{tp}	130(5) ps

A particle passing through the DPS-MWPCs detector assembly ionizes the gas molecules leaving a trail of electron-ion pairs along its path. Due to the applied electric field the produced electrons and ions are accelerated towards the anodes and the cathode of each of the MWPCs, respectively. The accelerated electrons gain significant kinetic energy and generate an avalanche of new electron-ion pairs. The charges of the avalanche of electrons, indicating the position at which the original electron-ion pair was formed thus the position of the particle (see an example of the charge distribution in Figure 5.5), are collected by the anode wires while the corresponding ions are detected by the cathode wires. The cathodes of both detectors provide one timing signal each. The anodes of the front MWPC has 39 wires in horizontal and 60 wires in vertical position while the one of the back has 64 wires in horizontal and 92 wires in vertical position. Each anode wire acts as independent detector and is read out individually. The treatment of the charges collected on the anode wires to obtain positions and the timing signals from the cathodes will be described in Section 3.4.4. The nominal performance of the detector in terms of the resolution in position, angle and time of flight is given in Table 3.5. The detection efficiency of ~96% was measured for heavy ions with $28 \leq Z \leq 65$ and energies ranging between 2 and 8 MeV/A due to the stopping by the 20 μm wires of the cathode and anode planes [VLR+16].

3.4.1.2 Ion optical system

Examining several spectrometer configurations for the construction of VAMOS it was chosen to combine the characteristics of a variety of spectrometers in the domain and to have the possibility to work in different modes of operation [Sav03]. These modes can be optimized depending on the requirements of the diversity of experiments. In the present experiment, the spectrometer was employed in a momentum dispersive mode. In this mode, the ion optical system of the spectrometer is configured to focus and bend the reaction products to the different positions in the focal plane according to their magnetic rigidities. The latter is required for particle identification and is obtained based on a reconstruction of the particle trajectories in the optical system of the spectrometer.

After the DPS-MWPCs, particles are guided through the ion optical system which consist of three magnets: two quadrupoles followed by one dipole, see Figure 3.6. The first and the second quadrupoles focus the particles in y-direction, perpendicular to the plane of dispersion, and in x-

direction, the dispersion plane, respectively. The first one has a diameter of 30 cm and a magnetic length of 60 cm while the second one has a magnetic length of 90 cm and an elliptical aperture with its x-axis of 100 cm, to compensate the dispersion in x introduced by the first quadrupole. The dipole deflects the particles according to their magnetic rigidities. It has a variable deflection angle of 0 - 60° with a nominal deflection radius of 1.5 m and the nominal maximum magnetic rigidity of 1.6 Tm. In the present experiment, the magnetic rigidity was varied between 0.85 and 1.15 Tm depending on the energy of the beam and the presence of the degrader.

3.4.1.3 Focal Plane MWPPACs

A step further towards improving the performance of VAMOS++ was made by modifying its focal plane detection system. The latest upgrade is a pair of Multi-Wire Parallel Plate Avalanche Counters (MWPPACs). It is a larger version of the DPS-MWPCs at the entrance of the spectrometer. It replaced the DCs and the existing MWPPAC and provides both the timing and position information which were measured by its predecessors separately. It aims to improve the resolution in time and position, thus the mass resolution. It also aims to provide lower energy losses of reaction products and an improved counting rate capability compared to the DCs.

The particles exiting the dipole are detected by the two MWPPACs. They have an active area of 1000×150 mm^2 each. The first and the second one are placed, along the central trajectory of the spectrometer, at a distance of around 7.6 and 8.2 m from the target, respectively. They are separated from each other by a distance of 523.5 mm in vacuum. The distance was chosen based on the estimations of the expected resulting mass resolution. Similar to the DPS-MWPCs, each of the detectors has a three electrode structure made of 20 μm gold plated tungsten wires: one cathode and two orthogonally placed anode wire planes used to measure the time ($t^{fp}_{1,2}$) and positions ($X^{fp}_{1,2}$ and $Y^{fp}_{1,2}$), respectively. The former and the latter have wires every 500 μm and 1 mm, respectively. The planes are separated by 2.4 mm from each other. One 100 μm gold plated tungsten wire is placed upstream of the first detector for calibration purposes and for obtaining the position resolution. In the present experiment, the focal plane MWPPAC detectors, similar to the entrance DPS-MWPC detectors, operated in a gas volume filled with isobutane (C_4H_{10}) at a pressure of 3 mbar initially, then increased to 6 mbar and then set back to 3 mbar (due to the decrease of the beam energy from 7.193 to 6.765 MeV/A). The gas volume was isolated with 0.9 μm thick Mylar windows. The cathodes were polarized at negative potentials between -420 and -424 V while the anodes were at ground potential. Figure 3.8 (left) shows a schematic view of the detector.

The working principle of the MWPPACs is similar to the one of the DPS-MWPCs. It is based on a larger amount of position wires, 992 in X and 160 in Y, and 20 independent time signals in each of the MWPPACs. The time signals of the MWPPACs and DPS-MWPCs are used for the time of flight measurements. Processing of the position and timing signals will be described in

Section 3.4.4.

3.4.1.4 Ionization Chamber

The last detector at the focal plane of the spectrometer is a segmented Ionization Chamber (IC) [RLN+11]. It provides ΔE-E measurement to identify the atomic charge Z of the reaction products. It also provides, combining the velocity and magnetic rigidity information measured with the spectrometer, the mass A of the reaction products, see Section 5.2.2. In the present experiment, the IC was not used for obtaining Z due to the limited resolution of ∼1/66 (FWHM) [RLN+11] for distinguishing the atomic charges of uranium-like nuclei of interest and was needed for the A identification.

At the end of the trajectory through the spectrometer, the particles are measured and stopped in the IC. It is placed at a distance of around 8.3 m from the target. It has an active volume of 1000(x)×150(y)×578.9(z) mm^3. It consists of a common cathode and an anode separated by a Frisch grid. The anode is divided in z-direction into 7 segments with dimensions given in Table 3.6. The grid is placed at a distance of 20 mm from the anode, made of gold coated tungsten wires with a diameter of 50 μm with 1 mm spacing. In the present experiment, the volume of the detector was filled with a CF_4 gas at a pressure of 50 mbar. To separate the MWPPACs and the IC which have different gas pressures a mylar window with a thickness of 1.5 μm was placed. A

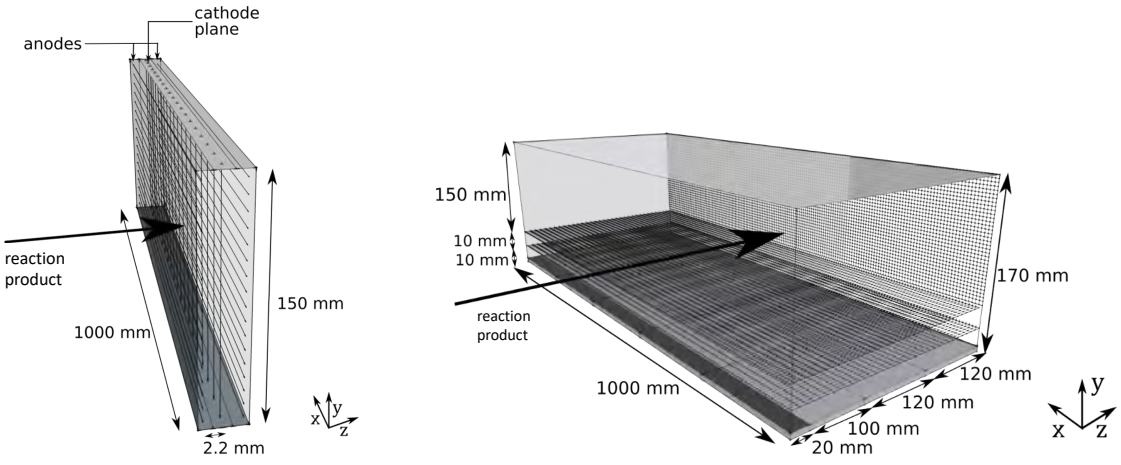

Figure 3.8: Left: schematic diagram of the MWPPAC detector. Only few wires are shown for a clear view of the detector. Right: schematic diagram of the IC detector. The characteristics of an acceleration grid placed at 10 mm from the anode on the lower part of the chamber is similar to the one of the Frisch grid described in the text. The dimensions of the anodes in z-direction are given in Table 3.6 and are different from the ones shown in the figure. The figures are taken from Ref. [Ram16].

Table 3.6: The dimensions of the anode pads segmenting the IC detector in depth.

Segment	Dimension (mm)	Measurand	
IC_1	9.6	ΔE_1	
IC_2	50.4	ΔE_2	
IC_3	60	ΔE_3	
IC_4	119.9	ΔE_4	E
IC_5	119.8	ΔE_5	
IC_6	119.2	ΔE_6	
IC_7	100	ΔE_7	

schematic representation of the detector is shown in Figure 3.8 (right).

A particle travelling through the IC ionizes the gas medium and loses part of its kinetic energy. As a result of the ionization, electron and ion pairs are formed. The ion is collected by the cathode and the electron drifts towards the segmented anode passing through the Frisch grid. The electron drifting across the grid-anode region provides a signal with an amplitude proportional to the energy loss ($\Delta E_{1,2,3,4,5,6,7}$) of the particle. Summing the energy lost in all the segments of the IC one can obtain the total energy (E) of the particle. The signal processing of the detector will be given in Section 3.4.4.

3.4.2 The ID-Fix x-ray detection array

ID-Fix is an x-ray detection array consisting of 3 Low Energy Photon Spectrometers (LEPSs). Thanks to the LEPSs, it was possible to measure coincident x-ray yields in fusion followed by fission reactions of ^{238}U + ^{64}Ni at 6.6 MeV/A and in quasifission reactions of ^{48}Ti + ^{238}U at 5.75 MeV/A. In the ^{238}U + ^{64}Ni reaction, the detected K x-rays were attributed to the compound nuclei with Z = 120 [FJM+12]. In the ^{48}Ti + ^{238}U reaction, the atomic charges of the quasifission fragments were determined from the associated $K_{\alpha 1}$ and $K_{\alpha 2}$ x-ray energies [MHS+17]. In the present experiment, the ID-Fix array was used to identify the atomic charge Z of the reaction products via the measurement of their emitted characteristic x-rays. A schematic layout of the array is shown in Figure 3.9 (left).

X-rays and low-energy γ-rays emitted from the reaction products were detected by the LEPS detectors. They were mounted at a distance of ~4 cm from the target, looking through the *doigt de gant* (see Section 3.3), made of aluminum with a thickness of 1.5 mm. The thickness of aluminum for the *doigt de gant* was needed to suppress low-energy photons from atomic de-excitations and was chosen based on the results of the in-beam test reported in Section 4.2. During the experiment, an absorber of 0.5 mm titanium was placed additionally since the count

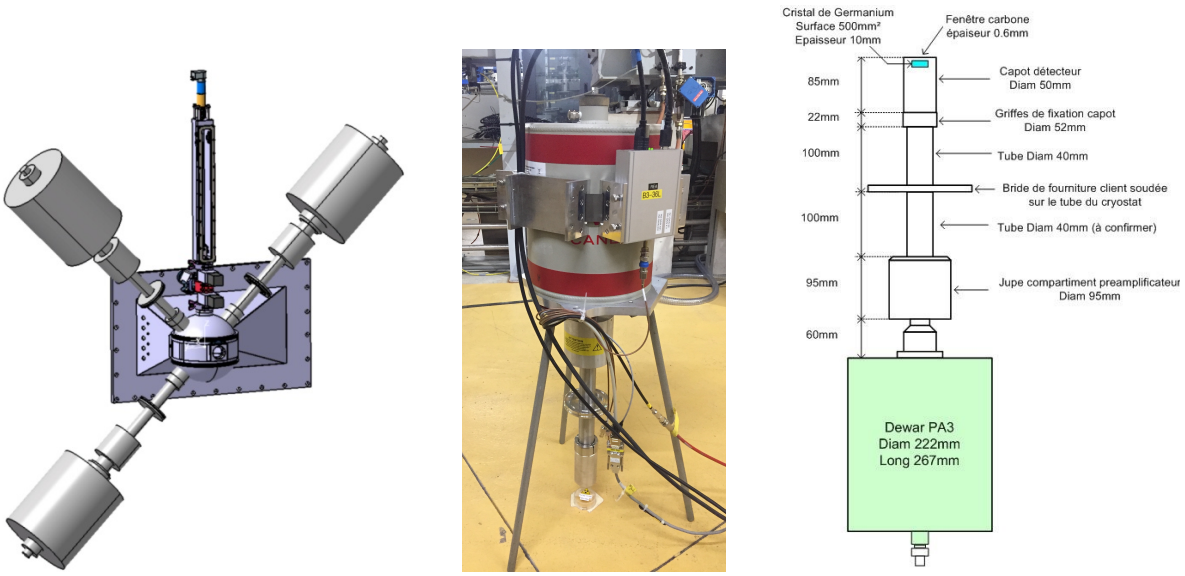

Figure 3.9: Left: schematic illustration of the ID-Fix array, the target chamber and the entrance of the VAMOS++ spectrometer. The three LEPS detectors are mounted close to the target through the *doigt de gants*. Positions of the detectors are given in Table 3.7. Middle: photograph of one of the LEPSs taken during the source test, see Section 4.3 for details of the test. Right: schematic layout of the LEPS detector.

Table 3.7: Geometrical characteristics of the HPGe crystals of the LEPS detectors. Positions of the LEPS detectors including the distance (d) from the target, provided by the mechanics group of GANIL, and the angles (θ, ϕ) with respect to the central trajectory of the VAMOS++ spectrometer, see Figure 5.29.

Detector	LEPS ID	HPGe crystal		LEPS position		
		Thickness (mm)	Area (cm^2)	d (mm)	θ (deg)	ϕ (deg)
1	81359	10.2	5.6	41.4	-87.31°	43.89°
2	81360	10.1	5.8	39.5	-86.81°	-46.98°
3	81361	10.2	5.8	42.2	86.73°	44.64°

rate at nominal beam energies and at the experimental conditions with the actual (new) VAMOS target chamber was higher than the expected one. The detectors covered altogether a solid angle of ∼6 %. Each of the LEPSs has a planar circular n-type high purity germanium (HPGe) crystal with a diameter of around 2.67 cm and a thickness of ∼1 cm, making it most efficient in detecting photons with energies around and below 100 keV, placed at a distance of 5 mm from a carbon cap window with a thickness of 0.6 mm which ensures a good low energy transmission. The position of the detectors, and dimensions of the HPGe crystals are given in Table 3.7. A schematic illustration and a photograph of one of the LEPSs is shown in Figure 3.9 (right and middle).

A photon passing through the HPGe crystal creates electron-hole pairs along its path. By applying an electric field the motion of the pairs generate a signal which is proportional to the energy of the photon[15]. The LEPS detectors were manufactured with an embedded preamplifier, ensuring low noise contribution which results in a better energy resolution. In this way, each LEPS provides a signal amplified by the preamplifier. Further processing of the signals will be described in Section 3.4.4. In the present experiment, the detectors were polarized with an electric field of 2 kV and were cooled down with liquid nitrogen to a temperature of 77 K to prevent, due to the small band gap of ∼0.7 eV, thermal generation of charge carriers which would at room temperature lead to a degradation of the energy resolution.

The performance of the LEPS detector has the advantage of being sensitive for the detection of not only K x-rays but also of L x-rays [Fre11]. The resolution of 0.43 and 0.63 keV at 6 and 122 keV, respectively, was measured by the detector manufacturer. The absolute efficiency has its peak of ∼1.7% at the energy of 46.6 keV and a rapid drop towards higher energies, see Section 5.3.2. A maximum count rate of ∼59 kHz was reached without a significant loss of resolution [FAC+19]. The response of the detectors and the digital electronics were tested and optimized for high count rates of low-energy x-rays expected during the experiment. The results of the test are reported in Section 4.3.

3.4.3 The AGATA γ-ray spectrometer

The Advanced GAmma Tracking Array (AGATA) is a large scale European project to develop and construct a new generation high precision 4π γ-ray tracking spectrometer [AAA+12, KAB+20]. It was started in the late 1990s. Its main goal is to provide an improved geometical efficiency and a high resolving power by means of the combination of a sphere of highly segmented HPGe detectors, Pulse Shape Analysis (PSA) and a tracking algorithm allowing altogether to reconstruct the interaction path of the γ-rays through the HPGe crystals. Figure 3.10 shows a design of the spectrometer configuration consisting of 180 hexagonal HPGe crystals resulting in nearly 4π solid angle coverage. Thanks to the European collaboration composed of over 40 institutions from 12 countries the AGATA demonstrater [GFVD+11], with 1/12 of the full solid angle coverage, became operational in 2009. Since then, it is operated in scientific campaigns at LNL (2010 - 2011), GSI (2012 - 2014) and GANIL (2015 - 2021) to take advantage of various beams and instruments possessed by these laboratories. At GANIL, the spectrometer was employed in several sub-campaigns for nuclear structure, nuclear reaction and nuclear astrophysics studies, together with the VAMOS++ spectrometer, the MUGAST array [ACL+21] and the NEDA-DIAMANT detectors [VDJG+19, SAA+97] using high-intensity stable ion beams as well as RIBs from the SPIRAL1 facility. The scientific results obtained in this campaign are briefly summarized on the GANIL website [GANa]. In future, it is planned to use AGATA at the new RIB facilities like FAIR, SPIRAL2,

[15]This is true only if the photon is completely absorbed within the crystal

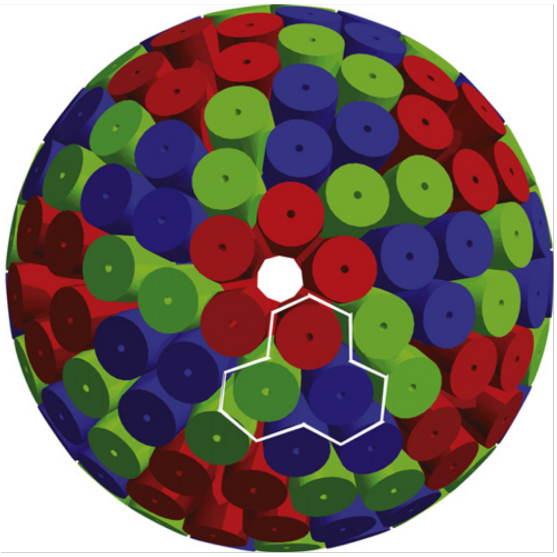

Figure 3.10: Design of the AGATA spectrometer with 180 detector configuration covering a 4π solid angle [AAA+12]. The cryostats and the detector encapsulation are not shown. The white line represents one ATC detector (see text for details).

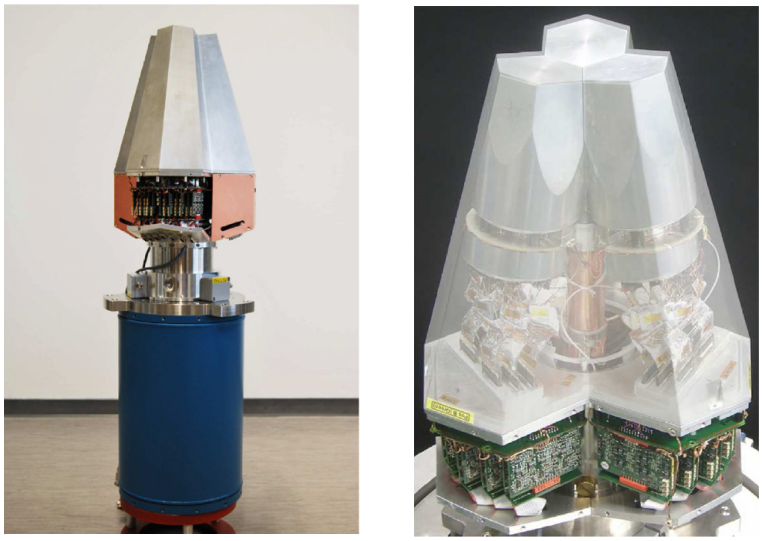

Figure 3.11: Left: The AGATA Triple Cluster with the partially removed cover of the warm part preamplifiers and its 38 cm long Dewar allowing to work for ~8 hours without refill. Right: closer view on the ATC with graphically edited transparent end cap showing the three encapsulated crystals and the cold part of the preamplifiers [WHB+10].

SPES and HIE-ISOLDE. As of 2021, the spectrometer has been returned to LNL. It is presently functioning with a solid angle coverage of $\sim 2\pi$ and will be expanded over time towards the full 4π. The construction of its $\sim 3\pi$ system is foreseen to be finished by 2030.

The final 4π configuration of the AGATA spectrometer will consist in 60 AGATA Triple Clusters (ATC). Figure 3.11 shows pictures of an ATC. Each of them contains three differently shaped tapered hexagonal coaxial n-type HPGe crystals with a thickness of 9 cm and a diameter of 8 cm at the rear. The surfaces of the crystals are very delicate and, therefore, each crystal is encapsulated in a sealed aluminum case with a thickness of 0.8 mm. Figure 3.12 shows a schematic illustration of the three different crystal shapes together with their dimensions. Each crystal is electrically divided into 36 segments, with 6 rings in depth and 6 sectors in each ring, providing an independent signal each. In addition, the core of each crystal provides two signals with different gains with a range of 5 and 30 MeV. All signal channels are equipped with charge-sensitive preamplifiers (PAs) designed specially to meet a number of spectrometer requirements such as good energy and timing properties as well as recording unperturbed signal traces for the PSA and high counting rate capability (>50 kHz). The segment PAs are divided into cold and warm parts. The former is operated close to the liquid nitrogen temperature of the cryostat while the latter operates at room temperature. Despite the high density of electronic components a cross talk of only 10^{-3} was found between the segments within a HPGe crystal while the observed value between the different HPGe crystals is as low as less than 10^{-5} [WHB+10]. Figure 3.13 shows the segmentation of one AGATA crystal. In the present experiment, the spectrometer was operated with 36 crystals placed in the normal configuration at a distance of $\sim$23 cm from the target covering a solid angle of around 13%.

A photon interacting with the HPGe crystal generates electron-hole pairs that are accelerated by the influence of an electric field towards the electrodes. In the AGATA spectrometer, the generated electrons and holes are collected by the core and segment electrodes, respectively. The 38 signals (36 segment + 2 core) produced in each crystal are amplified by PAs. Then, signal traces are digitized by 14-bit Flash ADCs with a sampling rate of 100 MHz. Then, the sampled data are sent to preprocessing electronics in which the amount of data from digitizers is reduced by a factor of $\sim$100 by extracting and processing data only for the segments which registered photon interaction. The energies of the detected photons are determined using a digital trapezoidal filter. In the present experiment, the trapezoidal filter with a risetime of 5 μs was used as a trade-off between the expected high count rate and the required energy resolution. A detailed discussion of the trapezoidal filter will be given in Section 4.3. The reduced data from the preprocessing electronics are then sent to the PSA farm [AAA+12, VB04] where the individual interaction positions of the photons are identified. Treatment of the position, energy and time information of all the individual interactions by tracking algorithms [LMHK+04] allows to perform a reconstruction of the interaction path and the full energy of the original photon on an event-by-event basis. Moreover, the angle of emission of the photon is determined precisely from the first interaction point of the

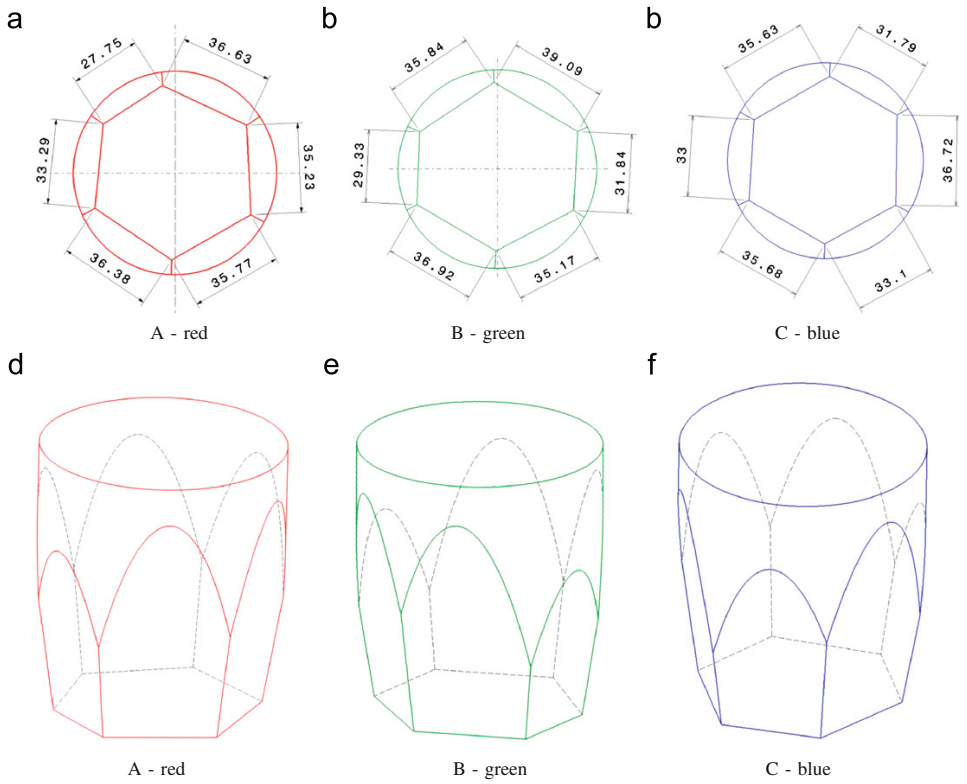

Figure 3.12: Schematic drawing of the three different crystal shapes (red, green, blue) forming one AGATA Triple Cluster. Dimensions are given in mm [WHB+10].

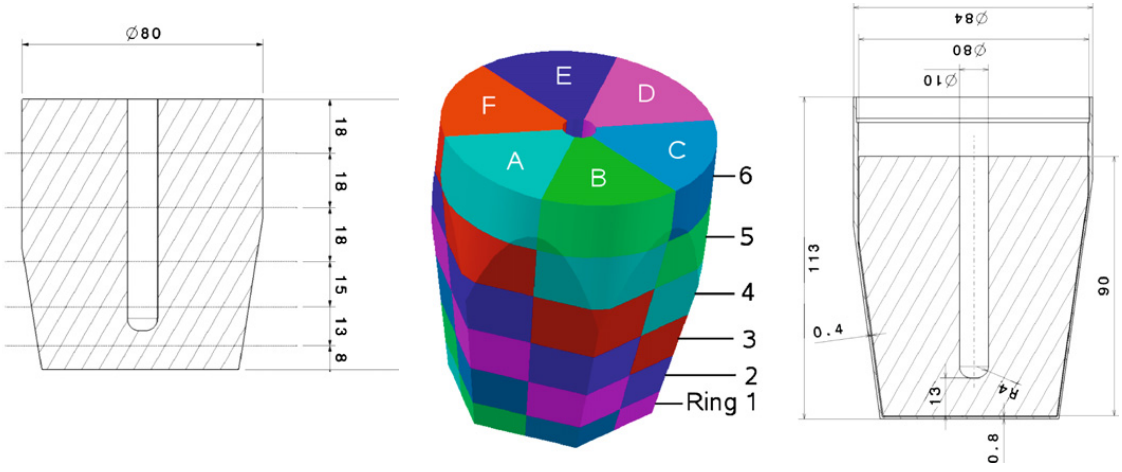

Figure 3.13: Drawing of segmentation and encapsulation for one AGATA crystal. The crystal is divided into six rings labelled 1–6. Each ring is subdivided into six sectors labelled A–F. Dimensions are given in mm [WHB+10].

paths. It allows to obtain an improved Doppler correction of the energies of the photons.

The experiment of the present work is one of the last experiments at GANIL where AGATA was used. Its goal was to identify the atomic charges of the reaction products by measuring the emitted K x-rays (primary) and to possibly measure new transitions for more exotic channels (secondary) if required statistics are accumulated. Its power to measure x-ray yields of uranium-like nuclei, which are of our interest, were demonstrated previously in the MNT reactions of ^{136}Xe + ^{238}U at 1 GeV [VBR+15]. The spectrometer will also help to verify the mass numbers by known γ-ray transitions as it was done for the ^{207,208,209}Pb isotopes in the MNT reactions of ^{208}Pb + ^{100}Mo at 6.25 MeV/A [RGS+17, RCG+19].

The AGATA spectrometer provides an energy resolution of around 2 keV [Joh15] and an absolute efficiency with a peak of around 6% [PV19] at 122 keV, near the region of interest of K x-rays of uranium-like nuclei. The count rate capability of each of the HPGe crystal is currently limited to 50 kHz of rate due to PSA processing [AAA+12].

3.4.4 Electronics

In this section, details of the electronics chain used to process the signals from the detectors of the VAMOS++ spectrometer and the ID-Fix array will be presented. The electronics chain of the AGATA spectrometer was briefly described in Section 3.4.3. In the present experiment, it was of interest to perform a coincident measurement of x-rays and γ-rays, detected by ID-Fix and AGATA, associated with the neutron-rich light actinides measured with VAMOS++. Therefore, the electronics chain was configured to process and store events from ID-Fix and AGATA registered in coincidence with the ones from VAMOS++. This, in turn, helps to reduce the saturation of the PSA processor farm of AGATA and the dead time of the data acquisition.

The readout of the VAMOS++ and ID-Fix detectors was carried out in a digital way using NUMEXO2[16] [Tri] digitizers. Each digitizer was independently connected to the GTS[17] [BBC+13] system which was responsible for tagging timestamps and clock distribution. The tagged timestamps were used to correlate the digitizers with a fast decision module TGV[18], which controls the triggering of the data acquisition, via the BEAST[19] [Bou] module. The coupling with the AGATA electronics was handled with the AGAVA[20] [AAA+12] module using timestamps and trigger decisions distributed by the GTS system [CMd+17]. The management of the data flow of VAMOS++, ID-Fix and AGATA, and writing to storage disks was performed using the NARVAL[21] [GCC+05, CMd+17]

[16] French: NUMeriseur pour EXOgam2; English: Digitizer for EXOgam2
[17] Global Trigger and Synchronization
[18] French: Trigger Generique VME; English: VME Generic Trigger
[19] Back End Adaptor for Synchronization by Timestamp
[20] AGATA VME Adapter
[21] French: Nouvelle Acquisition temps-Réel Version 1.2 Avec Linux; English: New Real-time Acquisition

Table 3.8: List of the NUMEXO2 digitizers used in the present experiment for the VAMOS++ spectrometer and the ID-Fix array. The details for the TAC modules are given in Table 3.9.

#	NUMEXO2 ID	Detection system	Description	Channels used
1	63	VAMOS++	Tracking DPS-MWPC$_{1,2}$	1-2, 3-4
2	60		Tracking MWPPAC$_1$	1-12
3	61		Tracking MWPPAC$_2$	1-12
4	116		Timing DPS-MWPC$_{1,2}$	14, 15
5	58		Timing MWPPAC$_1$	1-8
6	109		Timing MWPPAC$_2$	1-8
7	110		Timing MWPPAC$_{1,2}$	1-4, 5-8
8	57		TAC$_{1-8}$	1-8
9	59		IC	1-7
10	107	ID-Fix	LEPS$_{1,2,3}$	2, 6, 10

data acquisition system.

Each of the NUMEXO2 digitizers contains 8 Fast Analog to Digital Converters (FADC) which sample signals from 16 channels with a frequency of 100 MHz. The signals are sent to the digitizers via two single-ended to differential converter (B3) boards, having 8 channels each, and an HDMI cable with a length of 10 m. The B3 boards are placed close to the detectors and convert the signals into a differential mode in order to reduce noise contributions and interferences to transmit the signals over such a long distance [ECHB+15]. Both the digitizers and the B3 boards were developed at GANIL. Each NUMEXO2 digitizer has a specific firmware depending on the measurand. In the present experiment, ID-Fix and VAMOS++ were equipped with a total of 10 digitizers: one for the three LEPS detectors, 7 for the tracking and the timing wire planes of the DPS-MWPCs and the MWPPACs, 2 for the Ionization Chamber (IC) and the Time-to-Amplitude Converter (TAC) modules. The NUMEXO2 digitizers used in the present experiment are listed in Table 3.8. Figure 3.14 shows the scheme of the electronics chain for the signals from the different detectors of VAMOS++ and ID-Fix.

The **TAC** modules are used to measure the time interval between two fast logic input signals, Start and Stop, and generate an analog output signal proportional to the measured time. In the present experiment, eight TAC modules were used to measure the time of flight of the particle or the photon between the different detectors. The details of the two input signals coming from the detectors together with the ranges of the TAC modules are listed in Table 3.9. The output signals of the TAC modules are sent to the NUMEXO2 digitizer with a dedicated firmware, see Figure 3.14.

The **timing** wire planes provide a total of 42 signals: t_1^{tp} and t_2^{tp} signals from the first and the

Version 1.2 With Linux

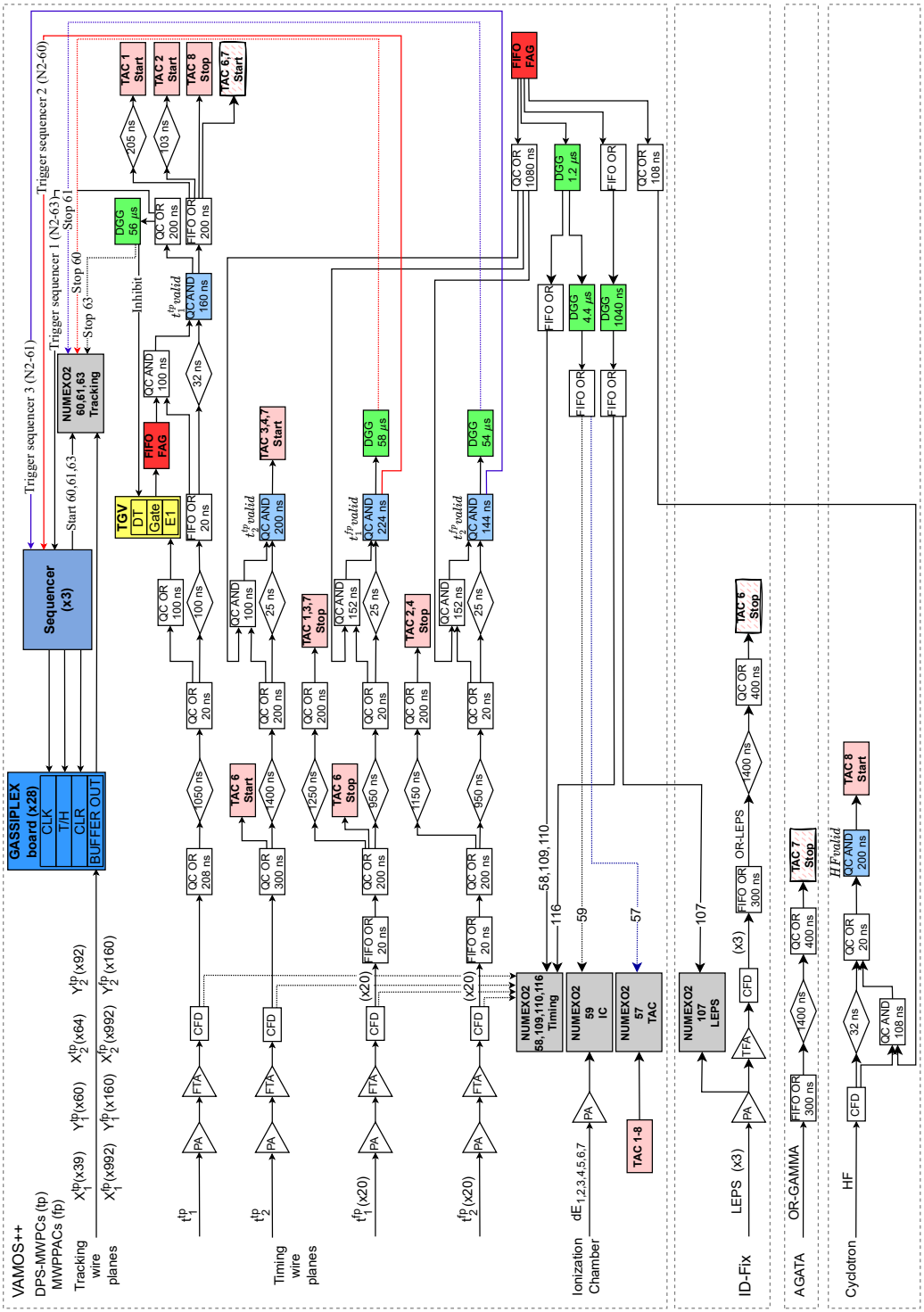

Figure 3.14: Electronic scheme for the VAMOS++ and ID-Fix signals together with the OR-GAMMA and HF (see text for details). The labels (tp) and (fp) refer to the DPS-MWPCs at the target position and the MWPPACs at the focal plane, respectively.

second timing wire planes of each of the DPS-MWPCs, and t_1^{fp} and t_2^{fp} from the 20 sections of the first and the second timing wire planes of each of the MWPPACs. Each signal is amplified in a preamplifier (PA) and then in a Fast Timing Amplifier (FTA). Later, it is sent to a Constant Fraction Discriminator (CFD) whose threshold was adjusted in such a way as to eliminate the noise contribution of the wires and to accept the induced charge that is split between two neighbouring time sections, consequently, resulting in a signal with lower amplitude. The effect of the split signal and its correction during the analysis will be discussed in Section 5.2.1.4. Afterwards, a fast logic signal coming from the CFD is sent in two separate ways. One is sent to the NUMEXO2 digitizer with a dedicated firmware. The second signal from each of the timing wire planes is processed in a number of ways for different purposes briefly described in the following (see Figure 3.14 for the complete scheme). (1) The t_1^{tp} signal triggers the TGV module which produces a Fast Analysis Gate (FAG) signal. The fast logic signals from all the VAMOS++, ID-Fix and AGATA detectors are accepted only if they are validated by the FAG signal which launches the readout of the data. Sufficient enough delay was introduced to the primary signals of the different detectors in order to synchronize them to perform a coincidence measurement. (2) The t_1^{tp} was also used to generate a gate signal which serves as a Dead Time (DT). It was validated by the FAG and processed through a Dual Gate Generator (DGG) producing the gate signal with a width of 56 μs needed for the readout of the position wires. Then, the gate signal, during which no events are accepted by the acquisition, was sent to the TGV module. A major contribution of around 60 μs is due to the DT comes from the readout of the position wires. (3) All of the signals except t_2^{tp}, validated by the FAG, trigger the readout of the position wires and are used to generate gate signals, with DGG modules, during which readout takes place. Both the trigger and the gate signals, which are named as Stop 60, 61, 63 in Figure 3.14, are sent to the NUMEXO2 digitizer with a dedicated firmware. (4) The logic signals were sent to the TAC modules for the time of flight measurement, see Table 3.9.

The charges induced by the particles on the **tracking** wire planes of the DPS-MWPCs ($X_{1,2}^{tp}$, $Y_{1,2}^{tp}$) and MWPPACs ($X_{1,2}^{fp}$, $Y_{1,2}^{fp}$) are integrated and multiplexed with GAS SIlicium multiPLEXing chips (GASSIPLEX) [SBB+94, SM01] and V551B sequencer modules. The chips are accommodated on a board with 6 slots, a low voltage supply and 4 channels for signals, namely Clock (CLK), Track-/Hold (T/H), Clear (CLR) and Output (BUFFER OUT). Triggered by the validated fast logic signals t_1^{tp} *valid*, t_1^{fp} *valid* and t_2^{fp} *valid*, the sequencer modules send the CLK, T/H and CLR signals to the chips. The CLK distributes a sequence of signals for each of the wires allowing to operate the stored charges multiplexed on a single output signal. The T/H switches between recording the maximum charge induced in each wire and storing the values in the sequence defined by the CLK. The CLR resets the chips to restore their initial values for processing the next event. One board handles 96 wires, 16 wires per chip, and provides a single multiplexed output signal BUFFER OUT. The BUFFER OUT is sent to the NUMEXO2 digitizer with a dedicated firmware where de-

[22] t_2^{tp} - t_1^{fp}(no V) with 2 μs range. no V means without a FAG validation (after change)
[23] t_2^{tp} *valid* - t_1^{fp} with 2 μs range (after change)

Table 3.9: List of the TAC modules, the ranges and the two input signals provided by the different detectors. The input signals and the ranges of the TAC #6 and #7 were changed during the experiment due to the the beam energy change, from $E_{beam} \simeq 7.2$ MeV/A to $E_{beam} \simeq 6.8$ MeV/A, which shifted and broadened the region of interest. The use of TAC #5 was not in the scope of the present work and, therefore, its parameters were not given here.

TAC	Description		Range
	Start	Stop	(μs)
1	t_1^{tp} *valid*	t_1^{fp}	1
2	t_1^{tp} *valid*	t_2^{fp}	1
3	t_2^{tp} *valid*	t_1^{fp}	1
4	t_2^{tp} *valid*	t_2^{fp}	1
6[22]	t_1^{tp} *valid*	OR GAMMA	1
7[23]	t_1^{tp} *valid*	OR LEPS	0.5
8	*HF valid*	t_1^{tp} *valid*	0.2

multiplexing of the signal takes place based on the sequence of the CLK signals, which are named as Start 60, 61, 63 in Figure 3.14, and the maximum charges induced in each of the wires are obtained. The measured distribution of the charges allows to obtain the position of the particle, see Section 5.2.1.1. Figure 3.15 (right and left) shows the board with a view of the signal channels and the GASSIPLEX chips inserted in the board.

The **IC** has 7 pads in depth providing $\Delta E_{1,2,3,4,5,6,7}$ signals proportional to the energy deposited by the particle. The signals are processed by capacitors and then sent directly to the NUMEXO2 digitizer where by means of the trapezoidal filter, having a flat top of 1 μs and a risetime of 1 μs, the energy information is extracted.

Each of the **LEPS** detectors provides two outputs of the signal amplified by PAs. One of the amplified signals of each LEPSs is sent to the NUMEXO2 module to obtain the energies of the detected photons using a digital trapezoidal filter with a risetime of 5 μs. The value of the risetime was chosen based on the source test results reported in Section 4.3. The FAG signal was used to produce a gate signal via a DGG module which was sent to the NUMEXO2 digitizer. The gate signal had a width of around 1 μs during which the events from the LEPSs were accepted. The second signals of each LEPSs are used to generate a common fast logic or signal (OR-LEPS) for a time interval measurement and for monitoring purposes. They are amplified in a Timing Filter Amplifier (TFA) module, evaluated in a CFD module and then sent to a Logic FIFO module which gives the OR-LEPS signal. The signal was delayed by 1400 ns, was transformed to a signal with a width of 400 ns by a Quad Coincidence (QC) module and sent to the TAC module to measure the

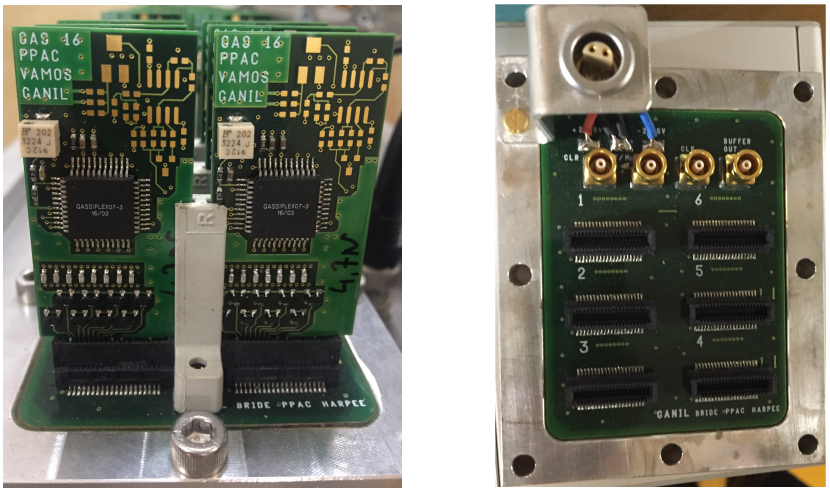

Figure 3.15: Right: Photograph of the board showing the slots for 6 GASSIPLEX chips, a low voltage supply and signal channels: CLK, T/H, CLR and BUFFER OUT (see text for details). Left: Photograph of the chips accommodated on the board. Each chip can handle 16 wires making it 96 wires per board.

time of flight of the photon emitted by the particle detected in VAMOS++.

OR-GAMMA and High Frequency (HF) are fast logic signals. The OR-GAMMA signal comes from the different HPGe crystals of AGATA and was produced in a similar way as the OR-LEPS signal. The HF signal is provided by each cycle of the cyclotron delivering the beam and was validated by the FAG. Both of them were sent to the TAC modules.

The output of all of the logic signals were used for inspection and were sent to the Universal Marker Module (U2M) [BS00] to monitor the counting rate without dead time coming from the data acquisition.

Chapter 4

Tests of the ID-Fix array

Contents

4.1 Introduction

The experiment of the present work relies on the atomic charge identification method involving characteristic x-ray spectroscopy. This method, however, is very sensitive to the x-ray and γ-ray background associated with the atomic and nuclear de-excitations of the ^{238}U + ^{238}U reaction products. Therefore, given the high-intensity ^{238}U beam, it is very important to optimize the performance of the ID-Fix x-ray detection array of the three LEPS detectors and the NUMEXO2 digitizer in terms of both the efficiency and the resolution at the expected experimental conditions of high counting rate of background events, see Section 3.4.2 for the description of the array. As a preparation for the experiment, source and in-beam tests were carried out. The first source test was performed during my master degree internship in 2018 and was reported in Ref. [DU19, FAC+19]. It demonstrated that the LEPS together with the NUMEXO2 digitizer can handle the maximum counting rate of 59 kHz while keeping a rejection rate below ∼30%. The successive in-beam test was carried out in 2019. Its major objective was to investigate photon absorbers of various thicknesses in order to reduce the aforementioned background events and their pile-up. Another source test was performed in 2021 for an extensive study of the trapezoidal filter of the NUMEXO2 digitizer to optimize the response of the LEPS detector for the counting rates of several tens of kHz. In this chapter, the analysis and results of these tests will be presented.

4.2 The in-beam test: absorber studies

Four absorber thicknesses were tested in-beam in the experimental hall G2 at GANIL, see Figure 3.2, using the beam of $^{238}U^{58+}$ at about half of the nominal beam energy of 3.8 MeV/A and an intensity of 2.5 - 3 nA (0.04 - 0.05 pnA) impinging on a sandwiched target of metallic ^{238}U with a configuration of ^{12}C-^{238}U-^{12}C having a thickness of 55-627-10 μg/cm^2. The tested absorber thicknesses are the following:

- 1.5 mm aluminum
- 2.0 mm aluminum
- 2.5 mm aluminum
- 1.5 mm aluminum + 0.5 mm titanium

The conditions regarding beam delivery and target manufacturing were similar to those of the experiment, see Section 3.2 and 3.3 for details, respectively. The targets were mounted on a wheel inside the chamber shown in Figure 4.1 (top left). The detection setup consisted of two silicon detectors, one LEPS detector and one EXOGAM clover [SAdF+00] detector. The silicon detectors were used to measure the recoils and were mounted inside the chamber at a distance of 39.1 cm and 45.4 cm covering a solid angle of 1.15 msr and 2.78 msr, respectively. Both of them operated in vacuum and were placed at θ = 21.5° and 47.1° (partly used) with respect to the beam direction.

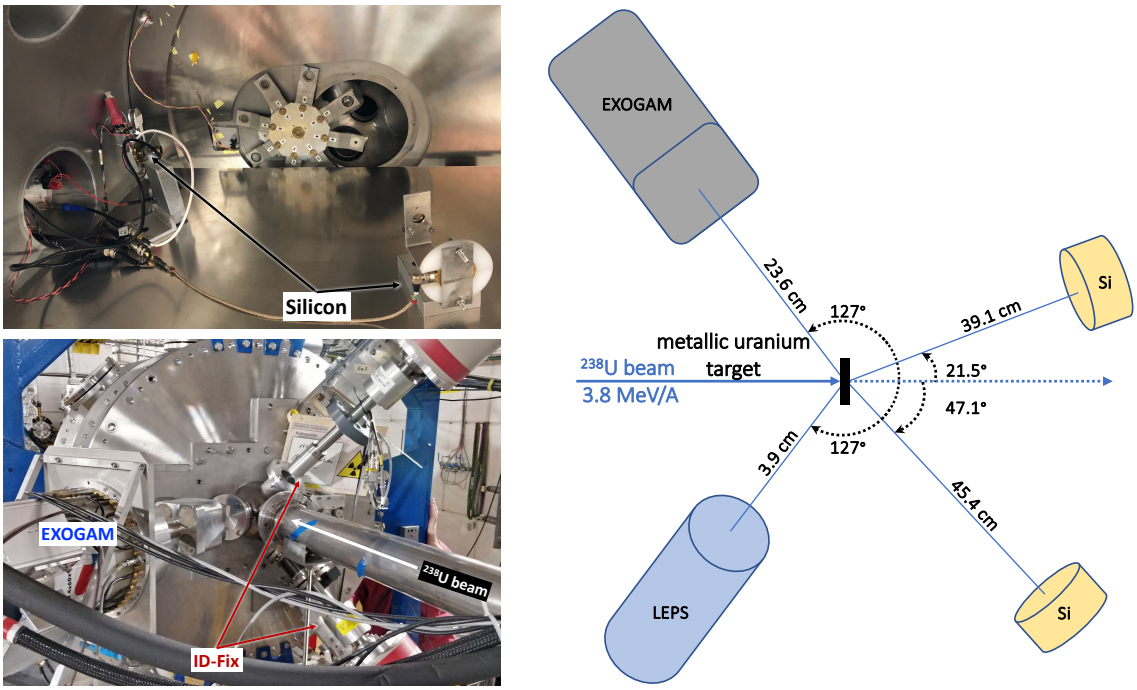

Figure 4.1: Top left and bottom left: Photographs of the setup taken in the experimental hall G2 at GANIL. Top: Internal view of the chamber with the 8-position target wheel in the background, the first silicon detector at 21.5° in the foreground, and the second silicon detector in the left corner still at 69.2° which was later replaced by a silicon detector at 47.1°. Bottom: External view of the chamber, and the view on the EXOGAM clover detector on the left and the two LEPS detectors on the right side. The upper LEPS mounted in air, facing the target through an aluminum window with a thickness of 1.5 mm, and the lower one mounted inside the vacuum. Technical issues related to the liquid nitrogen auto-fill system restricted to the use of only one of the LEPSs, to the one in vacuum which was later placed in air. Right: Schematic diagram of the setup illustrating the distances of the detectors with respect to the target and the angles relative to the beam direction.

Table 4.1: Geometrical characteristics of the detectors employed in the in-beam test including the distances from the target position and their solid angle.

Detector	Distance (mm)	Active area (mm^2)	Solid angle (msr)
Silicon detector at 21.5°	391	176	1.15
Silicon detector at 47.1°	454	572	2.78
LEPS detector in air / vacuum	38.8[24] / 79.2	580	353 / 90
EXOGAM clover detector	236	3600	64.5

X-rays and γ-rays emitted from the recoils were detected by the LEPS detector and the EXOGAM clover ($60\times60\times90$ mm^3) detector, see Figure 4.1 (bottom left). The latter played the role of AGATA (d_{rear} = 80 mm, 90 mm), as a large volume HPGe detector, to estimate the counting rate expected during the experiment. Both the LEPS and the EXOGAM detectors were mounted at the same polar angle θ =127° with respect to the beam direction but at different azimuthal angles. The initial place of the LEPS was at ϕ = 150° in vacuum and then it was changed to ϕ = 30° in air inside an insert with a 1.5 mm aluminum window facing the target. The photon spectra were measured for each of the absorbers by placing them inside the "doigt de gant", see Section 3.3, in front of the LEPS. The EXOGAM detector was kept fixed in air at ϕ = 270° also facing the target through a 1.5 mm Al window. The signals from preamplifiers of all the detectors were treated using the NUMEXO2 digitizer, see Section 3.4.4. The geometrical characteristics of the detectors used in the test are given in Table 4.1. Figure 4.1 (right) shows a schematic illustration of the detection setup. The calibration of the detectors, the analysis of the collected data and obtained results will be reported in the following.

4.2.1 Detector calibration

During the in-beam test experiment we had a misfunction of the liquid nitrogen filling system and network problems. The latter made it impossible to initialize the NARVAL data acquisition system, see Section 3.4.4. Only after many attempts and a reduction of the NARVAL actors to the absolute minimum, a working system could be created. As a consequence, the configuration of recorded spectra of all the detectors have the same energy value in eV for two different values in ADC channels before and after the network problems. Therefore, there are two different calibration parameters obtained from the calibration runs for the measurements before and after the network problems, respectively. Given that the spectra of the various absorbers for the LEPS were taken after the network problems, only the calibration runs recorded after the experiment are useful.

For the calibration of the silicon detectors spectra were taken using 3-line α and ^{252}Cf sources

[24]The distance from the target increases, decreasing the solid angle, when an additional absorber is placed

Table 4.2: Energies of the ^{252}Cf fission fragments obtained after the calibration of the silicon detector at 21.5° (top) and 47.1° (bottom). The values of the FWHM as well as the literature energy values for the corresponding fragments are given.

Fragment	This work		Ref. [CLR02]
	E_{ff} (MeV)	FWHM (MeV)	E_{ff} (MeV)
Heavy	80.23(4)	32.37(9)	80.0
Light	105.73(4)	16.09(6)	105.7

Fragment	This work		Ref. [CLR02]
	E_{ff} (MeV)	FWHM (MeV)	E_{ff} (MeV)
Heavy	80.02(4)	32.95(12)	80.0
Light	105.76(4)	16.77(5)	105.7

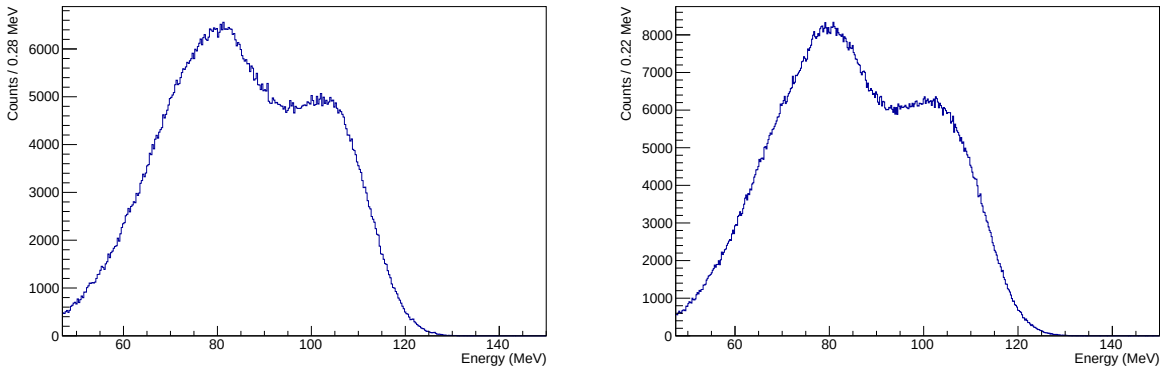

Figure 4.2: The spectra of heavy and light fission fragments of ^{252}Cf after the calibration procedure of the silicon detector at 21.5° (left) and at 47.1° (right).

before and after the experiment, respectively. Being the only useful one, the calibration procedure with the ^{252}Cf source will be described in the following. The details for the calibration procedure using the 3-line α source is, nevertheless, given in Appendix A.1. Spontaneous fission of ^{252}Cf leads to a broad distribution of heavy fragments and light fragments with average energies of 80.0 MeV and 105.7 MeV [CLR02], respectively (see Figure 4.2). Figure 4.3 (left and right) shows the outcome of the linear fit to the data. The energy distribution of the fission fragments is between 16 and 33 MeV (FWHM) with 15 - 40% error bars in an energy range from 80 to 105 MeV (see Table 4.2).

For the calibration of the LEPS detector and the EXOGAM clover detector a source of ^{152}Eu was used. From the raw spectra the centroids of photopeaks were extracted assuming that they follow a Gaussian distribution. Then, the centroids were used to find the relation between channel

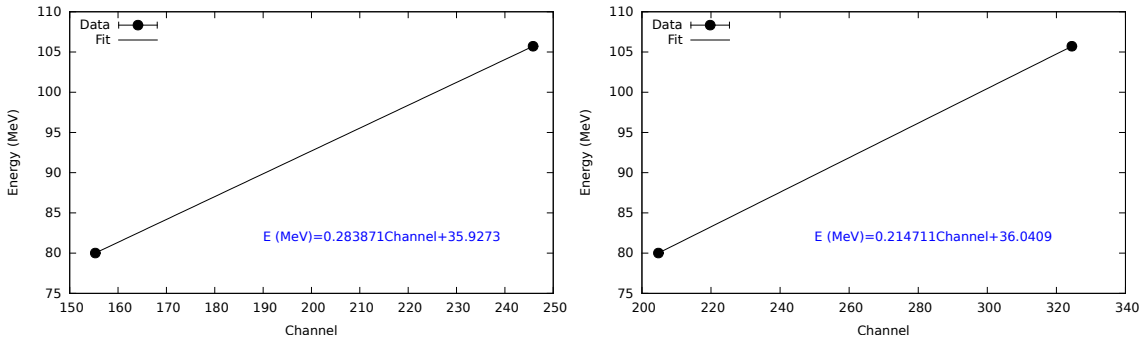

Figure 4.3: Energy-to-channel calibration curves of the silicon detector at 21.5° (left) and 47.1° (right) using the ^{252}Cf source. The statistical errors are smaller than the symbol size.

Table 4.3: Peak parameters of the ^{152}Eu x-rays and γ-rays obtained after the calibration of the LEPS detector (1) and EXOGAM clover detector (2). The values of the FWHM as well as the literature values for the corresponding peaks are also given.

Radionuclide	This work				Ref. [Zieb]
	$E_{x,\gamma}^{(1)}$ (keV)	FWHM$^{(1)}$ (keV)	$E_{x,\gamma}^{(2)}$ (keV)	FWHM$^{(2)}$ (keV)	$E_{x,\gamma}$ (keV)
^{152}Eu	39.7	1.7	39.8	2.9	39.9
	45.5	1.3	45.5	3.1	45.7
	122.1	1.4	121.9	2.6	121.7
	245.3	1.5	244.6	2.6	244.7
	344.9	1.5	344.1	2.7	344.3
	411.7	1.2	410.7	2.8	411.1
	444.1	1.6	443.6	2.8	443.9
	778.5	1.7	779.1	2.8	778.9
	867.2	1.8	867.7	3.0	867.4
	963.9	2.0	964.3	3.0	964.1
	1087.7	1.8	1086.1	3.3	1085.8
	1111.5	2.0	1112.1	3.1	1112.1
	1406.8	2.7	1407.9	3.3	1408

values and the well-known energies of x-ray and γ-ray transitions of ^{152}Eu. Figures 4.4 (b-e) and 4.5 (left) show the linear fit together with the resulting calibration equations for the EXOGAM clover detector and the LEPS detector, respectively. Note that only those photopeaks with a well defined Gaussian shape were considered for the relation. The spectra of ^{152}Eu after the calibration procedure of the EXOGAM clover detector and the LEPS detector are shown in Figures 4.4 (a) and 4.5 (right), respectively. The resolution of the detectors is given in Table 4.3.

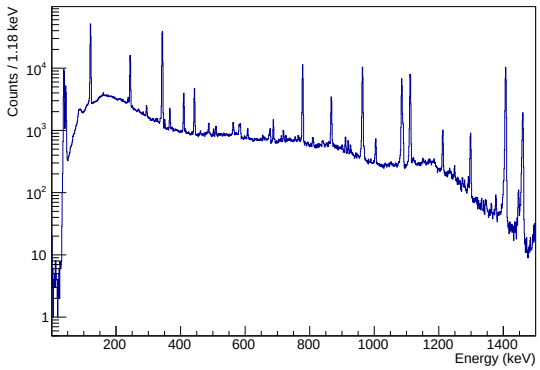

(a) EXOGAM A spectrum

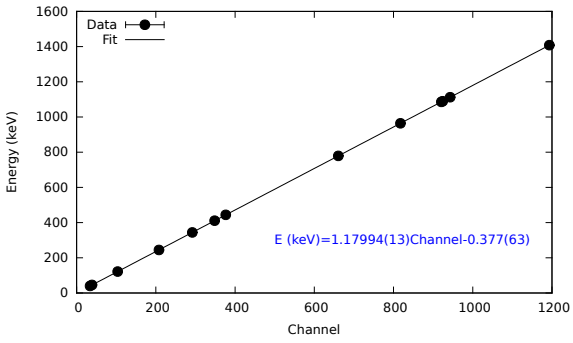

(b) EXOGAM A

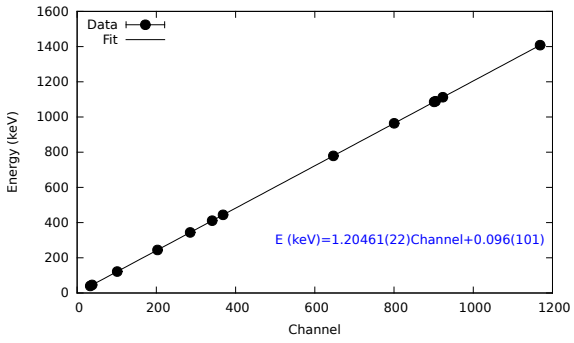

(c) EXOGAM B

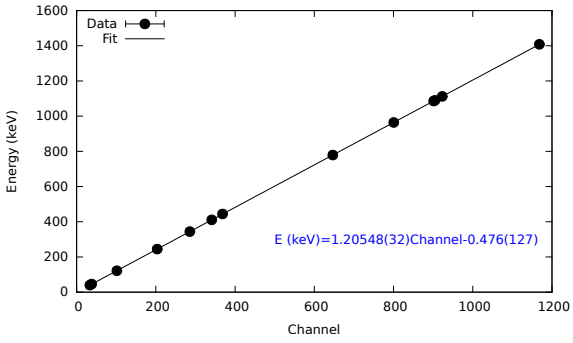

(d) EXOGAM C

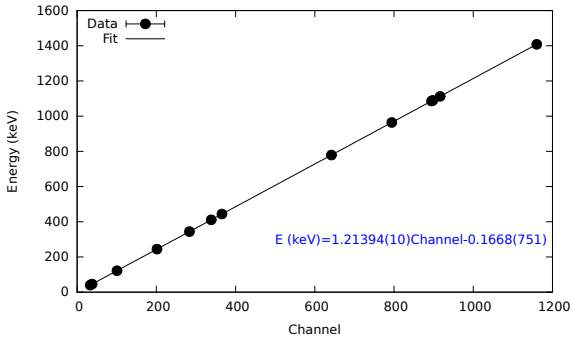

(e) EXOGAM D

Figure 4.4: Calibrated spectrum of ^{152}Eu taken in EXOGAM A crystal (a). Energy to channel calibration curve of the indicated EXOGAM crystals (b-e). The incorporated statistical errors are smaller the symbol size.

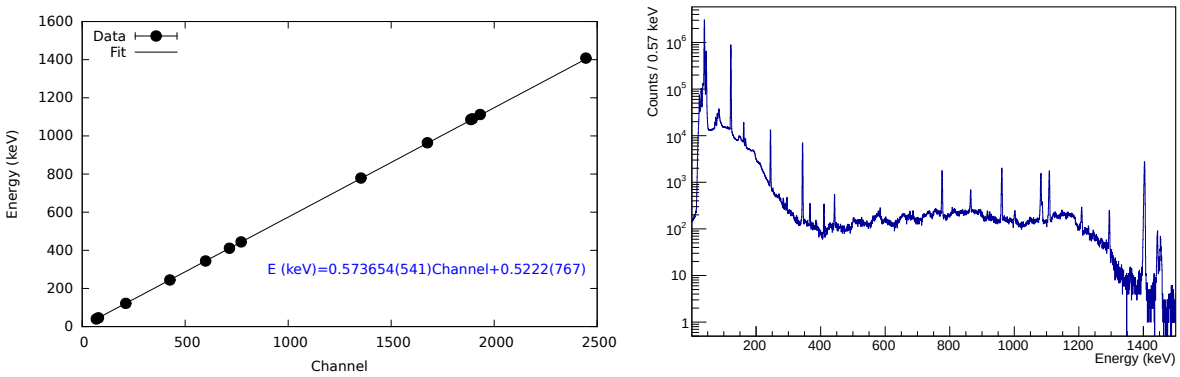

Figure 4.5: Left: Channel-energy calibration curve of the LEPS detector. The incorporated statistical errors are smaller than the symbol size. Right: Calibrated spectrum of ^{152}Eu measured with the LEPS detector.

4.2.2 Data analysis

Despite the previously mentioned misfunction of the liquid nitrogen filling system and the network problems, which restricted data taking to 5 out of 8 hours of the requested beam time, the major aim of this test was achieved thanks to the help from both the GANIL technical staff and the collaboration members. In this section, the data collected with the silicon, the LEPS and the EXOGAM clover detectors will be presented.

Figure 4.6 shows the energy spectra of the reaction fragments measured with the silicon detectors at 21.5° and 47.1°. The ^{238}U peak corresponds to both the beam-like and the target-like fragments which have the same energy value at a given angle. From more forward (E = 664(3) MeV at 21.5°) to more backward angles (E = 229(2) MeV at 47.1°) the energy decreases, see the reaction kinematics in Figure 4.12 (left). The yield of ^{238}U at 21.5° is around 70 times higher than that of ^{12}C whereas at 47.1° they become comparable. The two peaks at around 180 MeV for 21.5° and around 90 MeV for 47.1° correspond to the ^{12}C backing (upstream), onto which the ^{238}U target was evaporated, and the ^{12}C layer (downstream), with which the target was covered, see the target properties in the beginning of Section 4.2. At the region near the energy threshold there is also a peak at around 50 MeV for both silicon detectors. It corresponds to the electrons emitted from the atomic excitation of the reaction partners. The smaller peaks in the tale of the ^{238}U and ^{12}C towards higher energies, see Figure 4.6 (left), are probably caused due electronics issues as they were optimized not for the silicon detector but for the LEPS detector.

Figure 4.7 (left) shows the photon spectra measured with the LEPS detector in vacuum without any absorber. Given the count rate limitation of the detector, apart from two bumps at around 20 keV and 100 keV, there are no distinct peaks due to pile-up of the events from the overwhelm-

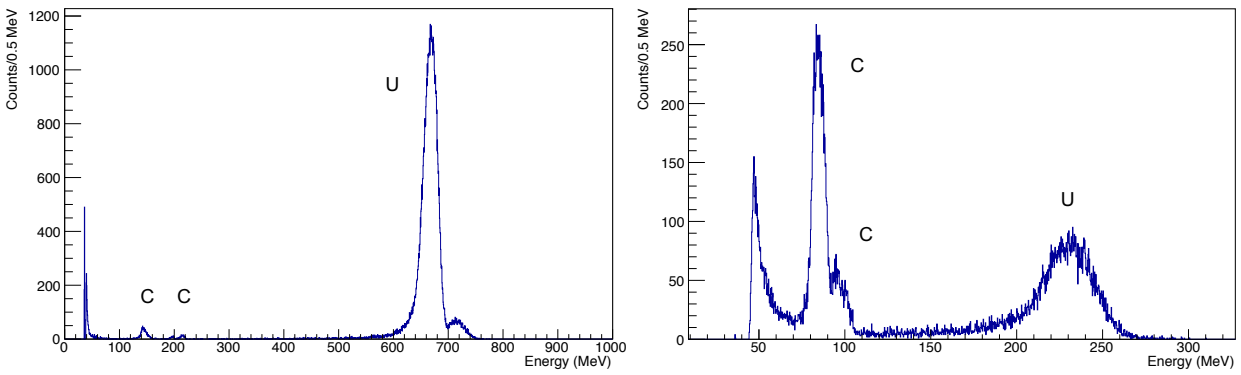

Figure 4.6: Silicon spectra at 21.5° (left) and 47.1° (right). The peaks corresponding to the ^{238}U and ^{12}C recoils are indicated. In the left figure, the smaller peaks in the tale of the ^{238}U and ^{12}C towards higher energies are probably caused due electronics issues as they were optimized not for the silicon detector but for the LEPS detector.

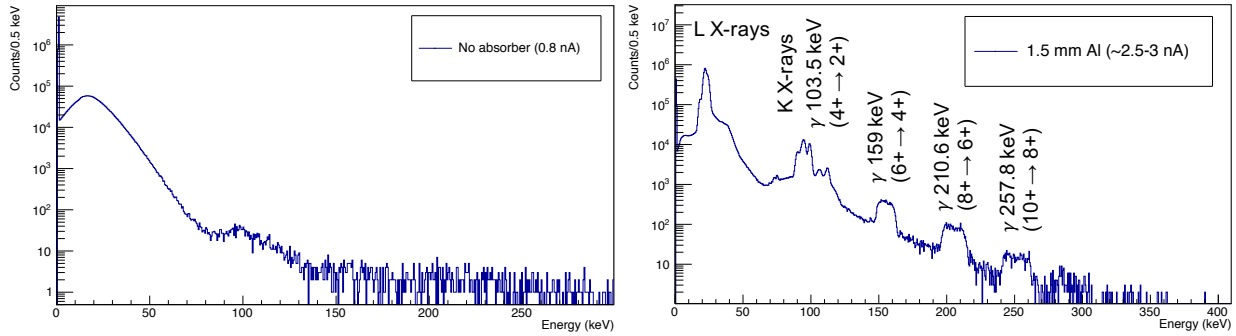

Figure 4.7: Photon spectra measured with the LEPS detector with (right) and without (left) an aluminum absorber of 1.5 mm. The peaks corresponding to photons emitted by ^{238}U recoils are indicated.

ing background of atomic low-energy transitions. The use of an additional absorber of 1.5 mm thick aluminum, in contrast, allows to observe different peaks by attenuating this low energy background, see Figure 4.7 (right). The presence of peaks around 20 keV is associated with the non-separated L_α, L_β and L_γ x-rays of ^{238}U. A bump is clearly visible at around 40 keV. It corresponds to the region where the de-excitation of the rotational band from 2^+ to 0^+ is expected. Several peaks at around 100 keV are visible. They come from the γ transition of the rotational band from 4^+ to 2^+ as well as the K_α and K_β x-rays of ^{238}U. There are 3 bumps, in the region from 150 to 300 keV, resulting from the γ de-excitation of the various rotational band members, see Table 4.4, which are expected to be at 159, 210.6 and 257.8 keV. The observed peaks are broadened due to the Doppler effect. For the photons with higher energies the absolute broadening is higher which is demonstrated by the increase of the width for the ^{238}U rotational band transitions. The Doppler effect correction will be discussed in the following.

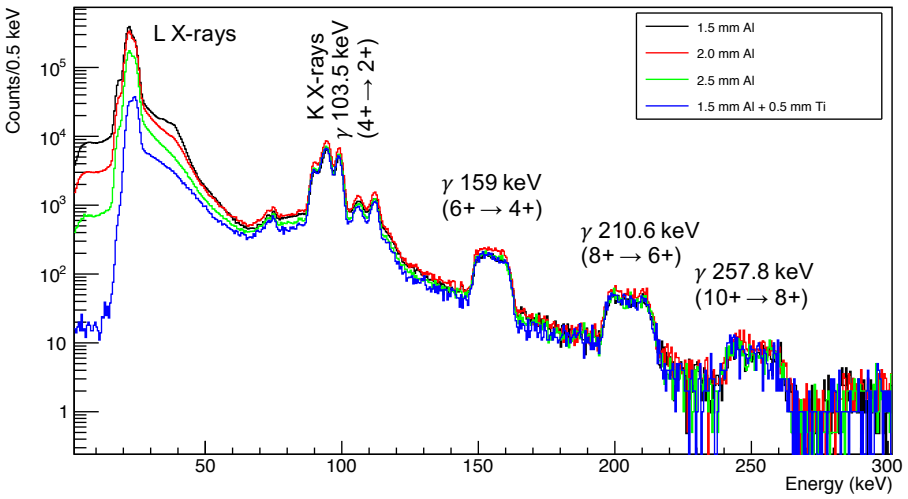

Figure 4.8: Photon spectra measured with the in-air mounted LEPS detector for various absorbers. The peaks corresponding to photons emitted by ^{238}U recoils are indicated.

Figure 4.8 shows the photon spectra measured with the LEPS detector, mounted in-air, for the different absorber thicknesses listed in the beginning of Section 4.2. The spectra were normalized to the duration of the measurement for each of the absorbers. It is evident that there is no change in transmission of photons with energies around and higher than 100 keV for the various absorber thicknesses. The effect of larger thickness becomes visible at around 80 keV and it is very distinct below 50 keV. The change in energy threshold is observed below L x-rays energies around 20 keV for increasing absorber thicknesses up to 2.5 mm of aluminum. For 1.5 mm aluminum + 0.5 mm of titanium L x-rays are starting to be suppressed as the threshold shifts to a higher energy region. The measured counting rates for each of the absorber thicknesses and the values estimated for

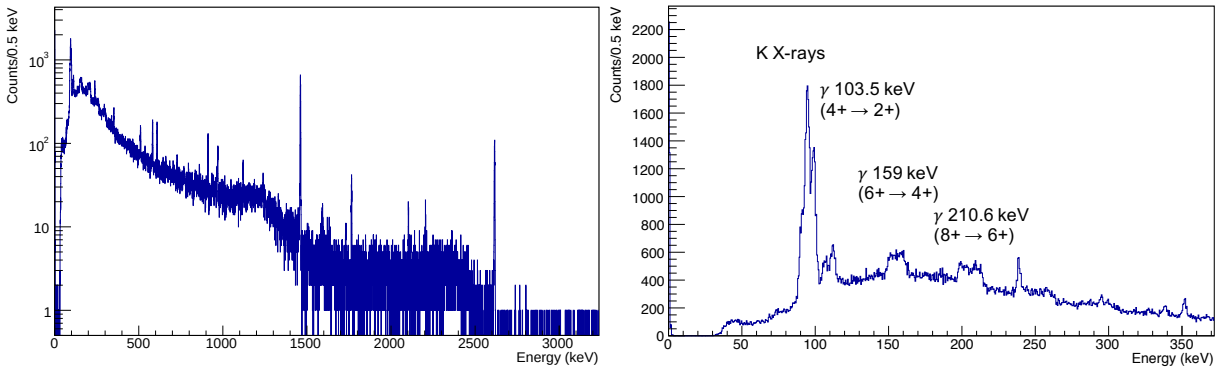

Figure 4.9: Photon spectra measured with one of the EXOGAM clover crystals: the whole spectrum in logarithmic scale (left) and the region of interest in linear scale (right). The peaks corresponding to photons emitted by ^{238}U recoils are indicated.

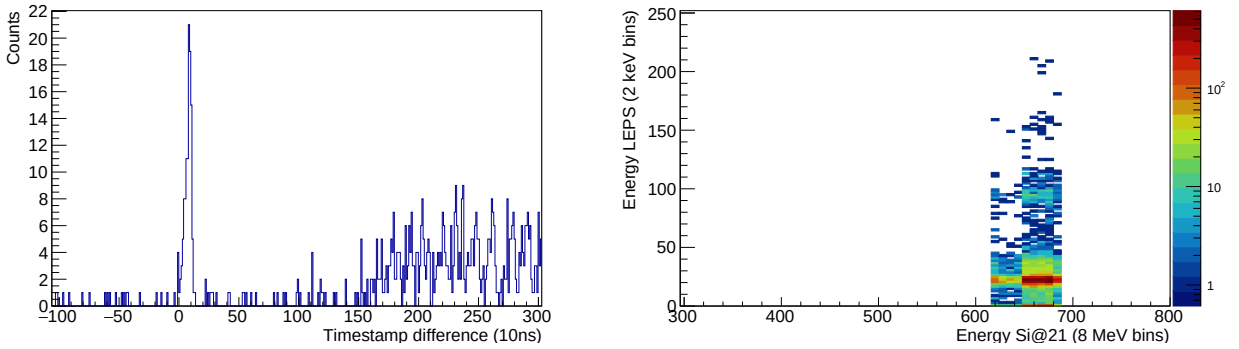

Figure 4.10: Left: Timestamp difference between photons and recoils. The intense prompt peak at around 150 ns and delayed structures of lower intensity are present. Right: Energies of the coincident events detected with the silicon detector at 21.5° and the LEPS detector in air.

the experiment will be further discussed in Section 4.2.3.2.

Figure 4.9 shows the photon spectra measured with one of the EXOGAM clover crystals. X-rays as well as γ-rays of the various rotational band members of ^{238}U are present. In contrast to the LEPS detector, the energy threshold for photons is found to be at around 35 keV, therefore no L x-rays were observed. The yields will be used to estimate the rates expected with the AGATA spectrometer, see Section 4.2.3.3.

In order to suppress the background events and to obtain the photons associated with the ^{238}U recoils only, a coincidence algorithm was applied using timestamps, tagged by the GTS system (see Section 3.4.4) of the events registered by the detectors. In the algorithm, the timestamp difference was built between the recoils detected by the silicon detectors and the photons measured with the LEPS. As an example, Figure 4.10 (left) shows the timestamp difference spectrum of the events from the silicon detector at 21.5° and the LEPS detector. Using the prompt peak of 150 ns as a gate, a 2-D spectrum with energies of the recoils and photons was produced, see Figure 4.10 (right). In order to reduce the amount of random coincidences which could be caused by a contribution of the ^{12}C recoils, an energy gate was put to the ^{238}U region in the silicon detector spectrum. The coincident photons obtained by means of this algorithm are shown in Figure 4.11 (left) together with the inclusive spectrum. The obtained coincidence count rate will be further discussed in section 4.2.3.2.

The measured energies of the detected x-rays and γ-rays are influenced by the Doppler effect and, therefore, need to be corrected. The correction procedure is explained in Section 5.3.3. In addition to the measured energy of the photons, it makes use of the information on the velocity of the recoils and the angle of the detectors. In our case, the velocity of the recoils was obtained from the measured energy event-by-event. As an example, Figure 4.11 (right) shows the photons

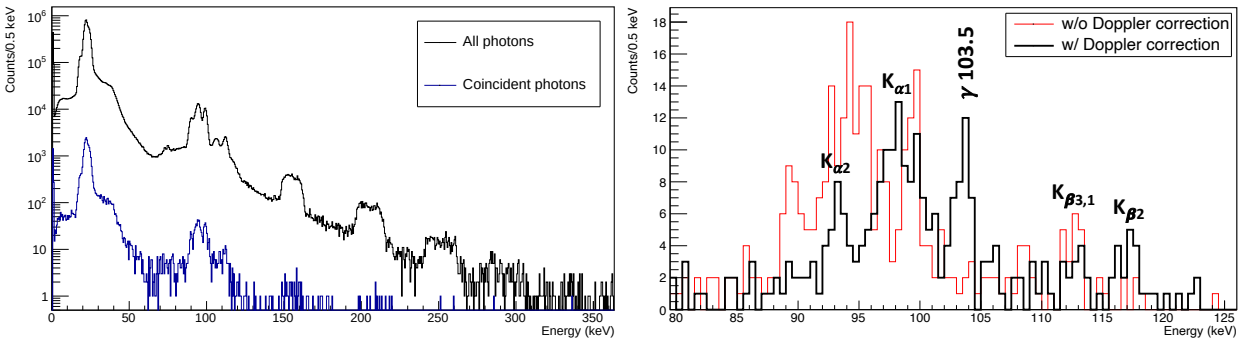

Figure 4.11: Left: Single and coincident photons detected with the LEPS detector. Right: The Doppler corrected energies of the K x-rays and the 103.5 keV γ-ray detected with the LEPS detector in coincidence with the ^{238}U recoils measured with the silicon detector at 21.5°.

Table 4.4: X-ray and γ-ray energies, in keV, of ^{238}U from this work as well as their literature values.

Recoil	X-ray / γ-ray transitions	This work	Ref. [nis, nnd]
^{238}U	K_{α_2}	93.9(8)	94.6
	K_{α_1}	98.4(7)	98.4
	$(4^+ \rightarrow 2^+)$	103.3(7)	103.5
	$K_{\beta_{3,1}}$	110.9(8)	111.3
	K_{β_2}	116.7(9)	114.6
	$(6^+ \rightarrow 4^+)$	160.5(5)	159.018
	$(8^+ \rightarrow 6^+)$	215(7)	210.6
	$(10^+ \rightarrow 8^+)$	259(1)	257.8
	$(12^+ \rightarrow 10^+)$	296(1)	300.6

in the K x-ray region, before and after Doppler correction, measured with the LEPS detector in coincidence with the recoils detected with the silicon detector at 21.5°. The accumulated data allows to observe the presence of the L X-rays and K X-rays as well as the γ transition of the 4^+ to 2^+ rotational band with an energy of 103.5 keV. The Doppler corrected energies of the photons are reported and compared to the literature values in Table 4.4.

4.2.3 Results

4.2.3.1 Comparison of the data on recoils with LISE++

Experimental data on the recoils obtained using the silicon detectors were extracted and compared to the theoretical values calculated with the LISE++ [TB] program. Figures 4.12 (left) and (right)

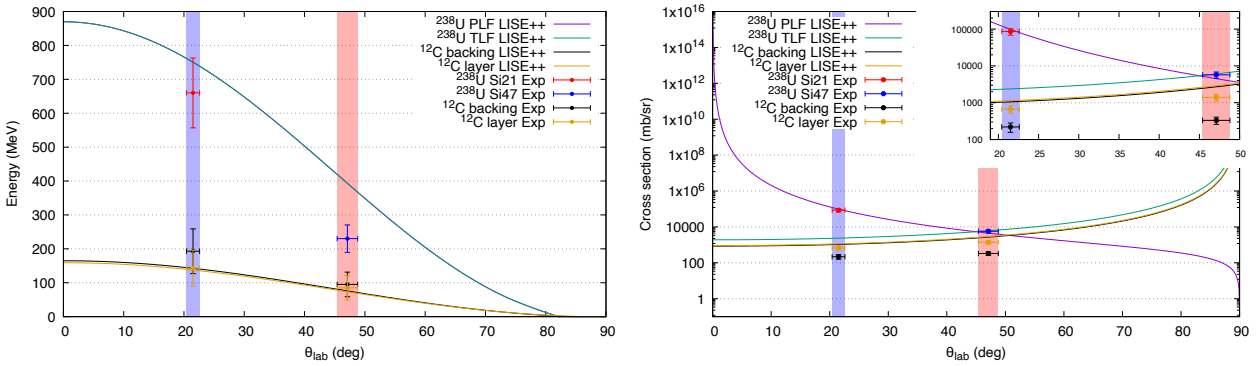

Figure 4.12: Measured and calculated [TB] energies (left) and cross sections (right), with a closer view at the region of interest in the inset, of the indicated reaction products, of the elastic scattering reaction of ^{238}U at 3.8 MeV/A on the metallic ^{238}U, as a function of scattering angles. The curves representing the calculated energies for the beam-like (PLF) and the target-like (TLF) ^{238}U recoils overlap. Shaded areas represent the region covered by the silicon detectors at 21.5° (in blue) and 47.1° (in red). The beam-like ^{238}U recoils scattered by the ^{12}C backing (upstream) and the ^{12}C layer (downstream) travel close to the beam axis ($\theta \leq 5°$) and are beyond the silicon detectors' acceptance they are not presented here.

show a comparison, for the beam-like and the target-like recoils, respectively, of the reaction kinematics and the cross sections for Rutherford scattering. For both 21.5° and 47.1° angles, the calculated energies of the ^{238}U recoils are overestimating the measured ones while for the ^{12}C recoils the values are consistent within the error bars. The overestimation can be explained by the deficiency of energy produced by the pulse height defect (PHD) [Kno79] from the silicon detectors, due to the use of the calibration source, see Section 4.2.1, having a lighter mass compared to that of ^{238}U. It is clear that the PHD observed for ^{238}U recoils is significantly higher and for ^{12}C recoils it is less pronounced. The cross sections for the ^{238}U recoils are in agreement within the error bars. The error bars include the statistical uncertainty and more importantly the uncertainty in the intensity of the beam which was as low as around 0.05 pnA, making it challenging to monitor them at the delivery level. The latter is also reflected in the overestimation of the cross sections for the ^{12}C recoils. The beam-like ^{238}U recoils scattered by ^{12}C backing and ^{12}C layer are not shown as they travel close to the beam direction at $\theta \leq 5°$ and, therefore, are not detected with the silicon detectors.

4.2.3.2 Photon count rate with different absorber thicknesses

The counting rates of photons associated with different absorber thicknesses, listed in the beginning of Section 4.2, were obtained by extracting the yields measured with the LEPS detector

and normalizing them to the duration of the measurement. Figures 4.13 (left) and (right) show the obtained results for the x-rays and 103.5 keV γ-ray emitted from Coulomb excitation of ^{238}U from the single and coincident spectra, respectively. The effect of absorbers for the L x-ray region is more important as compared to the K x-ray one in such a way that the count rate of L x-rays decreases as the thickness of the absorber increases while the transmission of K x-rays for the various absorbers remains the same within the error bars. The error bars represent the statistical uncertainty and the uncertainty from the beam current. The total counting rate of photons measured for the different absorbers is shown in Figure 4.14 (left). Based on these measured values the rates expected for the experiment were estimated by accounting for the beam intensity, the target thickness and the solid angle. From the estimated rates, see Figure 4.14 (right), it is concluded that the absorber of 1.5 mm of aluminum would be sufficient to reduce low-energy background x-rays, to meet the required previously established limit of 59 kHz, allowing at the same time to keep the energy threshold as low as possible, see Figure 4.8. These results were included in the proposal of ^{238}U + ^{238}U experiment resubmitted to the GANIL PAC 2020. A beam time for an additional in-beam test, that could clarify the total count rate and test the setup at the nominal beam energy and at the experimental conditions of VAMOS + AGATA + ID-Fix, was requested but was not allocated by the GANIL PAC.

4.2.3.3 Photon count rate estimation for the AGATA spectrometer

The total count rate of around 0.1 kHz was obtained from the spectra measured with the EXOGAM clover detector. Using this number the total count rate expected for the AGATA spectrometer at the normal configuration was estimated at the experimental conditions with the beam intensity of 1 pnA and taking into account the solid angle coverage difference between a single HPGe crystal of EXOGAM and AGATA. The rate was estimated to be 8(6) kHz per crystal which does not exceed the count rate limitation of the spectrometer.

4.3 The source test: trapezoidal filter studies

The performance of the Moving Window Deconvolution (MWD) or the trapezoidal filter [JK94] implemented in the NUMEXO2 [Tri, ECGT+15] digitizer, processing the signals from the LEPS detector, were tested in the experimental hall G2 at GANIL, see Figure 3.2, using the "two-sources-method" [Kno79]. This method involves a high-intense ^{60}Co source and a source of ^{152}Eu which mimicked the experimental conditions of the photons of interest in the presence of a high photonic background. The trapezoidal filter has four different parameters:

- K (risetime)
- M (flat top)

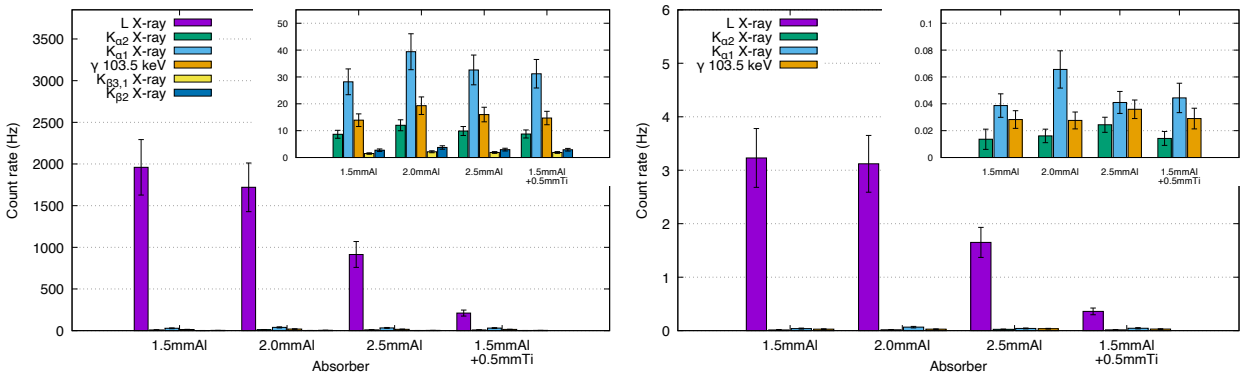

Figure 4.13: Counting rate of L x-ray, K x-ray and 103.5 keV γ of ^{238}U as a function of various absorbers. Error bars indicate the statistical uncertainty and the uncertainty coming from the beam intensity. The insert presents a zoomed-in view for the K x-ray and γ-ray region. Left: All photons detected by the LEPS detector. Right: Photons measured by the LEPS detector in coincidence with recoil ions measured by the silicon detectors.

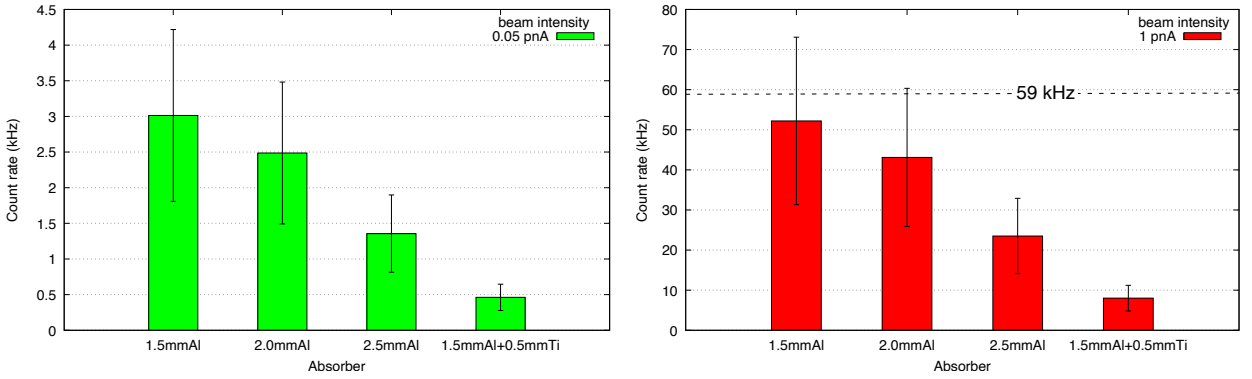

Figure 4.14: LEPS x-ray rates estimated for the experiment for 1 pnA (right) based on the measured values in the in-beam test at around 0.05 pnA (left). The dashed line indicates the counting rate limit of the detector at 59 kHz.

- N (average energy window)
- Q (computing delay)

These parameters are configured in the GECO[25] program and have to meet the following conditions: M > N, Q > K and K + M > Q + N. Figures 4.15 (top left) and (bottom left) show the trapezoidal filter together with its parameters represented in the user-friendly interface of the GECO program and on the oscilloscope, respectively.

The response of the LEPS detector was recorded by scanning the possible values of the parameters and by varying the distance of the ^{60}Co source, to obtain the necessary count rate, while the position of the ^{152}Eu source was kept fixed, see Figure 4.15 (right). As an example, Figure 4.16 shows the measured spectra of ^{152}Eu with and without the ^{60}Co source. One can see in the measurement of ^{152}Eu with ^{60}Co that the Compton background coming from the ^{60}Co source

[25] GANIL Electronic COntrol

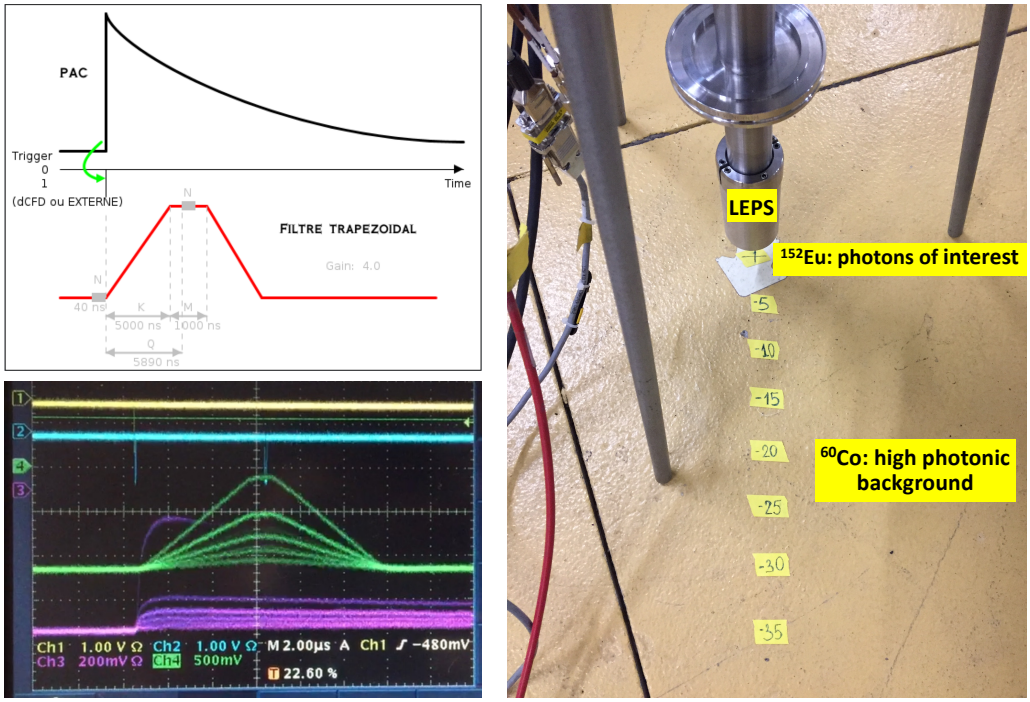

Figure 4.15: View of signal conversion in the GECO program (top left) and the oscilloscope (bottom left). The program demonstrates the preamplifier in the top panel and the trapezoidal signal, with its parameters, in the bottom panel. On the oscilloscope, the preamplifier signal is in purple and the trapezoidal one is green. Right: The LEPS detector and the positions of the ^{152}Eu source and the high intense ^{60}Co source. The different distances indicate the positions of the ^{60}Co source to obtain the necessary count rate.

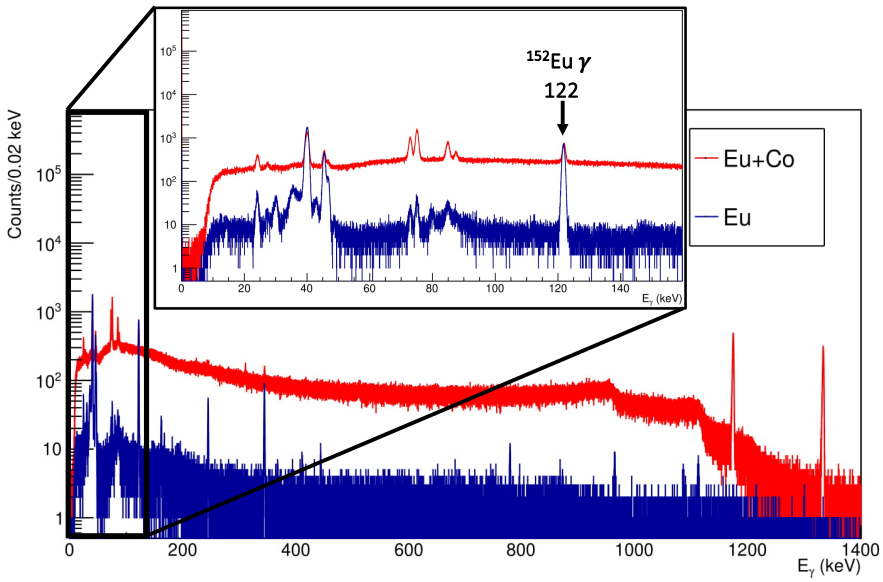

Figure 4.16: Spectrum of ^{152}Eu without and with the ^{60}Co source, at ∼15 cm distance, measured using the LEPS detector. The arrow points at the 122 keV γ-ray peak of ^{152}Eu used as a reference.

overwhelms the ^{152}Eu peaks. This is also true for the 122 keV γ-ray peak of ^{152}Eu which was used as a reference as it lies near the energy region of K x-rays of uranium-like nuclei. The resolution and the efficiency (ε) for the peak of reference was extracted for each set of the tested values of the risetime, flat top, average energy window and computing delay at the count rates from 1 to 40 kHz. The resolution is expressed in (keV) as full width at half maximum (FWHM)

$$\mathrm{FWHM} = 2\sigma\sqrt{2ln2} \tag{4.1}$$

where σ is the standard deviation of the peak assuming that it follows a Gaussian distribution. The efficiency ε and its error bar $u(\varepsilon)$ are given by

$$\varepsilon = \frac{m - b_m}{n - b_n} \qquad \text{and} \qquad u(\varepsilon) = \varepsilon \cdot \sqrt{\left(\frac{u(m - b_m)}{m - b_m}\right)^2 + \left(\frac{u(n - b_n)}{n - b_n}\right)^2} \tag{4.2}$$

where m and n are the rates of the peak of reference with and without the ^{60}Co source, respectively, and b_m and b_n are the associated background rates. Figures 4.17 (left) and (right) show the obtained results for various rates for the risetimes of 2.5, 5 and 10 μs for all the three LEPS detectors, see specifications of the detectors in Section 3.4.2. At low rates of ∼10 kHz, it is clear that the longer the risetime, the better the resolution and the lower the efficiency, due to the increase of the pile-up rejection. The increase of the rate leads to the steady loss of both resolution and efficiency for all the risetime values. However, at the rates of ∼20 kHz and higher the resolution for 10 μs experiences a more dramatic degradation compared to the other two risetimes, showing that the trapezoidal filter of the digitizer has a limited capability and is not able to perform at such

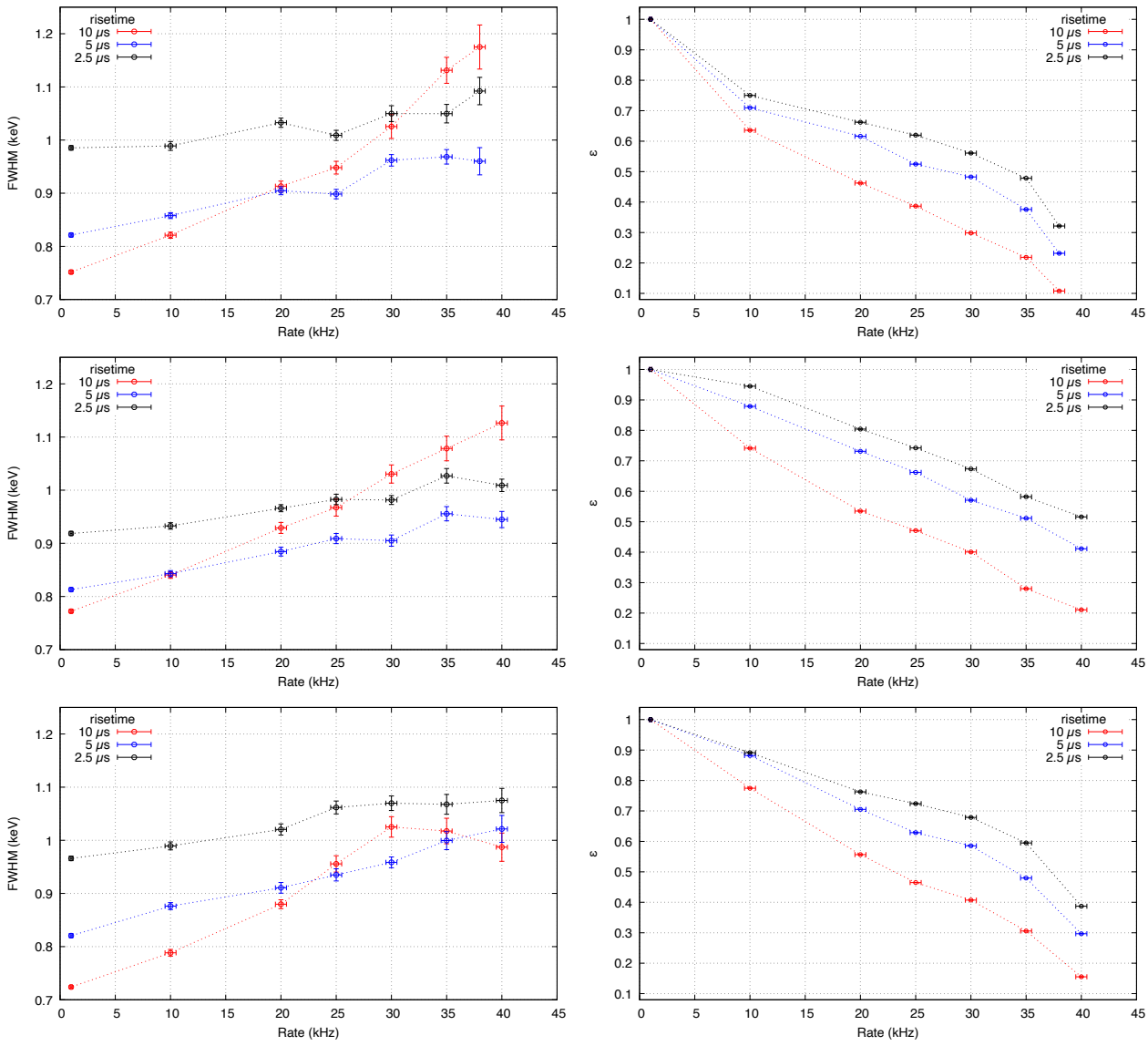

Figure 4.17: The resolution (left) and the efficiency (right), of the LEPS #1, #2 and #3 from top to bottom, respectively, as a function of different rates for the risetimes of 2.5, 5 and 10 μs. Dotted lines serve as a guide to the eye.

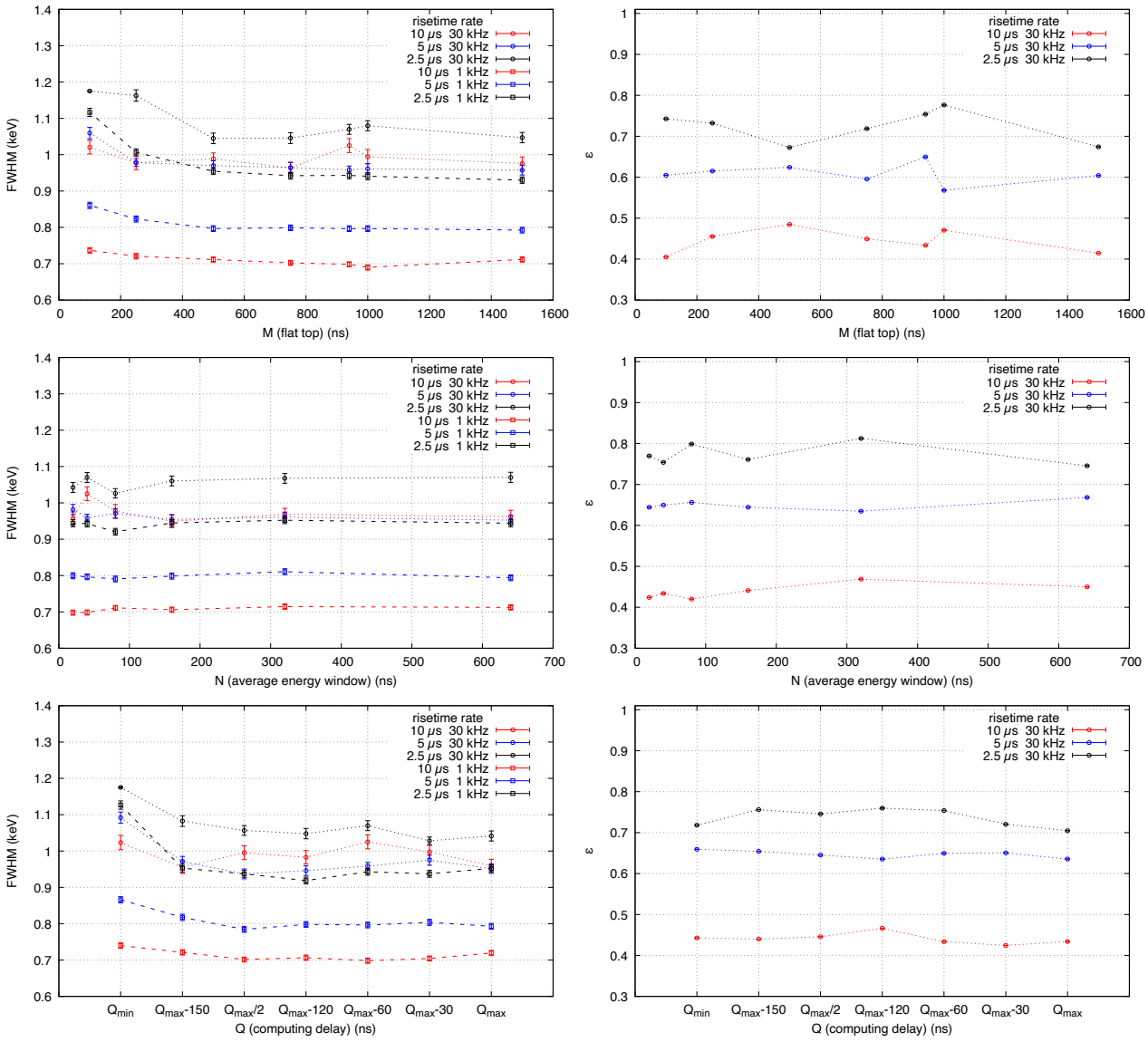

Figure 4.18: The resolution (left) and the efficiency (right), of one of LEPS detector, as a function of different values of the flat top (top), the average energy window (middle) and the computing delay (bottom) for the rates of 1 and 30 kHz and for the risetimes of 2.5, 5 and 10 μs. Dashed and dotted lines serve as a guide to the eye.

Table 4.5: Optimum parameters of the trapezoidal filter chosen for the experiment.

Parameter	Value (ns)
K (risetime)	5000
M (flat top)	1000
N (average energy window)	40
Ϙ (computing delay)	5890

high rates. For the rates of ∼35 - 40 kHz, the rejection rate is more than 40% for both 5 and 2.5 μs while providing a resolution of lower and higher than ∼1 keV (FHWM), respectively. Within the risetime value of either 2.5, 5 or 10 μs and at the rate of 30 kHz, the other parameters such as the flat top, average energy window and the computing delay are less critical to the response of the detector performing within ±0.2 keV (FWHM) in resolution and ±5% in efficiency as shown in Figures 4.18 (left) and (right), respectively. To keep a reasonable resolving power, a risetime of 5 μs was chosen, for the experiment[26]. The optimum values for all the parameters of the trapezoidal filter obtained based on the results of this test are reported in Table 4.5.

For AGATA, a test of the different risetime values of the trapezoidal filter was performed by Emmanuel Clement with a source of ^{203}Hg. It showed that the risetimes 2.5, 5 and 10 μs provide the resolution of 2.5, 2,1 and 2.9 keV (FWHM) at 80 keV while introducing a "dead time" of 15, 30 and 50% in the count rate range of 30 - 50 kHz, respectively [Cle21]. Similar to ID-Fix, the risetime of 5 μs was chosen for the trapezoidal filter of the AGATA signal processing.

[26]The present source test is not 100% suitable for our goals since the x-ray distribution of the uranium-like nuclei and the background are not the same, and does not allow to find the required resolution to resolve the different x-ray peaks.

Chapter 5

Data Analysis

Contents

5.1 Introduction

In the period of 10 days from 20th to 29th May 2021, the experiment investigating MNT cross sections was performed using a beam of ^{238}U at energies of 6.765 and 7.193 MeV/A impinging on a 615 μg/cm^2 ^{12}C-sandwiched metallic uranium target. The experiment suffered from various problems on the accelerator side, see Section 3.2. Nevertheless, it was possible to obtain partly the requested 1 pnA of beam intensity and accumulate ∼1.5 days of equivalent beam dose on target, instead of the requested 7 days, and collect data with the unique combination of VAMOS++, AGATA and ID-Fix.

In this chapter, the analysis of the data collected with each of the detection system will be presented. It will provide first the description of the calibration procedure of the detectors, and then the identification of the reaction products in charge state q and mass A with VAMOS++, and in atomic charge Z with ID-Fix and AGATA via the detection of characteristic x-rays.

5.2 Analysis of VAMOS++ data

VAMOS++ allows to identify a particle in atomic mass A, charge state q and atomic charge Z combining the information provided by a versatile detection system and employing a trajectory reconstruction technique [PRN+08, PCJ+08] based on the ion optics of the spectrometer. The detection system of the spectrometer, including the processing of measured signals, was described in detail in Section 3.4.1. The trajectory reconstruction technique will be described in Section 5.2.1.3.

The diagram of the identification algorithm of the spectrometer is shown in Figure 5.1. The step-by-step description of the algorithm is provided in the following:

i) The positions ($X_{1,2}^{tp,fp}$ and $Y_{1,2}^{tp,fp}$) are determined from the first and the second DPS-MWPC detectors at the entrance (tp), and the first and the second MWPPAC detectors at the focal plane (fp) of the spectrometer. Using the determined positions, the image of the target and the focal plane in terms of positions ($X_{tp,fp}$ and $Y_{tp,fp}$) and angles ($\theta_{tp,fp}$ and $\phi_{tp,fp}$) are obtained. Then, the obtained image information is utilized to reconstruct the magnetic rigidity (Bρ) and the distance (D) traveled by the particle between the entrance DPS-MWPC and the focal plane MWPPAC detectors.

ii) The timing signals provided with the two entrance DPS-MWPC detectors (tp) ($t_{1,2}^{tp}$) and the two focal plane MWPPAC detectors (fp) ($t_{1,2}^{fp}$) allow to obtain the time of flight (TOF) measurement. The obtained TOF is combined with the distance D between the corresponding entrance and the focal plane detectors to determine the velocity (υ), β and γ via $\upsilon = D/TOF$, $\beta = \upsilon/c$ and

$\gamma = 1/\sqrt{1-\beta^2}$, respectively.

iii) The mass over charge ratio (A/q) can be reconstructed combining the magnetic rigidity Bρ and the velocity υ, since the motion of the particle in the magnetic field (B) is defined by the equation for the Lorentz force as

$$\frac{A\upsilon^2}{\rho} = q\upsilon \times B \tag{5.1}$$

and if υ is perpendicular to B then A/q is equal to

$$\frac{A}{q} = \frac{B\rho}{\upsilon}. \tag{5.2}$$

iv) The mass (A_{raw}) can be calculated using the information on the kinetic energy measured with the IC detector as follows

$$A_{raw} = \frac{E}{u\,(\gamma - 1)} \tag{5.3}$$

where $E = E_{nm}$ + E_{IC} is the total kinetic energy given as a sum of the total energy released in the IC detector $E_{IC} = \sum_{n=1}^{7} \Delta E_n$ with n segments together with the deduced, not measured, energy E_{nm} deposited in the different layers of the material before the IC detector, u = 931.5016 MeV/c^2 stands for the energy value for one atomic mass unit.

v) The combination of A/q and A_{raw} allows to obtain the charge state (q)

$$q_{raw} = \frac{A_{raw}}{A/q}, \tag{5.4}$$

which, in turn, allows to reconstruct the mass (A), with the precision higher than the one of A_{raw}, as

$$A = q_{raw}^{int} \times A/q \tag{5.5}$$

where $q_{raw}^{int} = |q_{raw} + 0.5|$ is the integer value of q_{raw}.

Typically, the atomic charge Z is obtained using the energy loss ΔE, governed by the Bethe-Bloch equation [Kno79], and the total energy E_{IC} of the particle provided by the IC detector. In the present experiment, VAMOS++ was not used for the atomic charge identification due to the limited resolution of $\Delta Z/Z \simeq 1/66$ (FWHM) to determine the uranium-like products of interest. It was used for the identification of their atomic mass only. The mass resolution of $\Delta A/A \simeq 1/263$ (FWHM) [RGS+17] was achieved at VAMOS++. However, the focal plane MWPPAC detectors had been newly installed before the experiment. With these detectors, the mass resolution of $\Delta A/A \simeq 1/301$ (FWHM) is simulated, making it possible to identify the masses of uranium-like products of interest. In the following sections, the calibration procedure of the various VAMOS++ detectors for obtaining the abovementioned physical information, and the analysis of the data to extract the atomic mass and the charge state will be given.

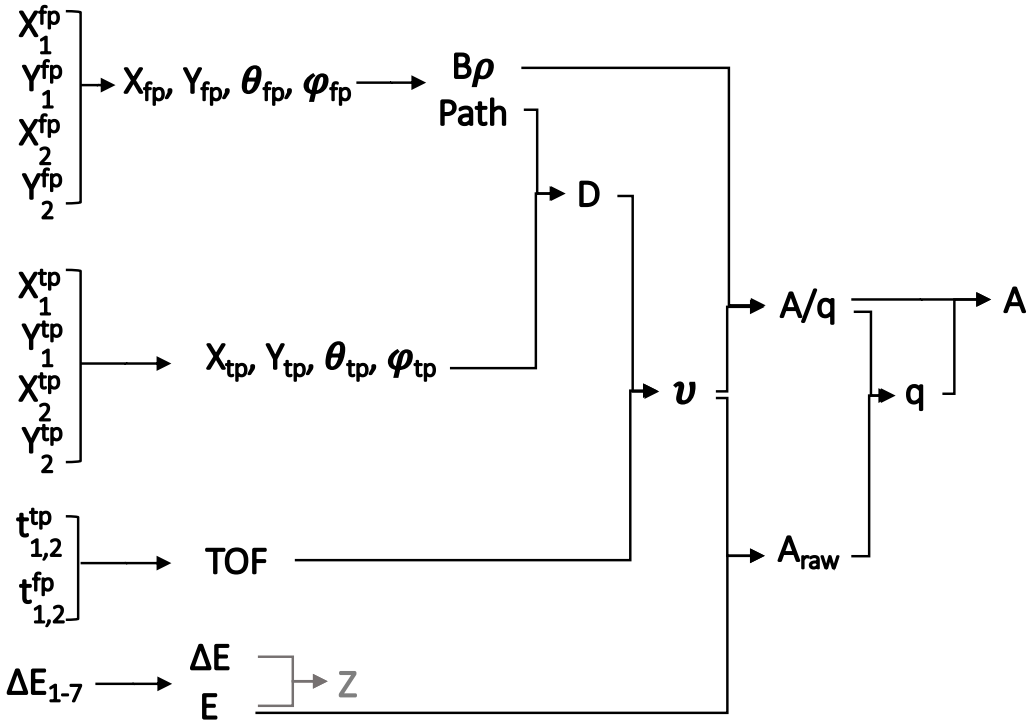

Figure 5.1: Diagram of the identification algorithm of the VAMOS++ spectrometer, see text for details. The quantities measured with the VAMOS++ detectors, see schematic illustration of the detectors in Figure 3.6, include the positions ($X_{1,2}^{tp,fp}$ and $Y_{1,2}^{tp,fp}$) and the time signals ($t_{1,2}^{tp,fp}$) from the first and the second multi-wire detectors at the entrance (tp) and the focal plane (fp) of the spectrometer as well as the total energy (E) and the energy losses (ΔE_{1-7}) in the segmented IC, having 7 rows. The magnetic rigidity ($B\rho$) and the distance (D) traveled by the particle between the entrance and the focal plane multi-wire detectors are reconstructed based on the positions ($X_{tp,fp}$ and $Y_{tp,fp}$) and angles ($\theta_{tp,fp}$ and $\phi_{tp,fp}$) at the target and the focal plane obtained from $X_{1,2}^{tp,fp}$ and $Y_{1,2}^{tp,fp}$. The time of flight (TOF) is provided from the difference of the measured $t_{1,2}^{tp}$ and $t_{1,2}^{fp}$. The combination of TOF and D allows to extract the velocity (υ) of the particle.

5.2.1 Presorting and Calibration

5.2.1.1 Entrance Dual Position Sensitive Multi-Wire Proportional Counters

The particle passing through the DPS-MWPCs detector volume ionizes its gas medium creating an avalanche of the secondary electron-ion pairs. For each of the two MWPC detectors, the charges of the created pairs are measured with the wires mounted in three planes: one of them for timing and two of them to determine positions in X and Y. The timing signals allow to have the TOF measurements, see Section 5.2.1.4. The position of each particle is obtained from a distribution of the charges, firing at least three wires, relative to each other requiring a careful calibration to have an equal response of all the wires for a signal with the same amplitude.

The chips, pre-amplifier electronic circuits, integrating the charges from the position wires, see Section 3.4.4, induce signals (pedestals) without the presence of any external source. In order to prevent accumulating useless data, these pedestals were removed before the experiment by setting the thresholds correspondingly. The primary calibration of the detectors include the alignment of the signals with various attenuation factors sent from a pulse generator module to each wire channel. The peak of each signal of each channel n was fit by means of a Gaussian function to extract the centroid which is equal to the amplitude ($\mathrm{Q_n}$) of the signal. Using $\mathrm{Q_n}$, the signals of all the wires were aligned with respect to the ones of the arbitrary chosen reference wire ($\mathrm{n_{Ref}}$) according to the following equation

$$\mathrm{Q_n^{align}} = \mathrm{A_n} + \mathrm{B_n}\cdot\mathrm{Q_n} + \mathrm{C_n}\cdot\mathrm{Q_n^2} \tag{5.6}$$

where $\mathrm{A_n}, \mathrm{B_n}$ and $\mathrm{C_n}$ are the alignment parameters, and $\mathrm{Q_n^{align}}$ is the amplitude of the signal of channel n after the alignment. The signals of each of the wire channels of the detectors before and after the alignment are shown in Figure 5.2.

Due to non-uniform gains of the wire channels, leading to a discontinuity of the charge distribution, a secondary calibration procedure consisting in matching the gains is required. The procedure involves the elastic scattering reaction of ^{238}U + ^{197}Au at 7.193 MeV/A. The elastic recoils of this reaction a have high enough energy ($\mathrm{E_{^{238}U}}$ = 843.71 MeV and $\mathrm{E_{^{197}Au}}$ = 990.31 MeV at θ_{lab} = 40°) to be measured with the IC detector at the focal plane of VAMOS++ as shown in Figure 5.3 (left). In particular, it makes use of the maximum charge ($\mathrm{Q_{Max}}$), which is proportional to the energy loss, among the charges induced by each elastically scattered recoil in the wires, and calculates a scaling factor ($\mathrm{S_n}$) from the ratio between the mean value of all the $\mathrm{Q_{Max}}$ of an arbitrarily reference wire $\mathrm{n_{Ref}}$ and of the wire n as follows

$$\mathrm{S_n} = \frac{\overline{\mathrm{Q}}_{\mathrm{Max}}(\mathrm{n_{Ref}})}{\overline{\mathrm{Q}}_{\mathrm{Max}}(\mathrm{n})}, \tag{5.7}$$

Thus, the gain of the wire channels are matched

$$\mathrm{Q_n^{matched}} = \mathrm{S_n}\cdot\mathrm{Q_n^{align}}. \tag{5.8}$$

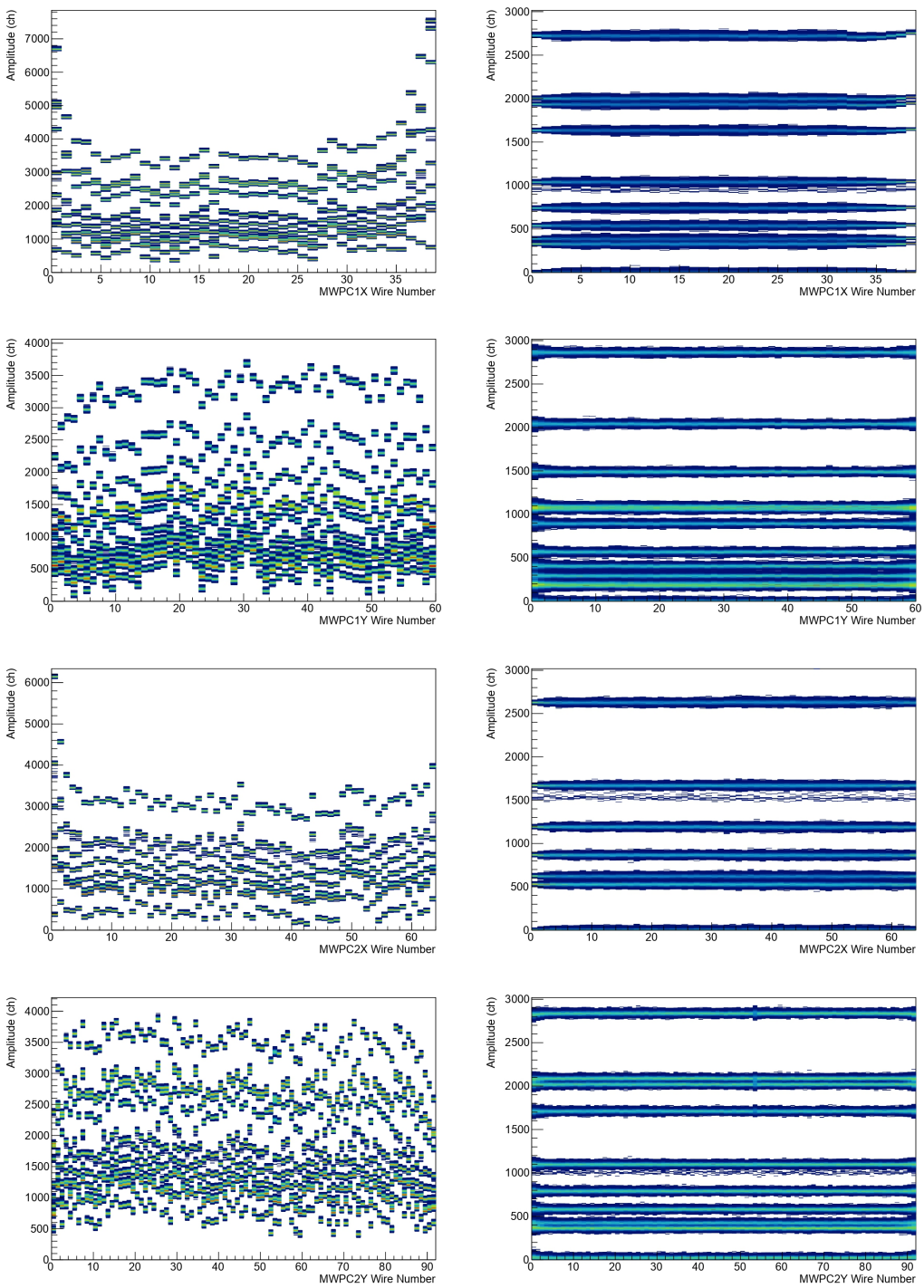

Figure 5.2: Spectra of the signals from a pulse generator module sent to the X and Y multi-wire planes of the first and the second MWPC detectors before (left) and after (right) the alignment.

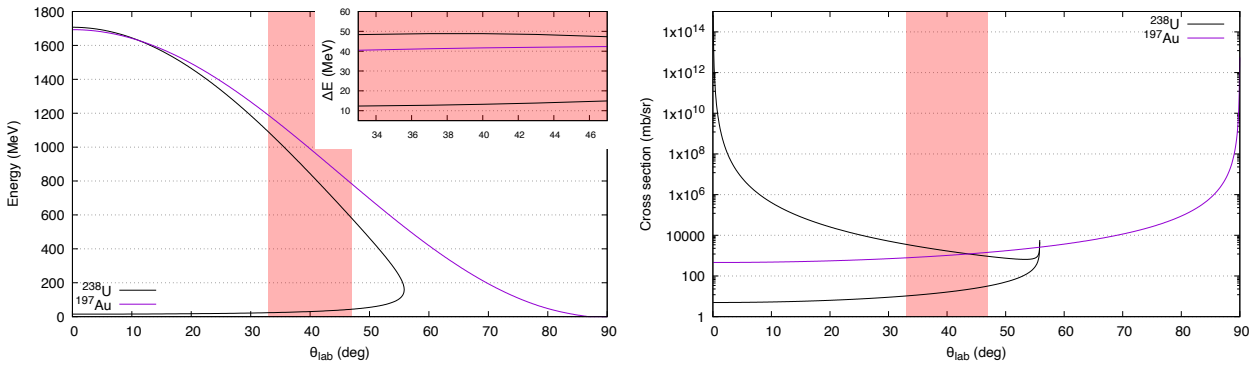

Figure 5.3: Calculated, using the LISE++ program [TB], energies (left) and cross sections (right) of the elastic scattering reaction of ^{238}U + ^{197}Au as a function of scattering angles. The calculated energy losses (ΔE) of the indicated recoils in the DPS-MWPC detector are shown in the inset. Red shaded areas represent the region covered by the VAMOS++ spectrometer placed at 40°.

where $Q_n^{matched}$ is the gain matched charges induced in wire n. The maximum charges Q_{Max} induced by the elastically scattered recoils of ^{238}U + ^{197}Au on all of the wires of the detectors before and after the gain matching are shown in Figure 5.4. It is worth to note that the maximum charge Q_{Max} distribution, shown in Figures 5.4 (b) and (f), illustrates a general trend similar to one of the calculated energy losses shown in the inset of Figure 5.3 (left). The intensity of Q_{Max} reflects the cross sections for the recoils, with a peak at more forwards angles, which also look similar to the calculated ones shown in Figure 5.3 (right). One can also note that only a portion of the low energy ^{238}U recoils, having around 30 MeV of kinetic energy at 40° according to LISE++ [TB], reach the second MWPC detector as they lose around half of their energy in the mylar foil and the gas medium of the detector, i.e. measured counts/binning for low energy ^{238}U recoils are more and less than 10^2 in the X plane of the first and the second MWPC at the entrance, respectively.

After the calibration of the response of all the wires in terms of the alignment and the gain matching, the detectors are now ready for the determination of the positions of the products of ^{238}U + ^{238}U reaction. Figure 5.5 shows an example of the charge distribution, induced by a single event, measured with the wires in the X plane of the MWPC1 detector. The measured distribution is fitted with various functions, namely Gaussian, Lorentzian and Hyperbolic secant squared (SECHS) [LP95]. The centroid values returned by the various fitting functions are equal to the position of the event. The positions (X_1^{tp}, Y_1^{tp}) and (X_2^{tp}, Y_2^{tp}) for all the events in the X and Y plane of the first and the second MWPC detectors were determined and transformed into the spectrometer reference frame by subtracting the respective offsets. As there was no change inside the detector, the offsets (reference positions) in X and Y are used from the previous experiment and are given in Table 5.1. The resulting two-dimensional hit pattern of the reaction products on the two MWPC detectors is shown in Figure 5.6. The performance of the used functions were

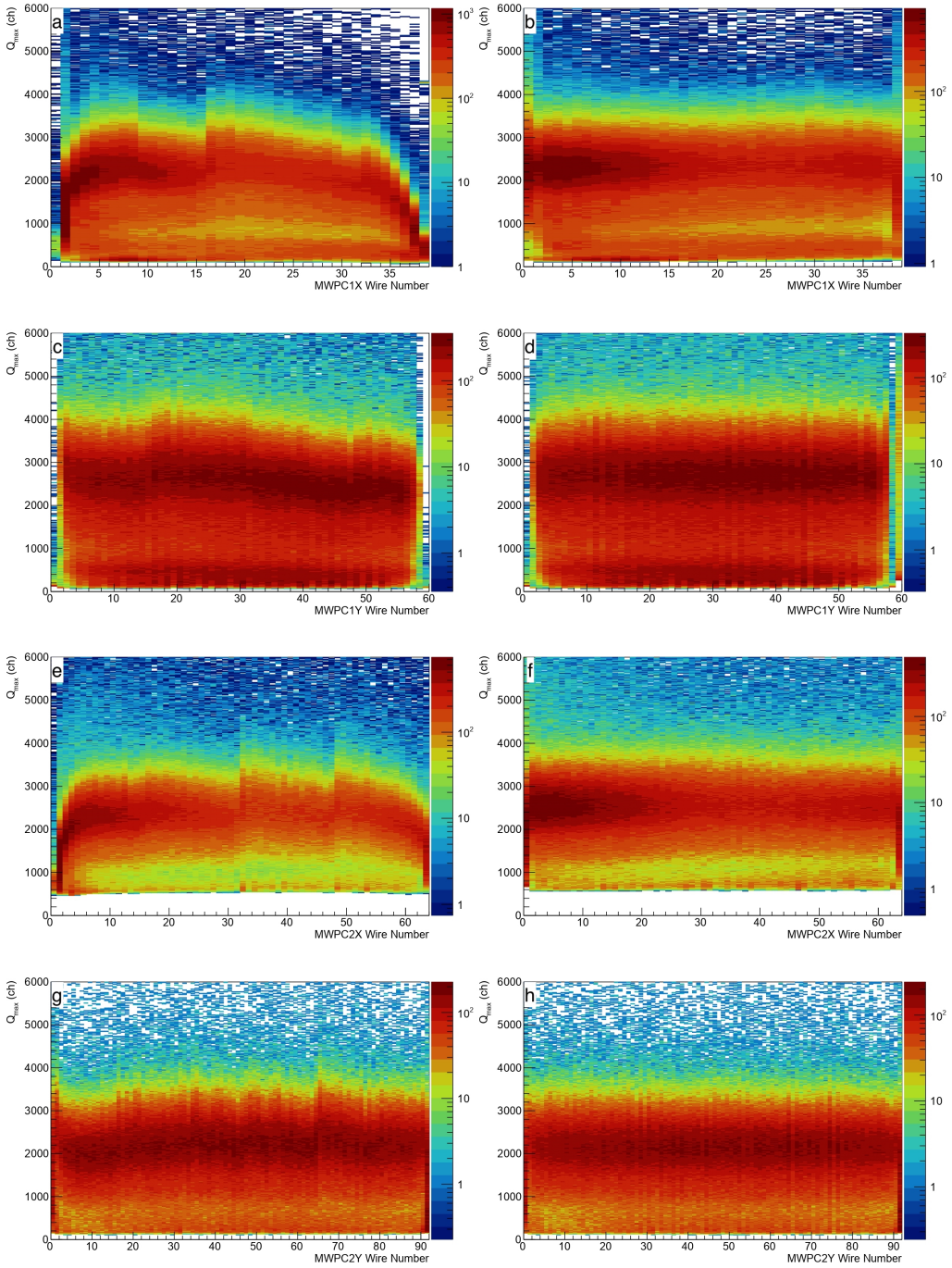

Figure 5.4: Spectra of the maximum charges Q_{Max} induced by the elastically scattered recoils of ^{238}U + ^{197}Au on all of the wires of the X and Y planes of the first and the second MWPC detectors before (a,c,e,g) and after (b,d,f,h) the gain matching. The wire numbers in X planes are proportional to the scattering angles (θ_{lab}) of the recoils.

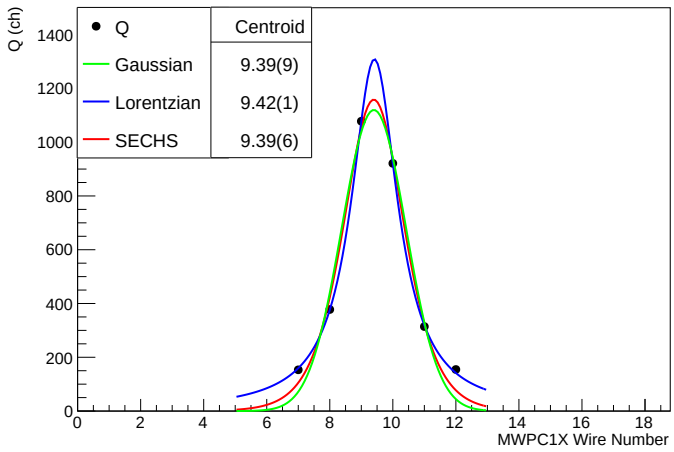

Figure 5.5: The black dots represent the charge distribution, induced by a single event, measured with the wires of the X plane of the MWPC1 detector. The lines in green, blue and red are fittings with various functions used to extract the position of the event, given as a centroid of the fit (see text for details).

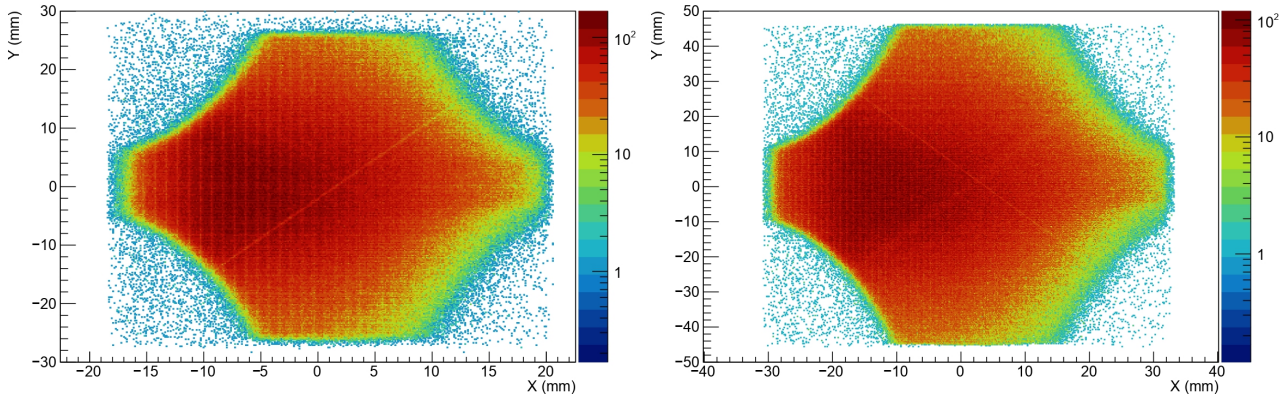

Figure 5.6: Spectra of the two-dimensional hit pattern of the first (left) and the second (right) MWPC detectors. Only the events reaching the focal plane of the spectrometer are shown, hence the spectra with a shape of the quadrupole magnets mounted after the entrance DPS-MWPC detectors, see Section 3.4.1.2. The diagonal line in the spectra of each of the MWPC detectors represents the shadow of the 100 μm reference wires.

evaluated by measuring the resolution of the peak resulting from the shadow of the diagonally placed 100 μm reference wire. The obtained position resolutions for the Gaussian, Lorentzian and SECHS functions for the first MWPC detector are 311(6), 302(9) and 300(12) μm (FWHM). The SECHS function has a slightly better performance and therefore from now on it is used to extract the positions in the entrance DPS-MWPC and also in the focal plane MWPPC detectors. As an

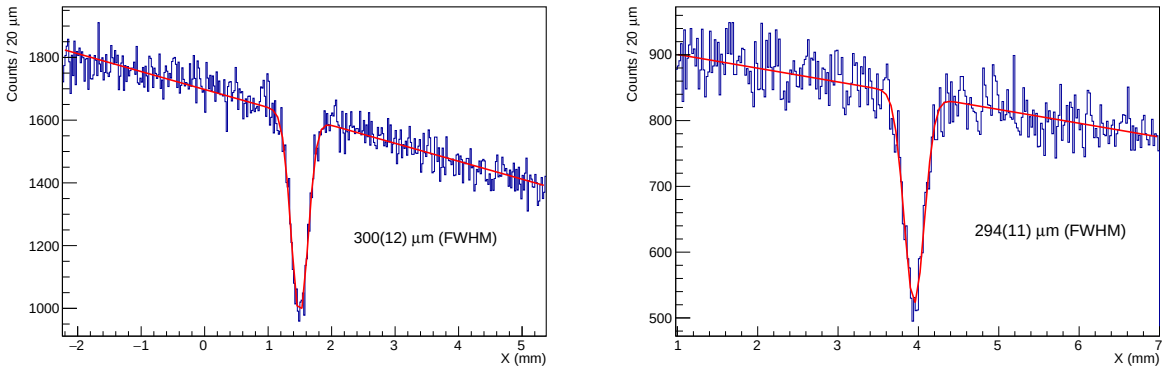

Figure 5.7: Projection, perpendicular to the reference wire, of the two-dimensional hit pattern of the first (left) and the second (right) MWPC detectors shown in Figure 5.6, respectively. The obtained position resolutions are indicated.

Table 5.1: Reference positions of the two MWPC detectors, placed at the entrance of VAMOS++, in the spectrometer reference frame.

Detector	X (mm)	Y (mm)	Z (mm)
MWPC1	18.4	29.35	139.7(1)
MWPC2	30.8	45.8	244.7(1)

example, the measured position resolutions for the SECHS function for the first and the second MWPC detectors are shown in Figure 5.7.

Once the positions X_1^{tp}, Y_1^{tp} and X_2^{tp}, Y_2^{tp} in the two MWPC detectors are obtained, the image of the target position in terms of the interaction point on the target and the scattering angles can be reconstructed. The relations for the interaction point on the target (X_{tp}, Y_{tp}) follows as

$$X_{tp} = X_1^{tp} - Z_1 \frac{X_2^{tp} - X_1^{tp}}{Z_2 - Z_1} \qquad \text{and} \qquad Y_{tp} = Y_1^{tp} - Z_1 \frac{Y_2^{tp} - Y_1^{tp}}{Z_2 - Z_1} \tag{5.9}$$

where Z_1 and Z_2 are the distances from the target to the first and the second MWPC detectors, respectively. These distances were measured by the mechanics group of GANIL before the experiment, see Table 3.3. However, to account for any possible displacements during the experiment, e.g. the target holder or the detectors, a scan of different values for Z_1 was performed, from 130 to 150 mm with a step of 0.1 mm, by measuring the position resolution of the interaction point on the target ($\sigma_{X_{tp}}$, $\sigma_{Y_{tp}}$). Assuming that the minimum dispersion of the events on X_{tp} and Y_{tp} to be optimal, the value of Z_1 was found to be 139.7(1) mm as shown in Figure 5.8. Knowing Z_1, one can calculate the value of Z_2 as the distance between these two is 105 mm, see Section 3.4.1.1. The values of the obtained distances (reference positions) in Z are given in Table 5.1. Figure 5.9 (left) shows the reconstructed image of the interaction point on the target X_{tp} and Y_{tp}. The scattering

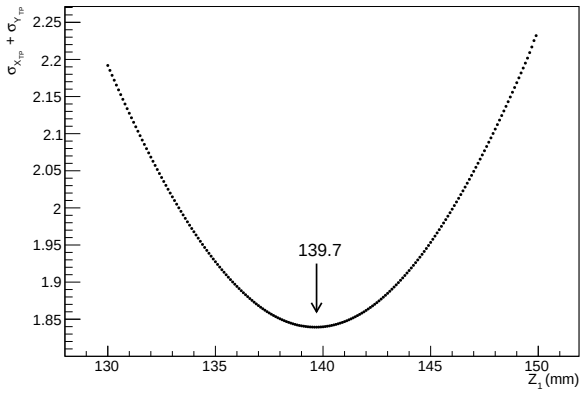

Figure 5.8: The sum of the position resolution of the interaction point on the target ($\sigma_{X_{tp}} + \sigma_{Y_{tp}}$), shown in Figure 5.9 (left), for different values of Z_1 between the first MWPC at the entrance of VAMOS++ and the target position. The minimum deviation reflects the optimal value for Z_1.

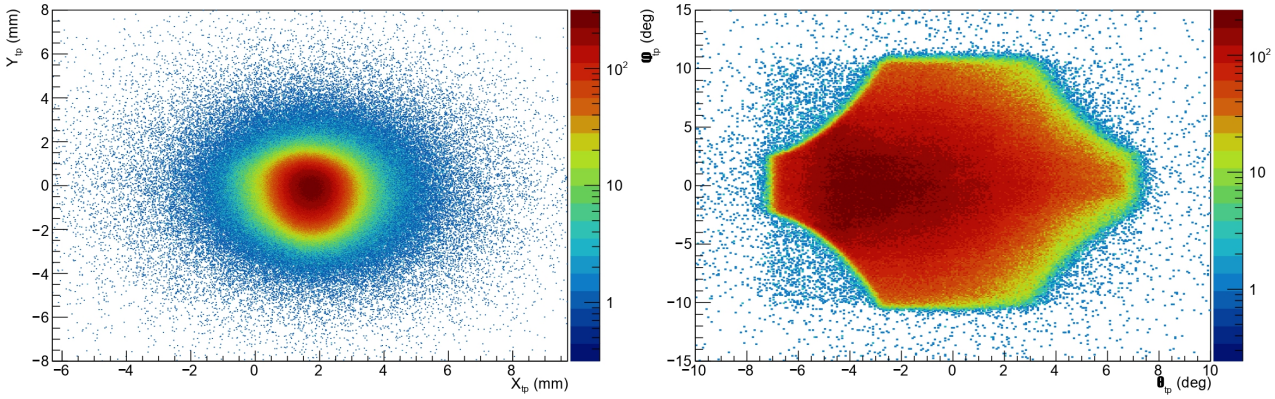

Figure 5.9: Spectra of the image at the target position showing the scattering angles of the reaction products (right) and the interaction point on the target (left). Only the events reaching the focal plane of VAMOS++ are shown and, hence, such a shape of the image of the scattering angles of the products originating due to the quadrupole magnets focusing them in y- and x-directions, see Section 3.4.1.2.

angles of the products (θ_{tp}, ϕ_{tp}) are reconstructed using the following relations

$$\tan(\theta_{tp}) = \frac{X_2^{tp} - X_1^{tp}}{Z_2 - Z_1} \qquad \text{and} \qquad \tan(\phi_{tp}) = \frac{Y_2^{tp} - Y_1^{tp}}{Z_2 - Z_1}. \tag{5.10}$$

Figure 5.9 (right) shows the reconstructed image of θ_{tp} and ϕ_{tp}. In the following sections, this information will be used for the determination of the traveled distances of the reaction products in VAMOS++.

5.2.1.2 Focal Plane Multiwire Parallel Plate Avalanche Counters

The pair of focal plane MWPPAC detectors operate using the same principle as the DPS-MWPC detectors at the entrance of VAMOS++ described in the previous section, and its calibration procedure, likewise the same, consists of the alignment of the wire channels response and the gain matching shown in Figures 5.10 and 5.11, respectively. In contrast to the DPS-MWPC detectors, due to the insufficient amount of ^{238}U + ^{197}Au reaction data to cover all of the wires of the MWPPAC detectors, the scaling factors for the gain matching were calculated based on the actual experimental data of the ^{238}U + ^{238}U reaction, see Figure 2.8 for the energies of the elastically scattered recoils in the region covered by the VAMOS++ spectrometer.

The positions of the hit pattern (X_1^{fp}, Y_1^{fp}) and (X_2^{fp}, Y_2^{fp}) on the two MWPPAC detectors, obtained from the charge distribution of the products (see previous section), are shown in the two-dimensional spectra in Figure 5.12. The position resolution for the second MWPPAC detector measured from the profile of the diagonally placed reference wire is shown in Figure 5.13.

From the determined hit patterns one can reconstruct the image at the plane defined as "focal plane", located 7.6 m from the target in z-axis along the central trajectory of the spectrometer. The focal plane image, providing positions (X_{fp}, Y_{fp}) and angles (θ_{fp}, ϕ_{fp}) as shown in Figure 5.14, is reconstructed, in the same way as the target position image. It is transformed into the VAMOS++ frame, in which the trajectories were simulated (see the following section), using the reference positions in X, Y and Z. A precise determination of the reference positions is crucial to properly set the newly installed MWPPAC detectors in the VAMOS++ frame since the focal plane image is necessary to reconstruct the magnetic rigidity (Bρ) and the traveled distance (D) of the reaction products, and, in turn, to reconstruct their mass over charge state ratio (A/q), see the beginning of Section 5.2.

The determination of the reference positions was performed making use of the reconstructed A/q of the reaction products which is in first approximation proportional to their Bρ and D, combined with the time of flight (see Section 5.2.1.4), as given by Equation 5.2. This information together with the assumption that in the ^{238}U + ^{238}U reaction the mainly populated products are elastically scattered ^{238}U recoils, one can determine the charge states (238/(A/q)) of the reaction products. The condition that the values of the charge states 238/(A/q) has to be centered at integer values permits the determination of the reference positions. Starting from the Z values provided by the mechanics group of GANIL before the experiment (see Table 3.3) and the value of X set in the middle of the axis, the reference positions for the first and the second MWPPAC detectors together with the offset in time (see Section 5.2.1.4) were scanned iteratively by minimizing the difference (Δq) between the charge states ($238/(A/q)$) and their associated integer values ($(238/(A/q))_{int}$)

$$\Delta q = (238/(A/q)) - (238/(A/q))_{int}. \tag{5.11}$$

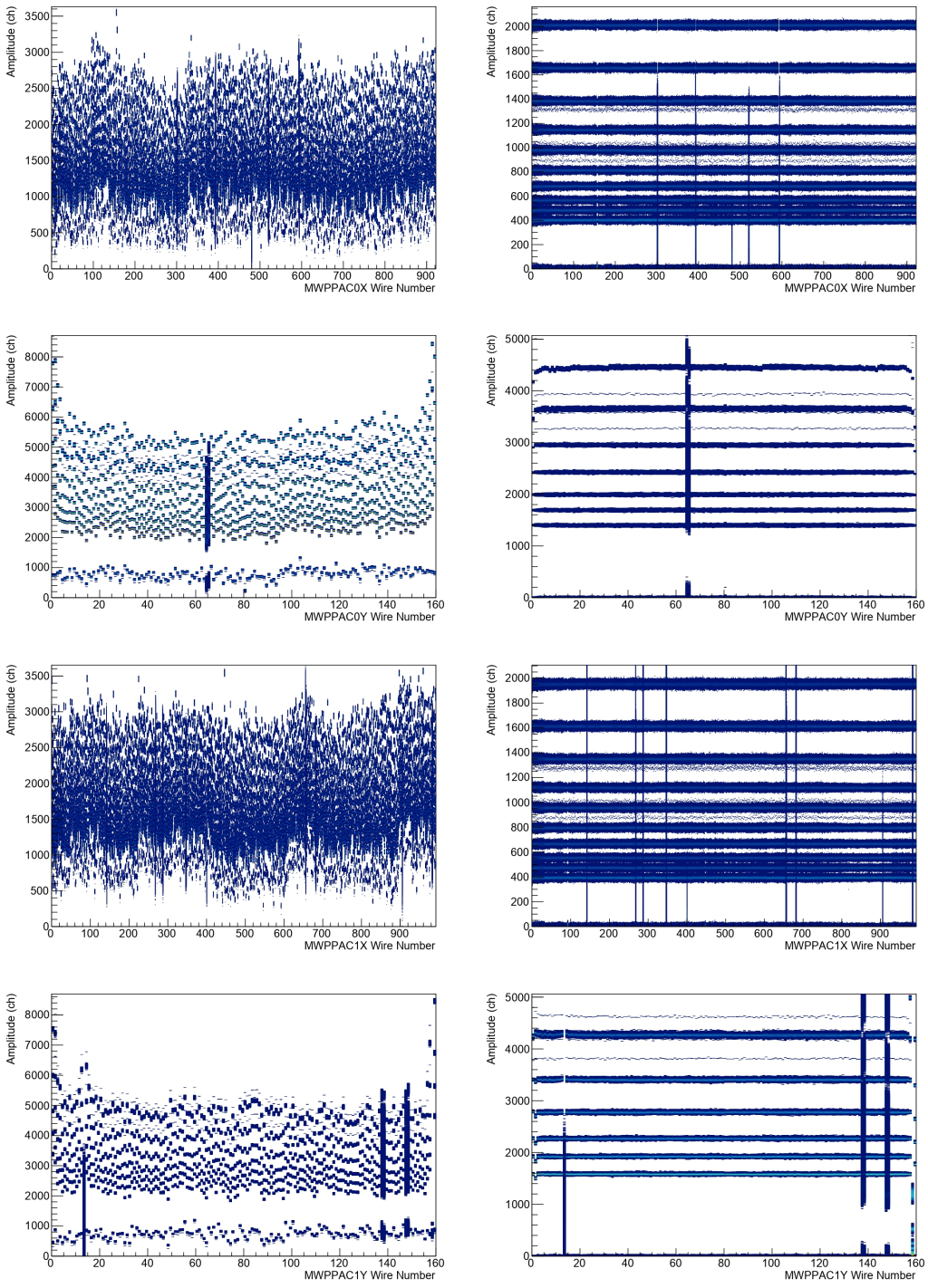

Figure 5.10: Spectra of the signals from a pulse generator module sent to the X and Y multi-wire planes of the first and the second MWPPAC detectors before (left) and after (right) the alignment. The first and the second MWPPAC detectors are denoted as MWPPAC0 and MWPPAC1, respectively. The abnormal signals in each plane are due to broken wires.

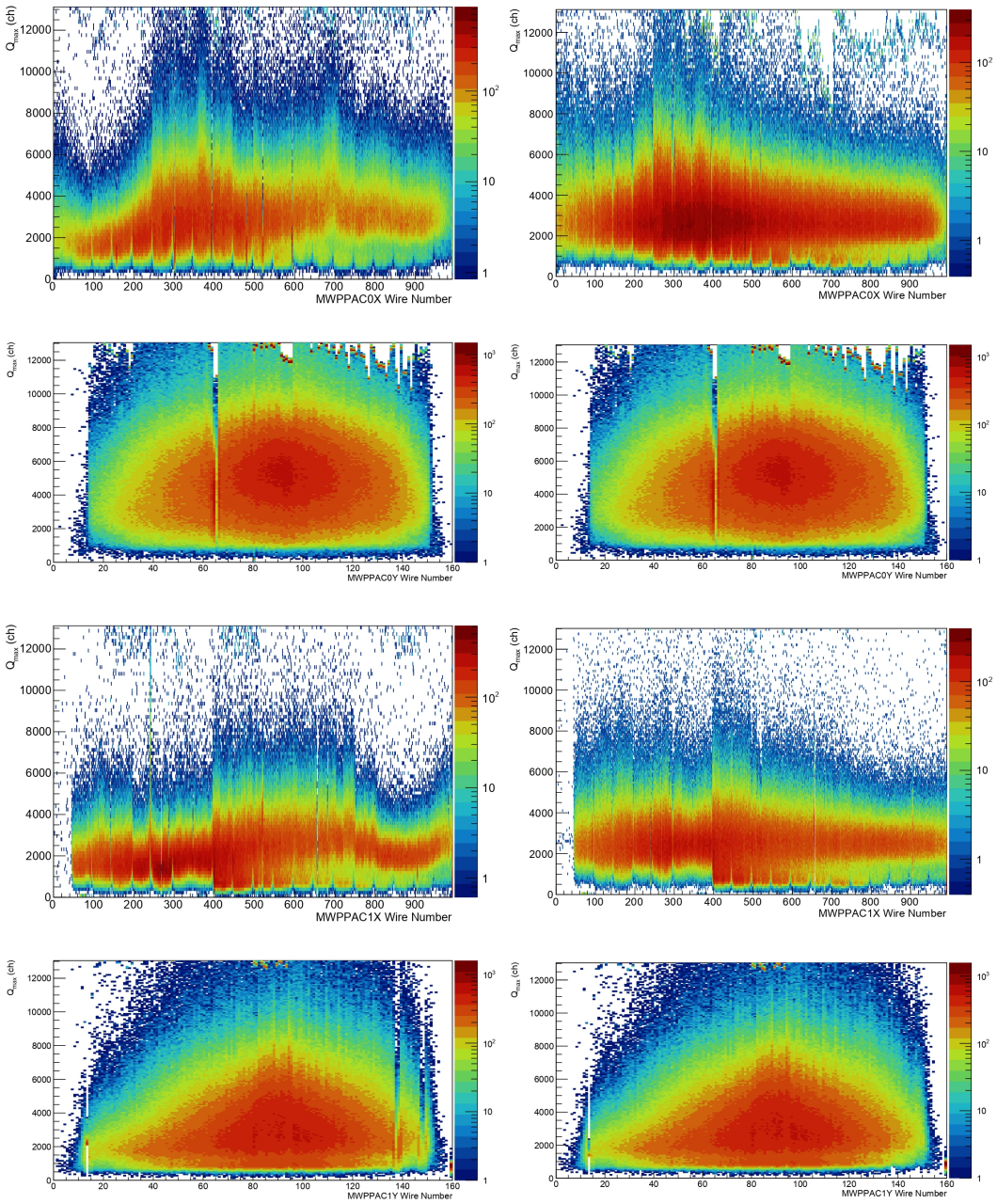

Figure 5.11: Spectra of the maximum charges Q_{Max} induced by the reaction products of ^{238}U + ^{238}U on all of the wires of X and Y planes of the first and the second MWPPAC detectors before (left) and after (right) the gain matching. The first and the second MWPPAC are denoted as MWPPAC0 and MWPPAC1, respectively. The abnormal signals in each plane are due to the broken wires.

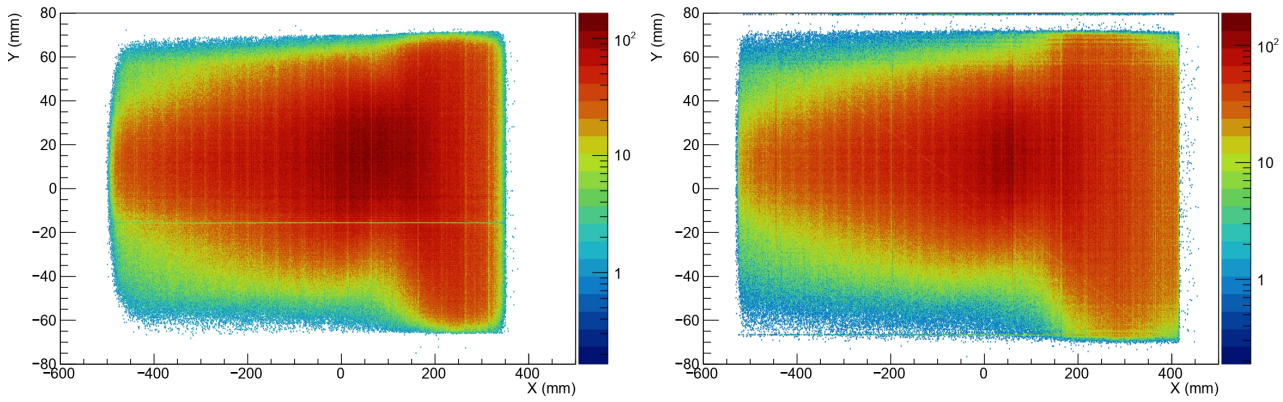

Figure 5.12: Spectra of the two-dimensional hit pattern of the first (left) and the second (right) MWPPAC detectors.

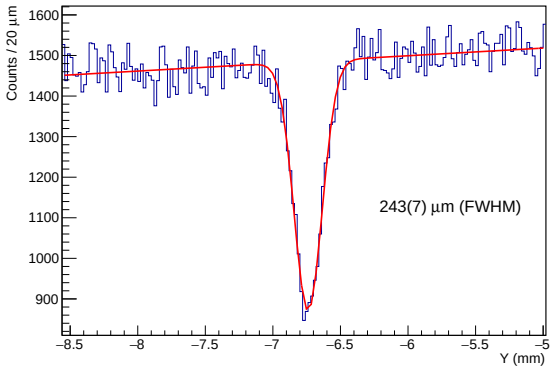

Figure 5.13: Projection, perpendicular to the reference wire, of the two-dimensional hit pattern of the second MWPPAC detector shown in Figure 5.12 (right). The obtained position resolution is indicated.

Figure 5.15 shows the charge states 238/(A/q) of the reaction products before and after performing the minimization procedure. One can see that the charge states 238/(A/q) are now well centered at integer values and that the standard deviation of the Δq is improved. The resulting reference positions of the MWPPAC detectors in the VAMOS++ reference frame are listed in Table 5.2. Being less significant, the values of Y were kept centered in the middle of the axis. The trajectory reconstruction technique will be described in the following section.

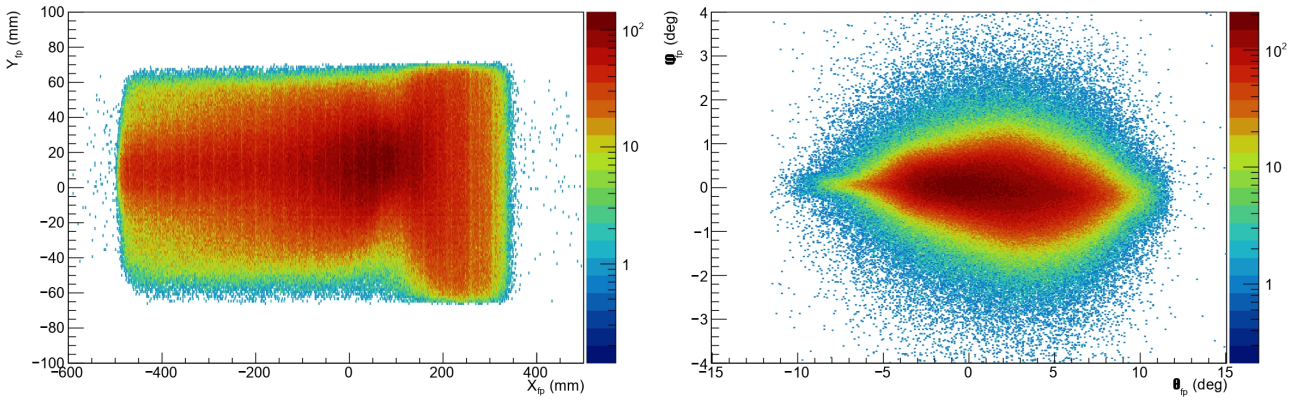

Figure 5.14: Spectra of the image at the focal plane showing the positions X_{fp} versus Y_{fp} (left) and the angles θ_{fp} versus ϕ_{fp} (right) of the reaction products. This information is to be used by the trajectory reconstruction technique to obtain the magnetic rigidity and the flight path of the reaction products, see Section 5.2.1.3.

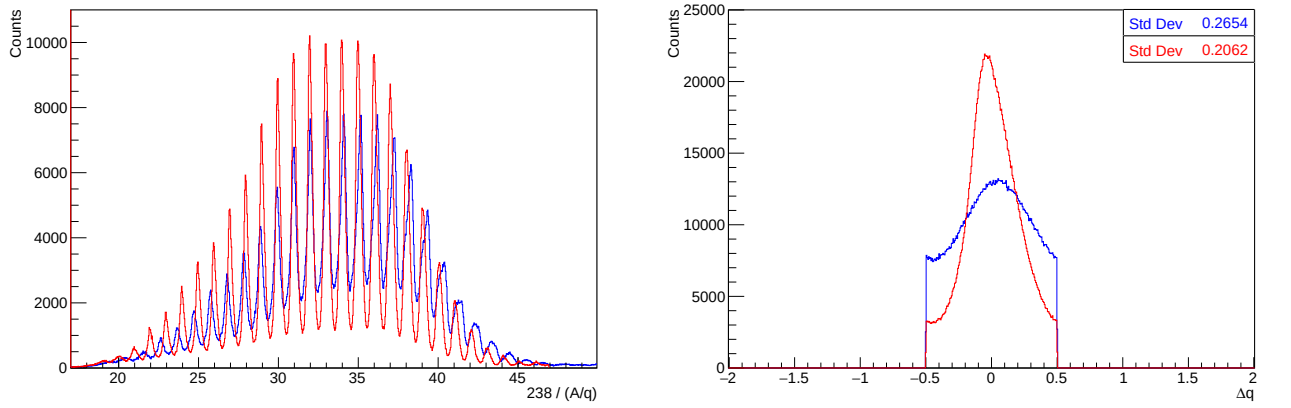

Figure 5.15: Left: The charge states (238/(A/q)) of the products, assuming that the most populated products are elastically scattered ^{238}U recoils, before (blue) and after (red) the minimization procedure of the reference positions in X and Z for the first and the second MWPPAC detectors as well as the offset in time (see Section 5.2.1.4). One can see the improvement from the charge states well centered at integer values (left), and from the standard deviation of the difference Δq between the charge states and their associated integer values (right), as given in Equation 5.11.

Table 5.2: Reference positions of the two MWPPAC detectors, placed at the focal plane of VAMOS++, in the spectrometer reference frame. The positions in X and Z are obtained by the minimization procedure (see text for details) and are crucial to match the coordinates of the focal plane image, provided by the MWPPAC detectors, with the ones having trajectories calculated by the trajectory reconstruction technique (see Section 5.2.1.3). The Y values are less significant and were centered in the middle of the axis.

Detector	X (mm)	Y (mm)	Z (mm)
MWPPAC1	460(2)	80.0	7662(3)
MWPPAC2	461(1)	80.0	8242(2)

5.2.1.3 Trajectory reconstruction

Due to the large size of the magnetic elements of VAMOS++, the ion optics becomes highly non-linear and therefore induces significant image aberrations in the focal plane, preventing, in this way, a determination of the particle momentum from the direct position measurement alone. To account for these aberrations, the identification algorithm of VAMOS++ employs a method which reconstructs the trajectory of the particle in the magnetic fields by making use of a numerical procedure combined with a relationship between the measured positions and angles at the focal plane and the reconstructed quantities such as the magnetic rigidity (Bρ) and the flight path of the particle (Path) between the target and the focal plane images [PRN+08, PCJ+08]. This method also can reconstruct the scattering angles of the particles which are presently measured directly with the DPS-MWPCs, see Section 5.2.1.1.

The trajectory reconstruction method is operated in two independent steps including the simulation of the particle trajectories and the back-tracing reconstruction. The first step involves the ion optical ray-tracing code Zgoubi [Mé99] which simulates the trajectories of the particles through the magnetic field of the ion optical elements using the field maps. The code traces a set of 20000 trajectories covering the full acceptance of the spectrometer and stores their initial (δ, x_{i}, θ_{i}, y_{i}, ϕ_{i}) and final parameters ($\mathrm{x_{fp}}$, θ_{fp}, $\mathrm{y_{fp}}$, ϕ_{fp}, l). For a given trajectory, the parameters x and y correspond to two transverse distances from the reference trajectory, and the parameters θ and ϕ refer to the inclination angle in horizontal and vertical planes. The parameter l is the difference in flight path length between the given and the reference path. The parameter δ = (Bρ - Bρ_0)/Bρ_0 defines the fractional magnetic rigidity deviation from the reference magnetic rigidity. The second step consists in a relation between the four final parameters ($\mathrm{x_{fp}}$, θ_{fp}, $\mathrm{y_{fp}}$, ϕ_{fp}), provided with the

focal plane MWPPAC detectors, and the quantities to be reconstructed:

$$\begin{aligned} \delta &= F_1(\mathrm{x_{fp}}, \theta_{\mathrm{fp}}, \mathrm{y_{fp}}, \phi_{\mathrm{fp}}) \\ \theta_{\mathrm{i}} &= F_2(\mathrm{x_{fp}}, \theta_{\mathrm{fp}}, \mathrm{y_{fp}}, \phi_{\mathrm{fp}}) \\ \phi_{\mathrm{i}} &= F_3(\mathrm{x_{fp}}, \theta_{\mathrm{fp}}, \mathrm{y_{fp}}, \phi_{\mathrm{fp}}) \\ l &= F_4(\mathrm{x_{fp}}, \theta_{\mathrm{fp}}, \mathrm{y_{fp}}, \phi_{\mathrm{fp}}) \end{aligned} \tag{5.12}$$

The parameters obtained from this method were provided by the VAMOS collaboration.

The determination of the distance (D) traveled by the particle between the entrance and the focal plane detectors, measuring the time of flight (TOF), of VAMOS++ is required to calculate its velocity. The TOF and the corresponding distance D are used in the further analysis between the second MWPC detector at the entrance and the first MWPPAC detector at the focal plane. The distance (D) is determined event-by-event using the reconstructed flight path length Path as well as the angles at the target position (θ_{tp}, ϕ_{tp}) and the focal plane (θ_{fp}, ϕ_{fp}) using the following equation

$$\mathrm{D} = \mathrm{Path} - \frac{\mathrm{Z_2^{tp}}}{\cos(\theta_{\mathrm{tp}}) \cdot \cos(\phi_{\mathrm{tp}})} + \frac{\mathrm{Z_1^{fp}} - \mathrm{Z_0^{fp}}}{\cos(\theta_{\mathrm{fp}}) \cdot \cos(\phi_{\mathrm{fp}})} \tag{5.13}$$

where $\mathrm{Z_2^{tp}}$ and $\mathrm{Z_1^{fp}}$ are the distances between the target and the second MWPC detector, and between the focal plane and the first MWPPAC detector, respectively (see the values in Tables 5.1 and 5.2, respectively). $\mathrm{Z_0^{fp}}$ is the distance of 7.6 m from the target to the focal plane of the spectrometer. The TOF measurement of the reaction products will be discussed in the following section.

5.2.1.4 Time of Flight

The timing signals measured with the DPS-MWPCs at the entrance and the MWPPACs at the focal plane of the spectrometer allow to obtain the time of flight (TOF) of the reaction products. Each pair of MWPPACs has 20 sections providing independent signals each. The TOF is measured using the Time-to-Amplitude Converter (TAC) modules. The details of the TAC modules, with the information on the Start and Stop signals, used in the present experiment were presented in Section 3.4.4. In the further analysis, the TOF between the second MWPC detector at the entrance and the first MWPPAC detector at the focal plane is utilized to have as little as possible fluctuation in the velocity calculation, resulting from the energy losses in the different layers of material between the detectors. The calibration of the TAC modules consists in the obtaining of the calibration parameters with a time calibrator module, allowing to convert signals from $\mathrm{channel}$ to ns, and the determining of the offsets using the actual experimental data of the ^{238}U + ^{238}U reaction for the measurement of the TOF of the reaction products.

The time calibrator module sends signals to the TAC modules with a period of 40 ns covering the full range of the TAC. The peaks of the signals were fitted with a Gaussian distribution which returns centroid values. The values were used for the calibration into ns via $\mathrm{Time\ (ns)} = \mathrm{a} \cdot (\mathrm{channel})$

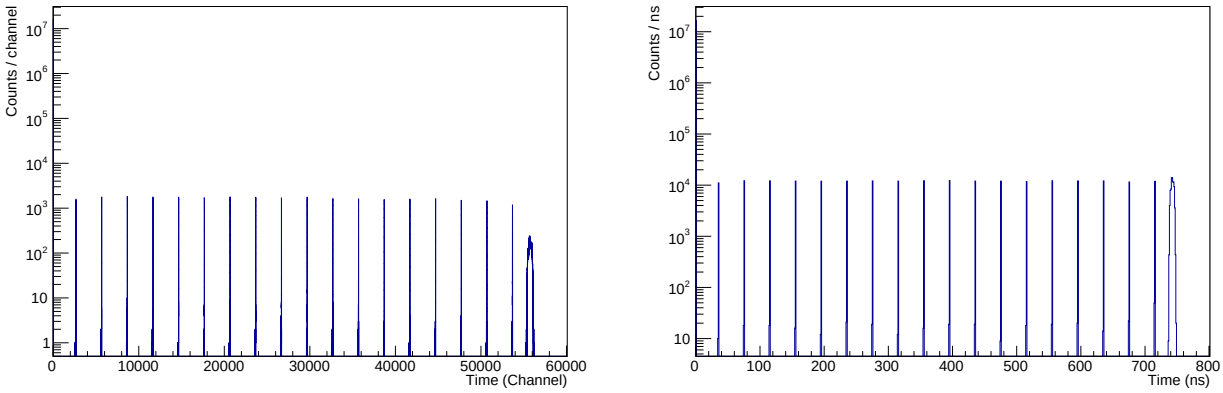

Figure 5.16: Example of spectra of the signals sent from a time calibrator to the TAC modules, used to measure the TOF of the reaction products, before (left) and after (right) the calibration. The period of the signals is 40 ns.

Table 5.3: The calibration parameters for the TAC modules, see details of the modules in Table 3.9. For TAC #6 and #7 the parameters are given before and after the change of the input signals. TAC #5 was used not in the scope of the present work and, therefore, is not given here. TAC#3 and #7 was used for extracting the TOF of the reaction products.

TAC	a	$\text{offset}_{\text{common}}$ (ns)
1	$1.33201(6)\times10^{-2}$	145.13(2)
2	$1.32754(7)\times10^{-2}$	143.33(3)
3	$1.28580(9)\times10^{-2}$	206.65(2)
4	$1.29036(16)\times10^{-2}$	314.50(8)
6	$1.33300(6)\times10^{-2}$ | $2.6657(8)\times10^{-2}$	0 | 38.12(5)
7	$0.640922(58)\times10^{-2}$ | $2.58152(6)\times10^{-2}$	0 | 206.65(4)
8	$0.275565(38)\times10^{-2}$	0

where a is the calibration parameter. Figure 5.16 shows, as an example, the spectra of one of the TACs before and after the calibration with the time calibrator module. The obtained calibration parameters for the above mentioned TAC module, and also for the ones listed in Table 3.9, are given in Table 5.3.

The offset in time was determined as shown earlier in Figure 5.15, together with the focal plane reference positions, benefiting from the proportionality of the TOF, together with the magnetic rigidity and the traveled distance of the reaction products, to the A/q given by Equation 5.2 and using the minimization of Δq described in Section 5.2.1.2. In addition, the different timing sections of the MWPPAC detector have to be aligned using additional offsets to prevent system-

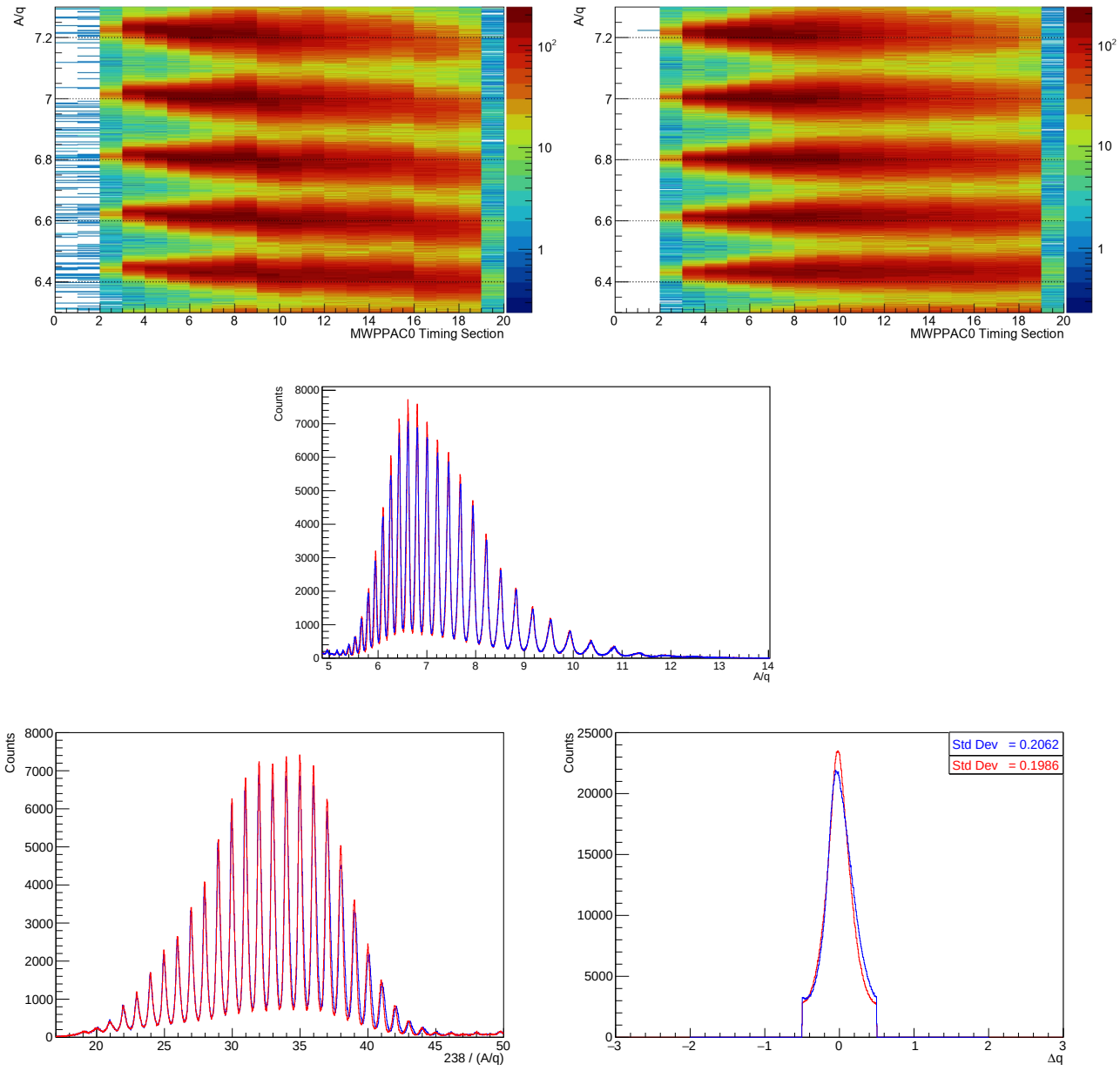

Figure 5.17: A closer view at the mass number over charge state (A/q) of the uranium-like reaction products as a function of different timing sections of the first MWPPAC detector, denoted as MWPPAC0, at the focal plane before (top left) and after (top right) alignment. The A/q spectrum (middle) and the charge states (238/(A/q)) of the uranium-like products (bottom left) with (red) and without (blue) alignment. The effect of the alignment is illustrated by the improved standard deviation of the difference Δq (bottom right).

atic errors related to the effect of the possible difference in cabling length or split of the charges created in the gas medium by the passing ion between neighboring sections leading to a lower amplitude signal. These offsets are also determined by the Δq minimization for a given timing section. Overall, the TOF of the reaction products are calculated by adding the offsets (since in the present experiment the Start and the Stop signals were provided by the second MWPC detector at the entrance and the first MWPPAC detector at the focal plane, respectively) to the time calibrated with the time calibrator as follows

$$\mathrm{TOF} = \mathrm{Time\ (ns)} + \mathrm{offset_{common}} + \mathrm{offset_n} \tag{5.14}$$

where $\mathrm{offset_{common}}$ is the offset common to all the sections of the MWPPAC, see the values in Table 5.3, and $\mathrm{offset_n}$ are the offsets for each of the n sections for the alignment. Figure 5.17 (top) shows the A/q spectrum of the uranium-like reaction products as a function of different timing sections of the first MWPPAC detector at the focal plane before and after alignment. The improvement of the alignment can be observed in Figures 5.17 (middle) and (bottom left) which show the A/q spectra and the charge states (238/(A/q)) assuming that the mainly populated products are elastically scattered ^{238}U recoils, respectively. Moreover, the improvement is also illustrated by the lower standard deviation for the Δq distribution, see Figure 5.17 (bottom right). To align the different timing sections, values of $\mathrm{offset_n}$ from -4 ns to + 3 ns were used.

Once the TOF information is extracted, it is possible to determine the velocity (v) of the products. As an example, Figure 5.18 shows the velocity v as a function of scattering angle for the ^{238}U + ^{238}U reaction products at 6.765 MeV/A without the aluminum degrader. The distribution is compared with the values calculated for the elastically scattered ^{238}U recoils using LISE++ [TB]. A slight discrepancy is due to the energy and angular straggling of the recoils in the entrance

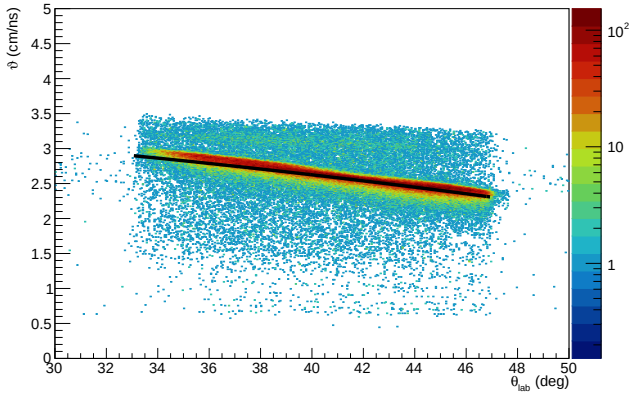

Figure 5.18: Example of the measured velocity (v) as a function of the scattering angle in the laboratory frame for the products of the ^{238}U + ^{238}U reaction at 6.765 MeV/A without the aluminum degrader. The black line represents the velocity for the elastically scattered ^{238}U recoils calculated with LISE++ [TB].

DPS-MWPC detector materials, e.g. for 33° and 47° the energy straggling (σ) of 0.000452 and 0.000388 MeV/A , corresponding to the velocities of 0.0295 cm/ns and 0.0274 cm/ns, respectively, is calculated for the upstream mylar window of the detector.

5.2.1.5 Ionization chamber

The particle crossing the volume of the IC detector deposits its energy by ionizing the atoms of the gas and generating electron-ion pairs, see the description of the detector in Section 3.4.1.4. The signals produced by the pairs are measured with the cathode and the anode which is divided into 7 segments in depth. The amplitude of the measured signal is proportional to the energy loss ($\Delta E_{1,2,3,4,5,6,7}$) of the particle in the given segment. The sum of the measured $\Delta E_{1,2,3,4,5,6,7}$ provides the total energy (E_{IC}) deposited in the IC detector by the particle. It is crucial to determine E_{IC} as it is required, combined with the energy lost before the IC detector (E_{nm}), to reconstruct the mass A of the reaction products, see the beginning of Section 5.2. Therefore, a proper energy calibration of the different segments of the IC is necessary.

Typically, the calibration of the IC detector for the measurement of such heavy products like uranium is performed using the elastically scattered products of the ^{238}U + ^{238}Au reaction. However, in addition to the previously mentioned insufficient amount of data, the gain of the preamplifiers were improperly set leading to the absence of the signals, which were probably in saturation, for several IC segments. The gains were reduced later for the ^{238}U + ^{238}U reaction. Therefore, the calibration of the IC detector is performed using the ^{238}U + ^{238}U reaction data directly.

The total kinetic energy (E) of the particle can be deduced from the velocity and the mass which in turn can be deduced from the combination of the reconstructed mass over charge state ratio (A/q) and assigning the charge state (q) to the particle obtained using the spectrometer, see Equations 5.3, 5.4 and 5.5. For the elastically scattered ^{238}U recoils which served as a reference, knowing the A/q, one can assign the correct value of the charge state q, e.g. if the A/q of ^{238}U is 5.8, then q is 41. Knowing q and A/q gives the mass which combined with the velocity provided by the spectrometer, allows to determine the total kinetic energy (E_{rec}). This information allows to perform the calibration of the IC detector using the actual experimental data of ^{238}U + ^{238}U reaction with the following equation

$$E = E_{rec} = E_{nm} + E_{IC} = b + \sum_{n=1}^{7} a_n \cdot IC_n \tag{5.15}$$

where a_n and b are the calibration parameters, IC_n is the energy lost in segment n of the IC detector. To obtain these parameters an iterative process is carried out minimizing the difference between the deduced total energy E_{rec} and the E_{IC} measured with the IC detector accounting for the not measured energy E_{nm}.

As a first step, the minimization of the difference of the E_{rec} and the E_{IC} was performed based

Table 5.4: The calibration parameters for each of the IC detector segments obtained based on the fission fragment region, see Table 3.6 for dimensions of the segments.

Segment	a	b
IC_1	$(4.39 \pm 2.10) \times 10^{-3}$	
IC_2	$(5.32 \pm 2.34) \times 10^{-3}$	
IC_3	$(5.71 \pm 1.06) \times 10^{-3}$	
IC_4	$(6.40 \pm 0.70) \times 10^{-3}$	3.43874 ± 7.713
IC_5	$(9.14 \pm 0.79) \times 10^{-3}$	
IC_6	$(1.29 \pm 11.01) \times 10^{-4}$	
IC_7	$(2.48 \pm 19.80) \times 10^{-5}$	

on the region of the fission fragments populated in the ^{238}U + ^{238}U reaction. The region of the fission fragments, having the masses lighter than the uranium ones, offers distinctively separated various charge states and A/q ratios, as was previously observed using VAMOS++ in the ^{238}U + ^{9}Be reaction at 6.2 MeV/A [KLR+17] and in the ^{238}U + ^{12}C reaction at 6.1 MeV/A [RCnF+18], providing a good starting point for the calibration.

The difference of the E_{rec} and the E_{IC} energies of the light fission fragments populated in the present measurement were minimized iteratively. The resulting distribution before and after minimization is shown in Figure 5.19 (bottom right). Figures 5.19 (top left) and (top left) show the q versus A/q spectra of the light fission fragments region before and after minimization, and the projection on the corresponding charge states are shown Figure 5.19 (bottom right). The improvement is appreciable with the charge states centered at integer values. The charge state resolution obtained for q = 26 is 1.87(3)% (FWHM). The obtained calibration parameters are given in Table 5.4.

The parameters determined based on the minimization of the fission fragments energies were applied for the calibration of the IC detector. However, it turns out that these parameters are insufficient for the calibration of the energies of the uranium-like products of interest, as reflected in incorrectly obtained charge state values of the uranium-like products in Figure 5.20 (top left). The correct charge state values, as mentioned earlier, can be calculated thanks to the knowledge of the A/q of the ^{238}U products, which are illustrated by the black dots.

With the energy left after the aluminum degrader , the uranium-like products lose around 30% to 70% of energy, according to LISE++ [TB], depending on the scattering angle, in the different layers of the matter of VAMOS++ prior to the IC detector. Therefore, they approach the Bragg peak quickly and have non-linear energy losses already in the first four segments of the IC detector as shown in Figure 5.21 (left). In contrast, the fission fragments lose their energy nearly linearly up to third segment and only then reach the Bragg peak. Thus, alternative calibration parameters

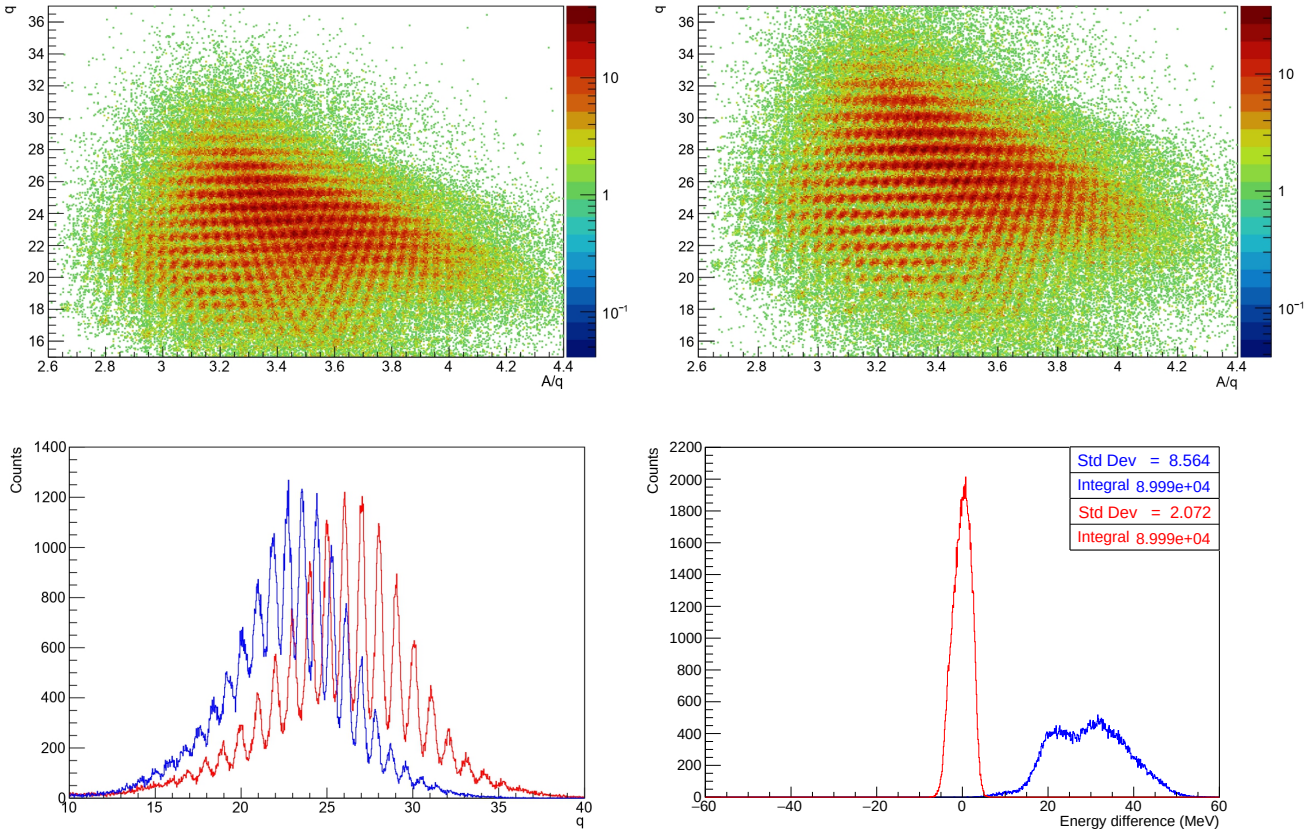

Figure 5.19: The charge state (q) as a function of the reconstructed mass number over charge state (A/q) of the light fission fragments before (top left) and after (top right) minimization. The charge state q (bottom left) and the corresponding energy difference (bottom right) spectra, between E_{rec} and E_{IC}, before (blue) and after (red) minimization.

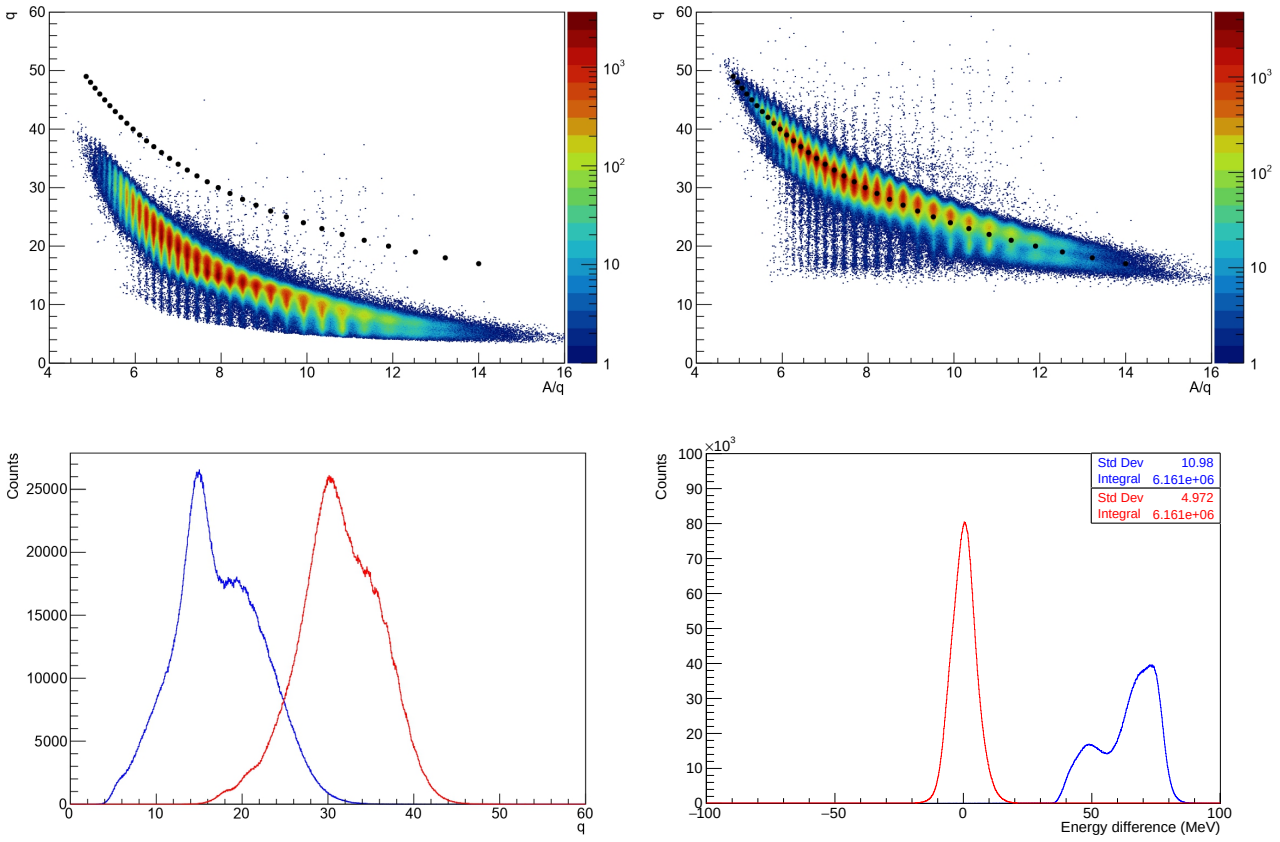

Figure 5.20: The charge state (q) versus the mass number over charge state (A/q) spectra of the uranium-like products calibrated with the parameters obtained based on the minimization of the energies of the fission fragments (top left) and of the uranium-like products (top right). The charge state q (bottom left) and the corresponding energy difference (bottom right), between E_{rec} and E_{IC}, minimized with the parameters obtained based on the region of the fission fragments (blue) and the uranium-like products (red). The black dots illustrate the correct charge state value q for the given A/q of the ^{238}U products.

Table 5.5: The calibration parameters required for the region of uranium-like products of interest.

Segment	a
IC_1	1.822×10^{-3}
IC_2	9.690×10^{-3}
IC_3	6.983×10^{-3}
IC_4	6.369×10^{-3}
IC_5	2.457×10^{-4}
IC_6	4.986×10^{-2}
IC_7	0.

#	p
0	3.214×10^{1}
1	2.930×10^{-3}
2	-7.794×10^{-9}
3	-3.483×10^{-12}

are necessary. To obtain them, the minimization procedure was carried out but this time based on the energies of the uranium-like products. In addition, to recover the not measured energy E_{nm}, the method described in the Ph.D. thesis of D. Ramos [Ram16] was employed. It relies on the linearity of the energy losses in two consecutive layers of material for the energies far from the Bragg peak and estimates the E_{nm} from the energy deposited in the first segment ΔE_{IC_1}, see Figure 5.21 (right). However, the parameters obtained from the estimation did not allow for the minimization to converge and, therefore, they were deduced based on the data instead. The equation for the calibration of the region of interest is now as follows

$$E = E_{rec} = E_{nm} + E_{IC} = p_0 + p_1 IC_1 + p_2 IC_1^2 + p_3 IC_1^3 + \sum_{n=1}^{7} a_n \cdot IC_n \tag{5.16}$$

where p_{0-3} are the parameters to account for the E_{nm} based on the energy lost in first segment IC_1 of the IC detector. The minimized energy difference of the E_{rec} and the E_{IC}, accounting for the E_{nm}, with Equation 5.16 is shown in Figure 5.20 (bottom right). Figure 5.20 (top right) shows resulting q versus A/q spectrum of the uranium-like products. The charge state q values of the products are now close to the correct ones. However, there is still room for improvement as it is not possible to observe a distinct separation of the different charge states q, as shown in Figure 5.20 (bottom left), due to the elongated distribution along each of the A/q for a given q, which has to be reduced. Moreover, the position of the charge states has to be corrected for the products with A/q higher than 8.5. The origin of the vertical lines for the products with A/q from 6 to 10 is not understood. The calibration parameters required for the region of interest is given in Table 5.5.

5.2.2 Atomic Mass and Charge State Identification

The data obtained from the various detectors, after the calibration, and the trajectory reconstruction is used to extract and to identify the reaction products in charge state and atomic mass.

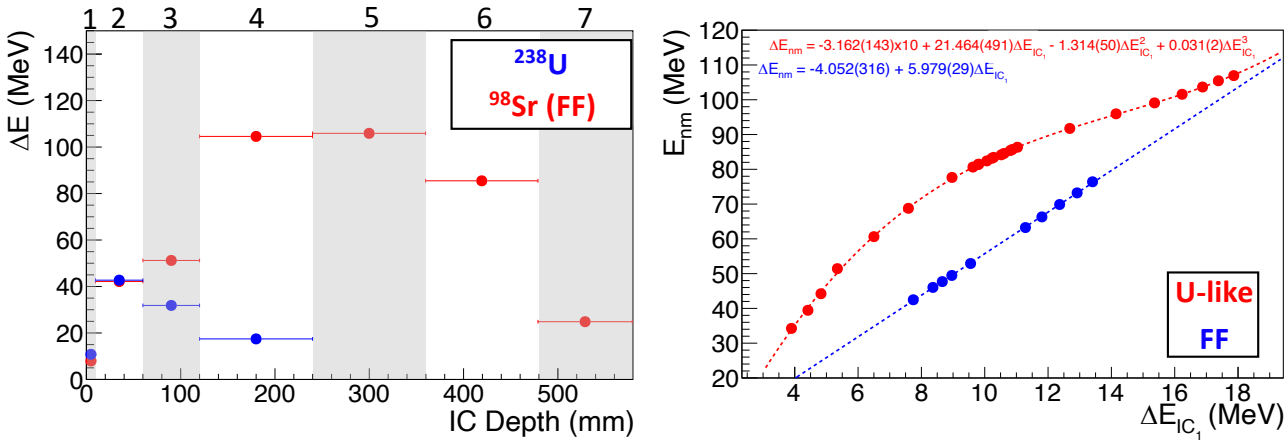

Figure 5.21: Left: The calculated energy loss at $\theta_{\mathrm{lab}} = 40^{\circ}$ using LISE++ [TB] as a function of depth of the IC detector for the fission fragment ^{98}Sr and the elastically scattered ^{238}U for the ^{238}U + ^{238}U reaction at 6.765 MeV/A with the aluminum degrader. The segments of the IC detector are indicated by the numbers from 1 to 7. The Bragg peak of ^{238}U is covered already in the first four segments while for ^{98}Sr in the last segments. The dimensions of the segments were given in Table 3.6. Right: The calculated not measured energy loss $\mathrm{E_{nm}}$ as a function of energy deposited in the first segment of the IC detector $\Delta\mathrm{E_{IC_1}}$ for a few even-A fission fragments with $88 \leq \mathrm{A} \leq 140$ (blue dots) and for U, Np, Pu isotopes (black dots). The distributions are fitted with first-order and third-order polynomial, respectively, represented by the dashed lines. Since the energy range of the fission fragments is far from the Bragg peak the relation between $\Delta\mathrm{E_{nm}}$ and $\Delta\mathrm{E_{IC_1}}$ is linear. This is not a case for the uranium-like products since they are at the Bragg peak region.

The identification algorithm was described in the beginning of Section 5.2 and was illustrated in Figure 5.1.

The reconstructed mass over charge state (A/q) of the reaction products is shown in Figures 5.22 (left) and (right) for the measurements at 7.193 MeV/A and 6.765 MeV/A, respectively, with and without the aluminum degrader. It is evident that the lower the beam energy, the higher the values of the measured A/q distribution of the products. It is also clear that the A/q values increase for the measurements with the degrader compared to the ones without, due to the energy lost in the degrader. The products with the A/q values higher than ∼3.6 and ∼4.5 correspond to the uranium-like products in the measurements without and with the degrader, respectively, while the ones with lower values correspond to the fission fragments. With the assumption that elastically scattered ^{238}U recoils are mostly produced, one can determine the charge states (238/(A/q)) of the reaction products as shown in the insets. It is worth to note that the resolution in A/q improves, due to the improved time of flight (TOF) resolution, with the use of the degrader leading to the energy losses and, hence, the longer TOF of the products.

Figures 5.23 (bottom left) and (bottom right) show the spectra of the charge state (q) as a function of A/q of the reaction products measured at 7.193 MeV/A and 6.765 MeV/A, respectively, employing the aluminum degrader. The spectra were built by means of the gates for the uranium-like products and the fission fragments in the spectra of the velocity (v) versus the energy lost by all the products in the first segment (ΔE_{IC_1}) of the IC detector shown in Figures 5.23 (top left) and (top right). With these gates it was possible to obtain the charge states q of the uranium-like products and the fission fragments by using the different calibration parameters for the IC detector correspondingly. However, the obtained charge states q for the uranium-like products were not distinctly separated, see the discussion in the previous section, making the further mass reconstruction challenging. For both energies, the products that are stopped in the IC detector are included in the spectra. For the fission fragments, only the ones reaching the fifth and sixth segments are shown, for the ones before the fifth segment additional corrections are necessary to account for the not measured energy of the fission fragments which is not the scope of the present work. The vertical lines, with q lower than the ones of the uranium-like products, are present in both spectra and their origin, as mentioned in the previous section, is not understood. The events in the region with q > 40 and A/q > 6 correspond probably to the second partner (TLF[27]) of the uranium-like products. Their incorrect charge state values can be explained by the possibly different location of the Bragg peak region requiring the calibration parameters for the IC detector different from the applied ones. For the measurement without the degrader[28] the data analysis is in progress. In particular, the energy losses of the products in the degrader affecting to the energy measurement in the IC detector and the gain in TOF resolution is being evaluated.

[27] target-like fragment

[28] Data without the aluminum degrader were collected for a total of ∼5 hours with a low beam dose of 7×10^{12} and 9×10^{12} particles for 7.193 MeV/A and 6.765 MeV/A, respectively.

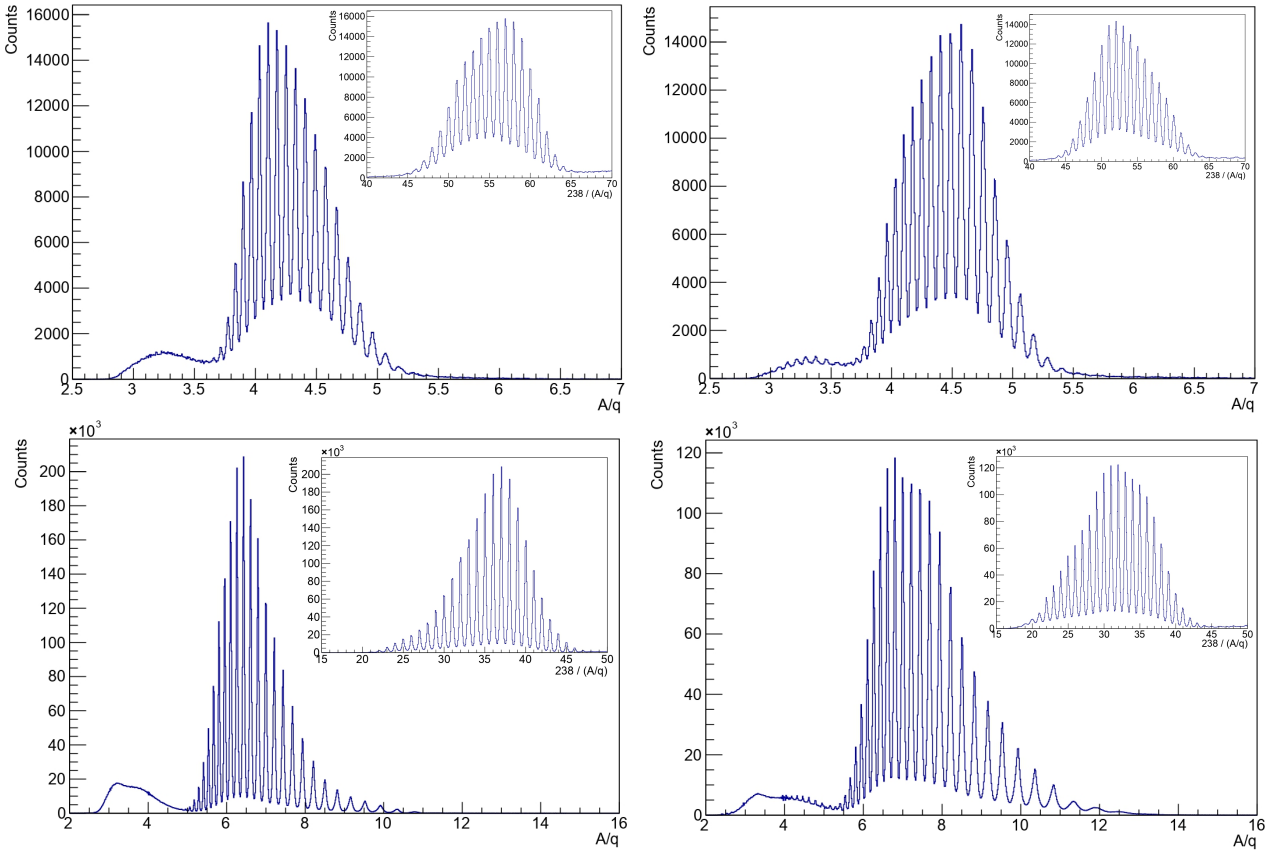

Figure 5.22: The mass over charge state (A/q) of the ^{238}U + ^{238}U reaction products for 7.193 MeV/A (left) and 6.765 MeV/A (right) with (bottom) and without the aluminum degrader. The uranium-like products have A/q values higher than ∼3.6 and ∼4.5 in the measurement without and with the degrader, respectively, and in the lower A/q region the populated fission fragments are shown. The charge states (238/(A/q)) of the products are shown in the insets assuming that the most populated products are ^{238}U.

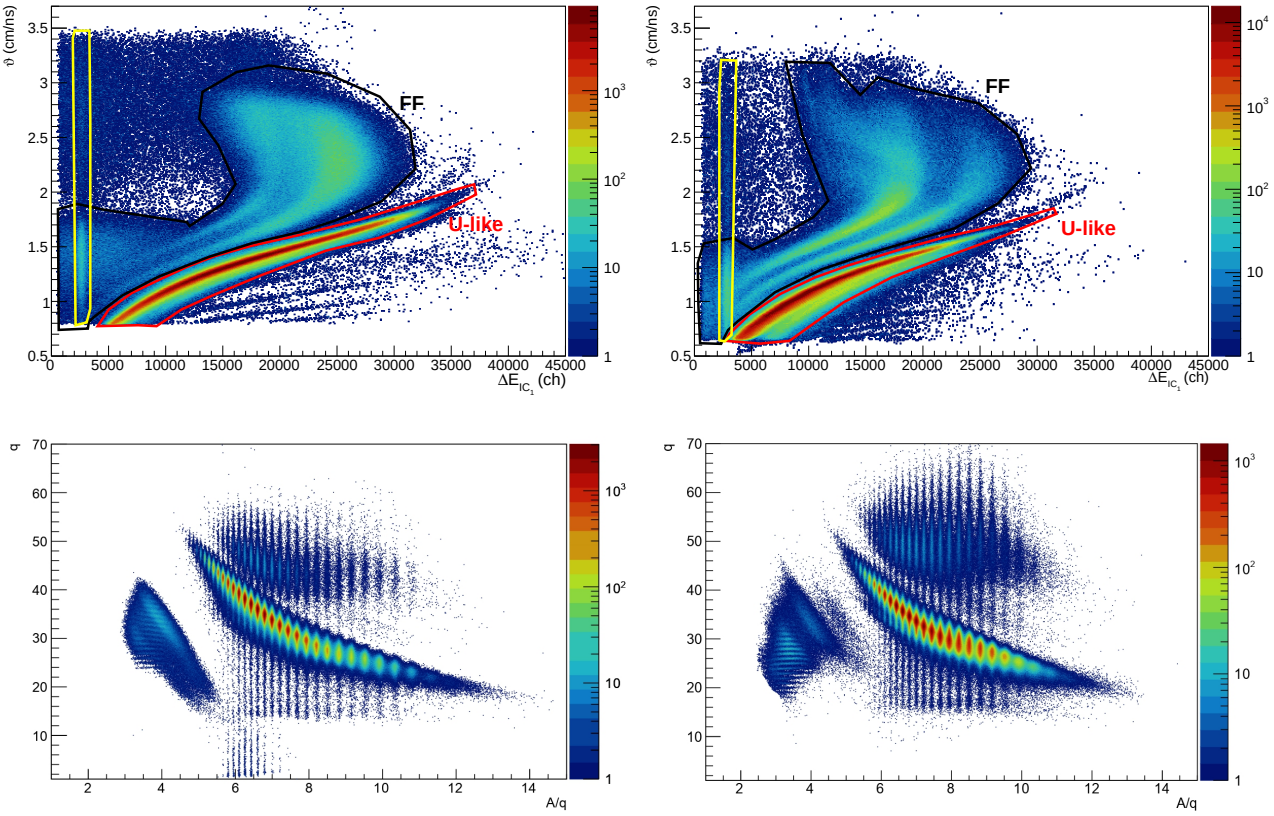

Figure 5.23: The measurement of the ^{238}U + ^{238}U reaction products at 7.193 MeV/A (left) and 6.765 MeV/A (right). Top: The velocity (υ) as a function of the energy deposited in the first segment (ΔE_{IC_1}) of the IC detector of all the products. The cuts in red and black are the gates for the uranium-like products and the fission fragments. The non-physical events, indicated in the region in yellow, are present in both energy spectra and were discarded in the further analysis. Bottom: The charge state (q) versus mass over charge state (A/q) spectra which were built using the aforementioned gates with the corresponding different calibration parameters for the fission fragments and the uranium-like products for the IC detector.

Figures 5.24 (top left) and (top right) show the masses of the products of the ^{238}U + ^{238}U reaction at 7.193 MeV/A and 6.765 MeV/A, respectively, with the aluminum degrader. The masses were reconstructed based on the measured q versus A/q spectra, shown in Figures 5.23 (bottom left) and (bottom right). To reconstruct the masses of the uranium-like products, gates on each of the blobs (well separated in A/q) were selected, due to the elongated and not properly separated distribution of the charges states. From the obtained masses it is evident that the elastically scattered ^{238}U recoils are overwhelming and that there is no indication for the population of transfer products. Nevertheless, the peak of the elastic channel extends to the ±4 nucleon transfer channels

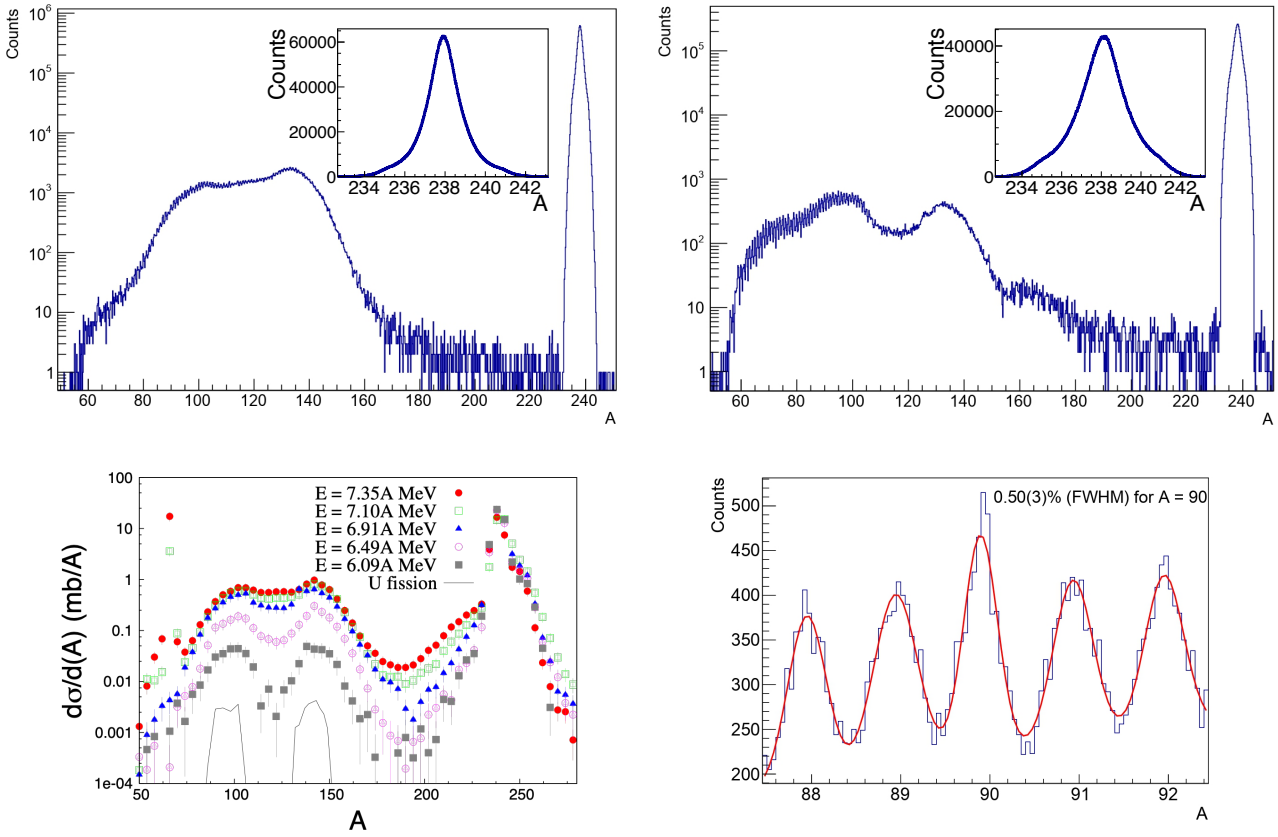

Figure 5.24: Mass spectra of the reaction products measured for beam energies of 7.193 MeV/A (top left) and 6.765 MeV/A (top right) with the aluminum degrader. The mass reconstruction for the uranium-like products was performed using gates for each of the q versus A/q blobs, shown in Figures 5.23 (bottom left) and (bottom right), since the charge states q were not properly separated and have an elongated shape. Bottom left: Same as Figure 2.9 (right), the mass (A) distributions measured with VAMOS at GANIL in 2006 [GHM+10]. The used beam energies are indicated. Bottom right: Closer view at the fission fragment region shown in top right figure, indicating the obtained mass resolution.

region. The distribution of the peak is narrower than the one observed previously by C. Golabek shown in Figure 5.24 (bottom left). However, there is an ambiguity of the upper and lower limits of the peak due to the aforementioned elongation of the measured charge states q. For the fission fragments, the increase of the beam energy leads to a more symmetric distribution as was also pointed out in the previous measurement. The mass resolution ($\Delta A/A$) does not remain the same for the different masses of the products as illustrated in the Ph.D. thesis of D. Ramos [Ram16]. In the present experiment, the mass resolution of $\Delta A/A \simeq 0.50(3)\%$ (FWHM) is obtained for A = 92 in the measurement at 6.765 MeV/A. For A = 238, the mass resolution of $\Delta A/A \simeq 0.48(6)\%$ (FWHM) is obtained in the measurement at two beam energies. To identify the masses of the uranium-like nuclei distinctly, a cleaning is still required by means of recoil-γ-x-ray coincidence analysis. The obtained cross sections for the elastic channel will be further discussed in Section 6.2.2.

5.3 Analysis of ID-Fix data

The ID-Fix array consists of three LEPS detectors. A detailed description of the detectors was presented in Section 3.4.2. The results of the test with the source, studying systematically the signal processing parameters to optimize the response of the detectors for the experimental conditions of high count rates, was reported in Section 4.3. The details of the in-beam test, investigating photon absorbers of various thicknesses to reduce the rates, was given in Section 4.2.3. The LEPS detectors were used for the identification of the atomic charges through the measurement of L and K x-rays emitted by the reaction products. In this chapter, the calibration procedure of the LEPS detectors will be described. Then, the performance of the detectors in terms of resolution and efficiency will be reported. Later, the procedure required to correct the measured energies of the photons due to the Doppler effect will be presented. Finally, the atomic charges of the detected products will be identified based on the characteristic x-ray spectroscopy.

5.3.1 Energy calibration

Energy to channel calibration of the LEPS detectors was performed using a source of ^{152}Eu. Table 5.6 provides the energy values of the photons of the source used for the calibration. The measured peaks of the photons were fit with a Gaussian function plus second-order polynomial as an approximation for the background. For the peaks with well defined Gaussian distribution, the centroids (x) returned by the fit were compared with the known energy values and fitted using a second-order polynomial ($\mathrm{E(keV)} = \mathrm{a} + \mathrm{bx} + \mathrm{cx}^2$) relation as shown in Figure 5.25. The parameters ($\mathrm{a}, \mathrm{b}, \mathrm{c}$) of the resulting relation are given in Table 5.7. Figure 5.26 shows as an example the spectrum of ^{152}Eu for the LEPS #1 detector after the calibration.

Table 5.6: The photon energies of the ^{152}Eu source used for the calibration of the ID-Fix array and AGATA spectrometer.

Radionuclide	Energy (keV) [nnd]
^{152}Eu	45.414
	46.578
	121.7817
	244.6974
	344.2785
	443.9606
	778.9045
	867.38
	964.057
	1085.837
	1112.076
	1408.011

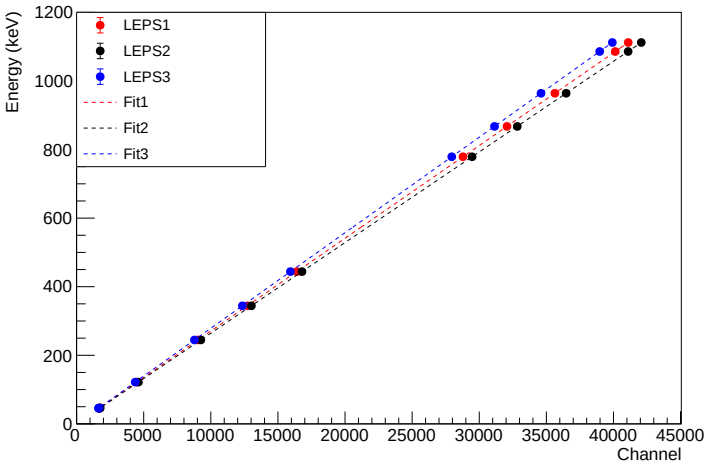

Figure 5.25: Energy to channel calibration of the three LEPS detectors. The dots represent the measured energy values in channel related to the known ones in keV. The dashed lines are the calibration curves using obtained using a second-order polynomial. The obtained parameters are reported in Table 5.7.

5.3.2 Detection efficiency and resolution

The resolution of the detector allows to evaluate its power to discriminate adjacent peaks and to determine its performance to measure a single peak of a photon. The fitting of the peaks of ^{152}Eu

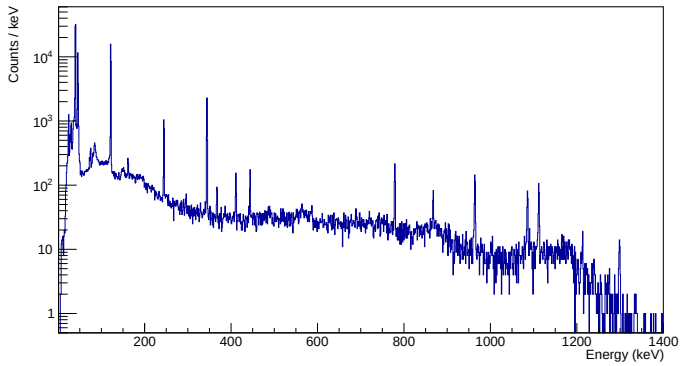

Figure 5.26: Example of the spectrum of ^{152}Eu, after calibration, measured with the LEPS #1 detector.

Table 5.7: Calibration parameters for the three LEPS detectors. Note that a first-order polynomail fit would have been sufficient since parameter c is 8 orders of magnitude smaller than parameter b.

LEPS #	a	b	c
1	0.024(41)	2.70601(57)$\times 10^{-2}$	-0.12(16)$\times 10^{-9}$
2	0.045(40)	2.64351(55)$\times 10^{-2}$	-0.13(15)$\times 10^{-9}$
3	0.037(42)	2.78709(61)$\times 10^{-2}$	-0.21(18)$\times 10^{-9}$

described in the previous section provided the value of the standard deviation (σ) for each of the peaks. Using these values, the Full Width at Half Maximum (FWHM) can be calculated, through the relation $\mathrm{FWHM} = 2\sigma\sqrt{2\ln 2}$, to give the resolution of the detectors in a commonly used term. Figure 5.27 shows the obtained FWHM of the peaks as a function of the energy of the photons for the three LEPS detectors. The energy resolution of the detectors reaches the minimum at around 100 keV and below, which is the region of our interest, allowing to achieve the value of FHWM lower than 1 keV.

The absolute efficiency provides knowledge on the probability of the emitted photon to be detected and fully absorbed by the detector, and allows to obtain the intensity of the photon transition. The measurement of the absolute efficiency (ε) is performed placing the ^{152}Eu source at the target position used in the experiment. The ε was obtained from the number of measured photons $\mathrm{I(E)}$ in the peak with energy E using the following equation

$$\varepsilon = \frac{\mathrm{I(E)}}{\mathrm{Ac(Z,N)b(E)}\Delta\mathrm{t}(1-\mathrm{t_{DT}})} \tag{5.17}$$

where $\mathrm{Ac(Z,N)}$ is the activity of the source, $\mathrm{b(E)}$ is the branching ratio of the decay, $\Delta\mathrm{t}$ is the duration of the measurement, $\mathrm{t_{DT}}$ is the dead time of the acquisition. The value of the $\mathrm{I(E)}$, for a

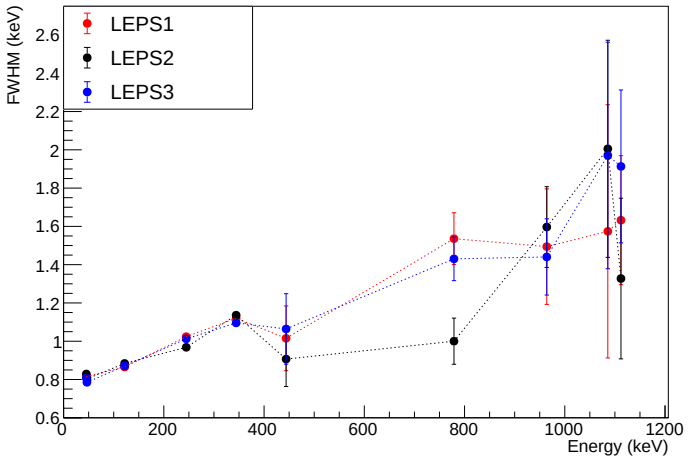

Figure 5.27: Energy resolution (FWHM) as a function of the energies of the photons, emitted from the ^{152}Eu source with an activity of 14541 Bq at the time of the measurement, for the three LEPS detectors. Dotted lines serve to guide the eye.

Gaussian distribution plus second-order polynomial as an approximation for the background, is obtained using the σ and the amplitude (Am), as

$$\mathrm{I(E)} = \mathrm{Am}\sqrt{2\pi}\sigma \tag{5.18}$$

Figure 5.28 (left) shows the ε as a function of the energy of the photons. The detectors are most efficient, around 100 keV and below, with a peak of around 1.7% at the energy of 46.6 keV. To cover the efficiency of the detector over wider energy ranges, describing particularly lower energies of interest, the data were fitted using a function [Kno79], relating the logarithm of ε to the logarithm of the energy as follows

$$\ln\varepsilon = \mathrm{a_0} + \mathrm{a_1(lnE)} + \mathrm{a_2(lnE)^2} + \mathrm{a_3(lnE)^3} + \mathrm{a_4(lnE)^4} \tag{5.19}$$

where $\mathrm{a_{0-4}}$ are the fitted parameters. The outcome of the fit is shown in Figure 5.28 (right) and one can see that the distribution of the data values is reproduced well by the fit.

5.3.3 Doppler Correction

Photons, x-rays and γ-rays, are emitted in flight by moving excited particles. Therefore, the measured energy ($\mathrm{E_{DS}}$) of each photon is shifted in the laboratory frame due to the Doppler effect. The shift in the measured energy depends on the velocity ($\beta = \mathrm{v/c}$) of the particle and the emission angle (θ_{DS}) between the particle and the photon, and can be corrected using the following relation

$$\mathrm{E} = \mathrm{E_{DS}}(1 - \beta\cos(\theta_{\mathrm{DS}}))\gamma \tag{5.20}$$

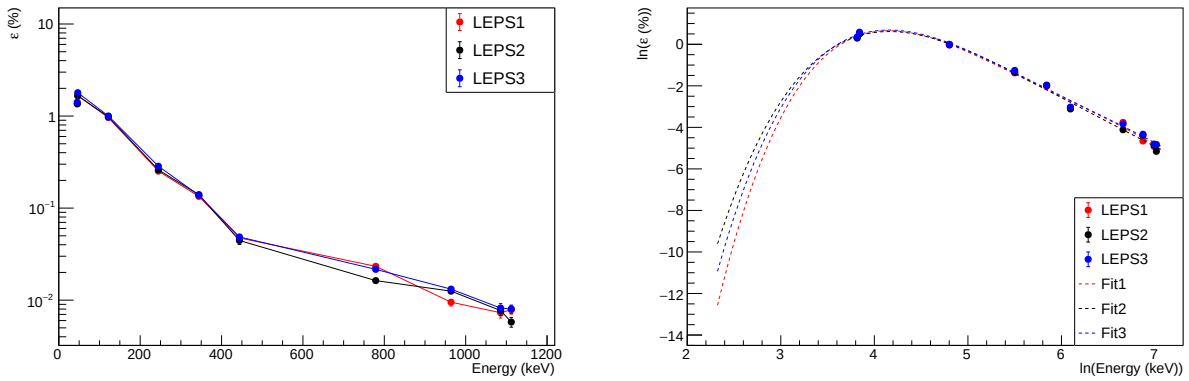

Figure 5.28: Left: efficiency ε as a function of the photon energy for the three LEPS detectors. Solid lines serve to guide the eye. Right: fitting the relation of the logarithm of the ε to the logarithm of the photon energy values using Equation 5.19.

where γ is the Lorentz factor, $\gamma = 1/\sqrt{1-\beta^2}$.

In the present experiment, the β and the θ_{DS} of the reaction products are measured event-by-event. The former is provided by VAMOS++, which measures the time of flight (TOF) for the distance that the particle travels between the entrance DPS-MWPC and the focal plane MWPPAC detectors, with the correction for the energy loss in the aluminum degrader. The latter is determined by the scalar product of the particle ($\vec{r}_{\mathrm{p}}$) and the photon ($\vec{r}_{\mathrm{x},\gamma}$) vectors in the following way

$$\vec{r}_{\mathrm{p}} = \begin{pmatrix} -\sin(\theta_{\mathrm{p}})\cos(\phi_{\mathrm{p}}) \\ \cos(\theta_{\mathrm{p}})\cos(\phi_{\mathrm{p}}) \\ \sin(\phi_{\mathrm{p}}) \end{pmatrix} \quad \text{and} \quad \vec{r}_{\mathrm{x},\gamma} = \begin{pmatrix} -\sin(\theta_{\mathrm{x},\gamma})\cos(\phi_{\mathrm{x},\gamma}) \\ \cos(\theta_{\mathrm{x},\gamma}) \\ \sin(\theta_{\mathrm{x},\gamma})\sin(\phi_{\mathrm{x},\gamma}) \end{pmatrix} \tag{5.21}$$

where (θ_{p}, ϕ_{p}) and ($\theta_{\mathrm{x},\gamma}$, $\phi_{\mathrm{x},\gamma}$) are the angles of the particle and the photon, respectively, with respect to the axis of VAMOS++. The particle angles (θ_{p}, ϕ_{p}) are provided by the DPS-MWPC detector of VAMOS++, see Section 5.2.1.1. For the photon angles ($\theta_{\mathrm{x},\gamma}$, $\phi_{\mathrm{x},\gamma}$), either the position of the LEPS detectors of ID-Fix, see Section 3.4.2, or the first interaction point provided by AGATA, see Section 3.4.3, are used depending on the detector measuring the photon. An illustration of the aforementioned angles defined relative to the axis of VAMOS++ is shown in Figure 5.29.

Figure 5.30 shows the measured photon spectra of the uranium-like products before and after the Doppler correction. The gate of on mass 238 measured by VAMOS++ was to make sure that only the photons of the uranium-like products contribute to the spectra. In addition, the employed angle θ_{DS} was relative to the partner respective to the one detected with VAMOS++ assuming a pure binary reaction, i.e. a two-body reaction and the partner travels perpendicular to the one entering VAMOS++. The β of the partner was deduced based on the momentum conservation

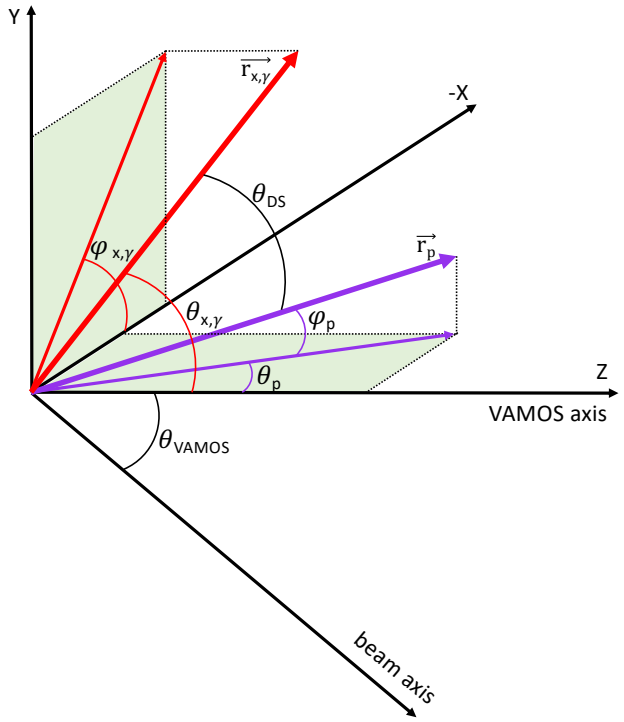

Figure 5.29: Schematic diagram illustrating the trajectories of the particle and the photon. All of the angles are represented with respect to the VAMOS++ axis and were used to obtain the angle θ_{DS} between the particle and the photon. The position of the LEPS detectors were given in Table 3.7. The coordinate system, in which the position of the detectors was provided, was kept as it was given by the mechanics group of GANIL, see text for the parameter definition.

as well as considering the energy lost in the target and the degrader calculated by LISE++. A slight shift in the Doppler corrected energies of the peaks of the x-rays and the γ-rays is due to the limited precision in the position of the photon interaction point resulting from the angular opening of around 6° of the LEPS detector.

5.3.4 Atomic Charge Identification

The data collected with the LEPS detectors, after the energy calibration and the Doppler correction, are used for the identification of the atomic charge (Z) of the reaction products. In the present experiment, the identification in Z is based on the measurement of characteristic K and L x-rays. The measurements of this kind was first utilized by Moseley in 1913 [M.A13, M.A14], who had discovered that the frequency (ν) of the x-ray is directly related to the atomic charge of the emitting atom $\nu \propto Z$.

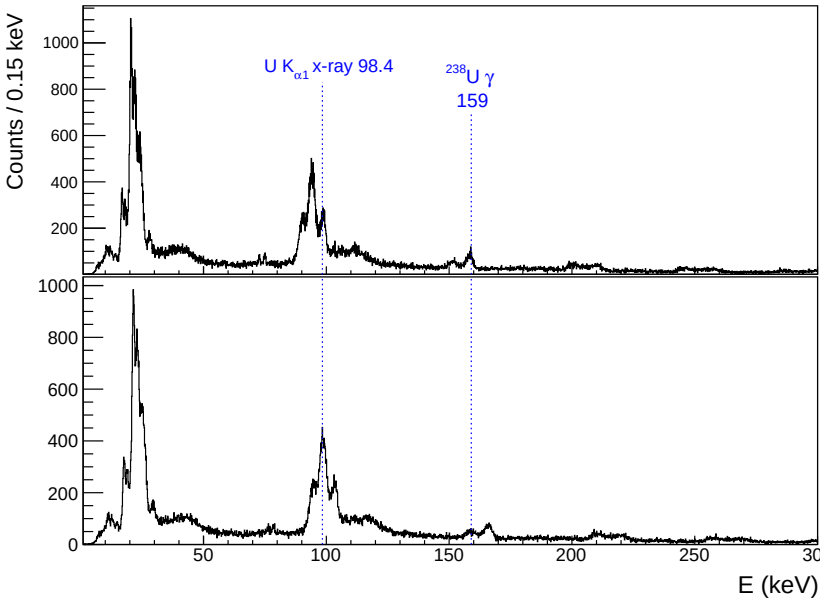

Figure 5.30: Photon spectra for uranium-like products, obtained with a gate on mass 238 measured with VAMOS++, collected with the LEPS #1 detector before (top panel) and after (bottom panel) the Doppler correction (DC). The DC is performed for the partner respective to the one measured in VAMOS++, for the measured one the correction is minimum as the emission angle θ_{DS} is close to 90 degrees.

The emission of characteristic x-rays is a form of energy removal and occurs by internal conversion where an electron is knocked out from inner shell, leaving a vacancy, close to the nucleus, de-exciting the nucleus. The x-rays come from an outer shell electrons falling into the vacancies. The energy of the emitted x-ray is given by the difference in binding energies between the initial and final states which are unique for each element. Auger electrons are kicked out from the atomic shell by external atomic excitations leading to the Auger cascades where electrons further out from the vacancy fall into the hole left by the Auger electron emitting x-rays of the energy differences between initial and final states.

Figure 5.31 (top) shows a 2-D spectrum with the photons detected by the LEPS #1 detector in coincidence with the uranium-like products measured with VAMOS++ at 6.765 MeV/A with the aluminum degrader mounted behind the the target. The most intense peaks of L and K x-rays are visible for the all masses, which permit the identification of the products to be uranium. It is worth to note that the threshold for low energies reached down to around 10 keV allowing the measurement of L x-rays of uranium. To verify the determined masses, gates on even-A uranium isotopes with masses from 234 to 242 were selected. Figure 5.31 (bottom) shows the mass gated photon spectra. The indication of contributions to the photon spectra of the recoils with masses

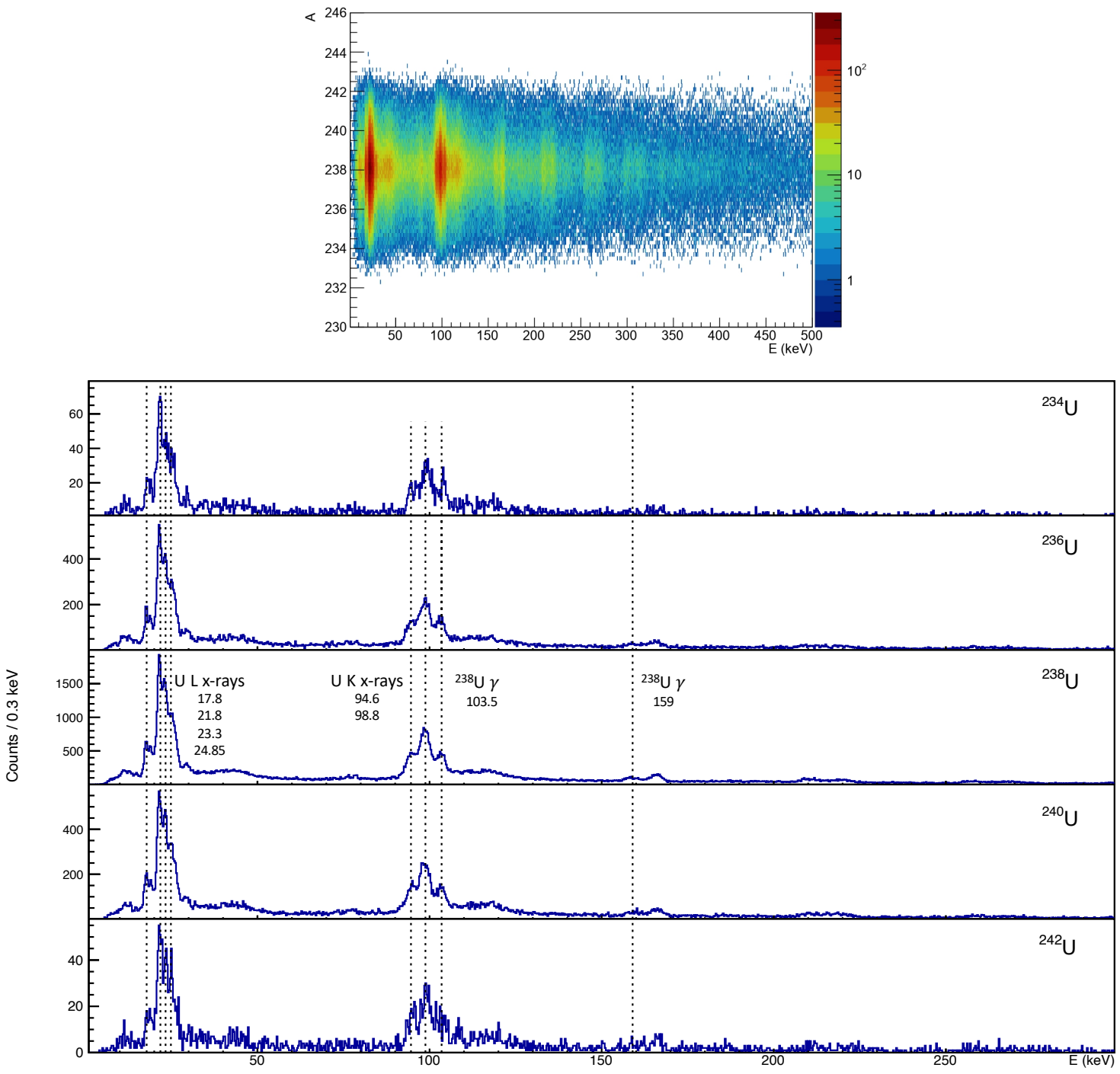

Figure 5.31: Top: Photons measured with the LEPS #1 detector in coincidence with the uranium-like recoils with the masses (A), shown in Figure 5.24 (top right), at 6.765 MeV/A with the degrader. Bottom: Spectra of photons gated on even-A from 234 to 242. The energies of the measured L and K x-rays of the uranium element as well as the γ-rays of the rotational band members of ^{238}U are indicated.

different from ^{238}U would be if the change of the γ-ray energies takes place from one mass to the other while the L and K x-rays energies remain the same. However, as one can see the γ-ray peaks have no change in energy. The γ-ray peaks are associated with the rotational band members of ^{238}U. In this way, it is clear that the only component contributing to the spectra is ^{238}U.

5.4 Analysis of AGATA data

The technical details of the AGATA γ-ray spectrometer were given in Section 3.4.3. This section starts with a brief description of the energy calibration. Then, it provides information for the resolution and the detection efficiency. Later, the detected x-rays and γ-rays, with the energies corrected for the Doppler effect, from atomic and nuclear de-excitations of the identified reaction products will be used to verify their origin.

5.4.1 Energy calibration

The energy calibration of the AGATA spectrometer was performed using sources of ^{152}Eu and ^{60}Co by the AGATA collaboration. The information on the sources can be found in Table 5.6 and 5.8. As an example the calibrated spectrum of ^{152}Eu measured with the AGATA spectrometer is shown in Figure 5.32.

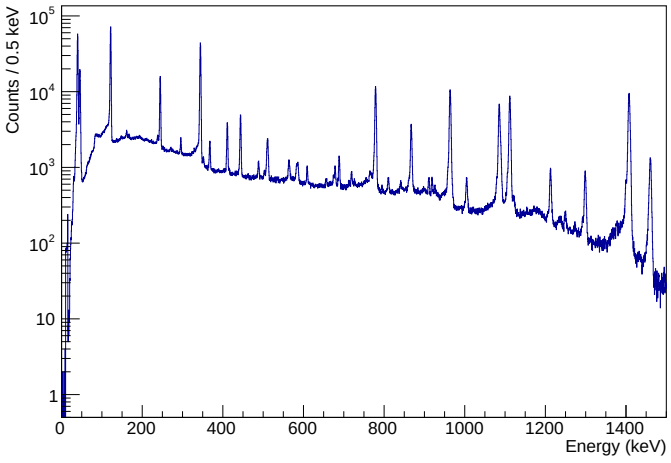

Figure 5.32: Example of the spectrum of ^{152}Eu, after calibration, measured with all of the AGATA detectors.

Table 5.8: The energies of the γ-rays of the ^{60}Co used for the calibration of the AGATA.

Radionuclide	Energy (keV) [nnd]
^{60}Co	1173.228
	1332.492

5.4.2 Detection efficiency and resolution

The risetime of the trapezoidal filter was chosen to be 5 μs (see Section 4.3) to process the signals of the AGATA spectrometer, as a compromise between event rejection rate and resolving power. The performance of the spectrometer in terms of efficiency and resolution is measured in the same way as for the ID-Fix array, as it was described in Section 5.3.2, using a source of ^{152}Eu.

Figure 5.33 and 5.34 show the absolute efficiency (ε), with a fit using a fifth-order polynomial, and the FWHM as a function of γ-ray energies. Based on the fit, an ε of around 9.3 % was obtained for the energy at 100 keV, which is the region of our interest for the measurement of K x-rays of the uranium-like products.

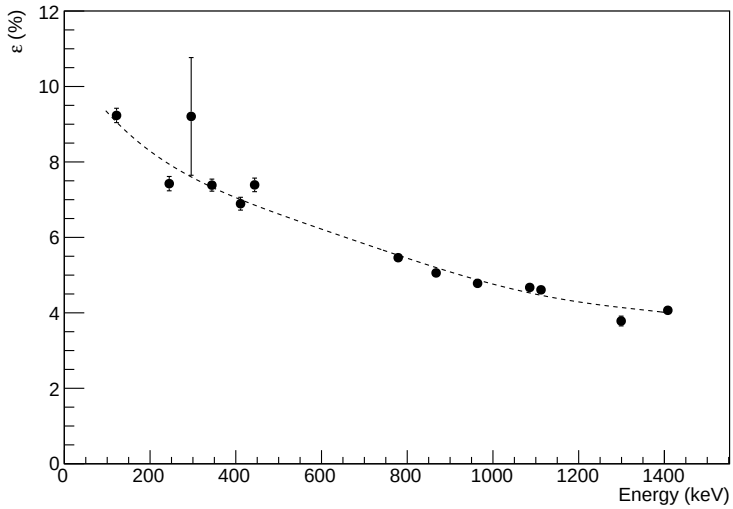

Figure 5.33: Absolute efficiency (ε) as a function of the γ-ray energy obtained with AGATA using a source of ^{152}Eu. The dashed line represents a fit performed using a fifth-order polynomial.

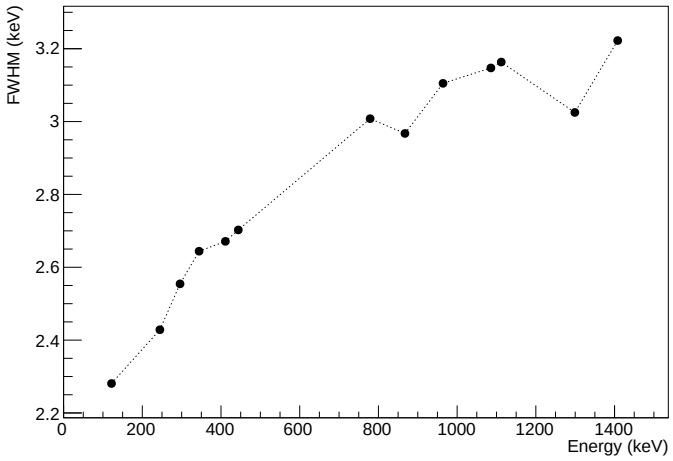

Figure 5.34: Energy resolution (FWHM) as a function of the energies of the γ-rays, emitted from the ^{152}Eu source, measured with the AGATA spectrometer. Dotted lines serve to guide the eye.

5.4.3 Gamma-ray spectroscopy

The measurement of the γ-rays were triggered by the recoils detected in VAMOS++ to record only the coincident events. However, as shown in Figure 5.35, events corresponding to more than one cyclotron pulses, delivering the beam with a period of around 110 ns, contribute to the spectra. In order to reduce the amount of random coincidences, a gate on the most intense peak was selected. In the further analysis the events within this gate will be discussed.

Figure 5.36 shows the γ-rays and x-rays of the uranium-like recoils measured with the AGATA spectrometer before and after the Doppler correction (DC). The details of the procedure required for the DC were described in Section 5.3.3. The energies of the photons emitted from the uranium recoils measured by VAMOS++ are well corrected. The contribution of the respective partner is visible as broadened peaks in the not Doppler corrected spectra.

Figure 5.37 (top) shows a 2-D spectra of coincident events of photons detected with AGATA and the recoils measured with VAMOS++ for the 6.765 MeV/A beam energy with the aluminum degrader. In contrast to the LEPS spectra, γ-rays with energies higher than 300 keV and no L x-rays are visible. A verification of the determined masses was performed gating on the even-A uranium isotopes from 234 to 242 as shown in the photon spectra in Figure 5.37 (bottom). The K x-rays of the uranium element can be observed for all the masses. Same as in the LEPS spectra, the energies of the γ-ray peaks do not change from one mass to the other and correspond to the γ-rays of the rotational band members of the ^{238}U recoils. The products different from ^{238}U could possibly be observed via recoil-γ-x-ray coincidence analysis which is in progress.

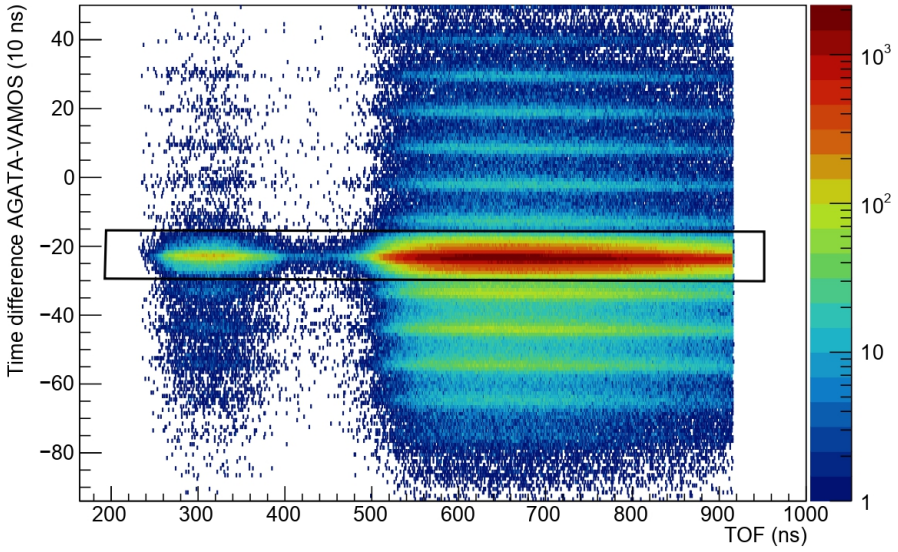

Figure 5.35: Timestamp difference between AGATA and VAMOS++ as a function of the measured time of flight of the recoils provided by VAMOS++. Spectra include all the recoil-photon coincident events. Each peak corresponds to the different pulses of the cyclotron delivering the beam with a period of around 110 ns. The gate in black was selected to avoid the contribution of random coincidences.

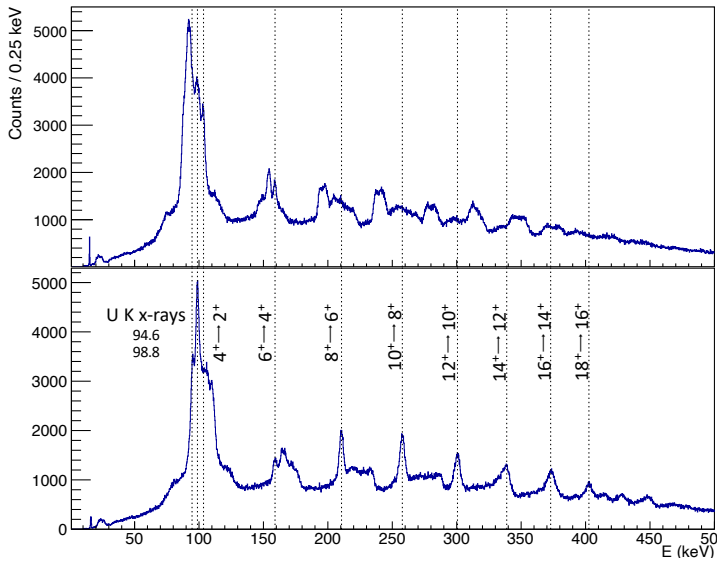

Figure 5.36: Photon spectra taken with AGATA for uranium-like products, obtained with a gate on mass 238 measured with VAMOS++, before (red) and after (blue) the Doppler correction (DC). The DC is performed for the partner measured by VAMOS++.

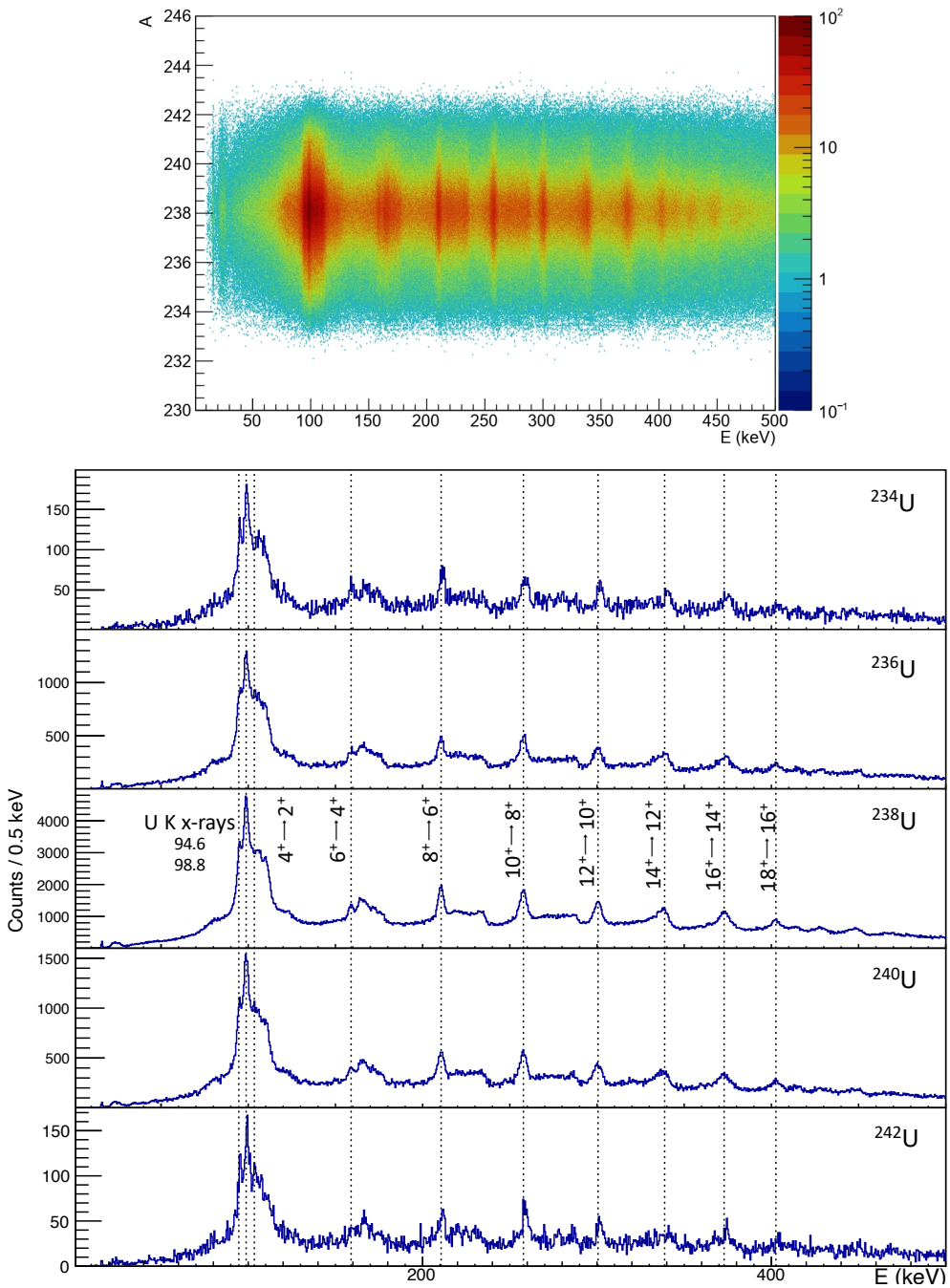

Figure 5.37: Top: Photons detected with the AGATA in coincidence with the uranium-like recoils with the masses (A), shown in Figure 5.24 (top right), at 6.765 MeV/A with the degrader. Bottom: Spectra of photons gated on even-A from 234 to 242. The energies of the measured K x-rays of the uranium element as well as the γ-rays of the rotational band members of ^{238}U are indicated.

Chapter 6

Results and Discussion

Contents

6.1 Introduction

In this chapter, the results obtained from the analysis of the ^{238}U + ^{238}U experiment data collected with VAMOS++, AGATA and ID-Fix will be reported. First, the cross sections limit in the present measurement were obtained taking into account the efficiency of AGATA and ID-Fix, and the transmission of VAMOS++. Then, the cross section for the elastic scattering will be extracted from the measured yields and compared to the calculated ones. Finally, the results on the post-experiment measurement of the decay of long-lived products with ID-Fix will be reported.

6.2 Production cross sections

6.2.1 Limit cross section

The accumulated beam dose, see Section 3.2, was not sufficient to observe any transfer channels, therefore it is reasonable to determine the cross section limit (σ_{limit}) obtained in the experiment of the present work.

The determination of the differential cross section ($\frac{\mathrm{d}\sigma}{\mathrm{d}\Omega}$) can be performed using the following relation

$$\frac{\mathrm{d}\sigma}{\mathrm{d}\Omega} = \frac{\mathrm{N_d}}{\mathrm{N_b} \cdot \mathrm{N_t} \cdot \Delta\Omega \cdot \varepsilon_{\mathrm{tr}} \cdot (\varepsilon_{\mathrm{AGATA}} + \varepsilon_{\mathrm{ID-Fix}})} \tag{6.1}$$

where $\mathrm{N_b}$ is the number beam particles, $\mathrm{N_t}$ is the number target nuclei per unit area and $\mathrm{N_d}$ is the number of detected particles which is in our case the number of the uranium-like products. The terms $\varepsilon_{\mathrm{tr}}$ and $\Delta\Omega$ stand for the transmission efficiency and the solid angle coverage of the VAMOS++ spectrometer, respectively. The terms $\varepsilon_{\mathrm{AGATA}}$ and $\varepsilon_{\mathrm{ID-Fix}}$ are the absolute efficiencies of the AGATA γ-ray spectrometer and ID-Fix array. They provide a total of 12.2(2)% of absolute efficiency[29] for an energy of the photon at $\sim$100 keV.

In the present experiment, the number of beam particles is obtained from the information on the intensity which was monitored by means of a Faraday cup placed in the beam line before VAMOS++. This information is not accurate resulting in a systematic error of $\sim$40%. The intensity and the accumulated beam dose were given in Table 3.1. The information on the thicknesses of the used targets was given in Table 3.2.

In a large solid angle spectrometer like VAMOS++ the entering particles are transported through the ion optical system in a complex way, making, therefore, the number of detected particles

[29]The absolute efficiency of AGATA and ID-Fix was measured with the calibration source placed at the target position, enabling, in this way, to have the same configuration as in the experiment and to neglect the geometrical dependency.

strongly dependent on the transmission efficiency $\varepsilon_{\rm tr}$. This is demonstrated in Figure 6.1 showing the uranium-like products measured in the DPS-MWPC detector at the entrance without and with gates on the ones detected in the first MWPPAC and IC detectors at the focal plane of the spectrometer. The reduction of the amount of events is visible due to the loss in transmission efficiency of VAMOS++. To make sure on the products being uranium-like, a gate on the 159 keV γ-ray or the K x-rays of the elastically scattered ^{238}U was selected in the AGATA spectrum, or the ID-Fix spectrum. The transmission efficiency $\varepsilon_{\rm tr}$ was obtained by means of the following relation

$$\varepsilon_{\rm tr} = \frac{N_{\rm d}^{\rm IC}}{N_{\rm d}^{\rm DPS-MWPC}} \tag{6.2}$$

where $N_{\rm d}^{\rm IC}$ and $N_{\rm d}^{\rm DPS-MWPC}$ are the number of the uranium-like products detected in the IC and the DPS-MWPC detectors, respectively. The $\varepsilon_{\rm tr}$ of 21.26(7)% and 20.48(6)% were deduced for the whole angular acceptance of VAMOS++ for the ^{238}U + ^{238}U measurements at 7.193 and 6.765 MeV/A, respectively.

The measurement of the reaction products is performed within the solid angle $\Delta\Omega$ of $\sim$100 msr thanks to the high acceptance of VAMOS++ [RLN+11] and the possibility of mounting its entrance DPS-MWPCs [VLR+16] detector as close as $\sim$140 mm to the target position. The reaction cross

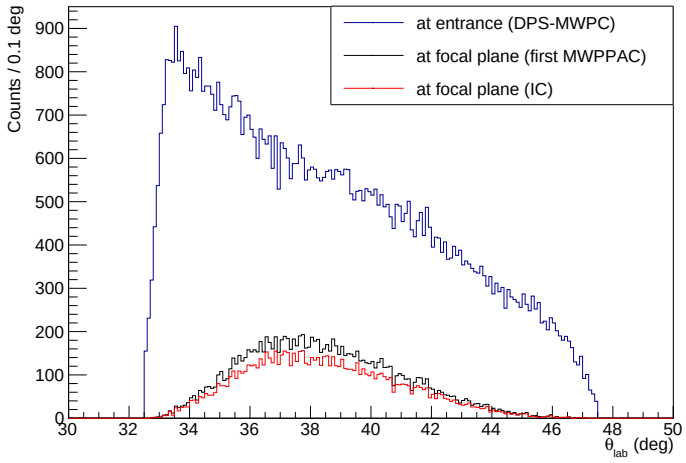

Figure 6.1: The scattering angle in $\theta_{\rm lab}$ of the uranium-like reaction products, with a gate on the 159 keV γ-ray of ^{238}U detected in AGATA, demonstrating qualitatively the transmission efficiency of the VAMOS++ spectrometer for one of the runs, with the aluminum degrader, at 6.765 MeV/A of beam energy. The blue curve illustrates the total amount of events at the entrance of VAMOS++ measured with the DPS-MWPC detector. The same distribution selecting the one, with A/q > 5 which corresponds to the uranium-like products, detected in the MWPPAC and IC detectors are shown by the black and the red curves, respectively.

Table 6.1: The limit cross sections σ_{limit}, together with parameters used for calculation, obtained in the present experiment for the two beam energies for the total angular acceptance (θ = $\pm 7^{\circ}$, ϕ = $\pm 11^{\circ}$) of VAMOS++ placed at θ_{lab} = 40°.

E_{beam} (MeV/A)	N_b (particles)	N_t (particles/cm^2)	ε_{tr} (%)	$\varepsilon_{\text{AGATA}}$ + $\varepsilon_{\text{ID-Fix}}$ (%)	σ_{limit} (μbarn)
7.193(4)	2.1(8) $\times 10^{14}$	1.56$\times 10^{18}$	21.26(7)	12.2(2)	$\sim$11(4)
6.765(3)	4.7(14) $\times 10^{14}$	1.56$\times 10^{18}$	20.48(6)	12.2(2)	$\sim$5(2)

section (σ) for the products accepted within $\Delta\Omega$ can be determined by integrating the $\frac{d\sigma}{d\Omega}$, from Equation 6.1, over all the angles as follows

$$\sigma = \int \frac{d\sigma}{d\Omega}\Delta\Omega = \frac{N_d}{N_b \cdot N_t \cdot \varepsilon_{tr} \cdot (\varepsilon_{\text{AGATA}} + \varepsilon_{\text{ID-Fix}})} \tag{6.3}$$

Considering the detection of at least N_d = 100 recoil-photon coincident events of interest and accounting for the transmission of the spectrometer, the limit cross sections σ_{limit} can be obtained. Table 6.1 reports the values of the obtained σ_{limit}, together with the used parameters, for the measurements at two beam energies for the total angular acceptance of VAMOS++ placed at a grazing angle of θ_{lab} = 40°. Although the obtained σ_{limit} values are comparable to the ones of 5-10 μbarn cross sections envisaged in the experiment proposal for the transfer of ± 5 uranium-like nucleons, according to the GRAZING and the Langevin-type dynamical models (see Section 2.3.1), it was not possible to observe any transfer channels. This suggests that the models overestimate the cross sections required for the transfer, and the accumulation of statistics assumed in the proposal, which is not our case with only $\sim$20 % of the requested beam dose, would make the measurement possible.

6.2.2 Elastic channel cross section

The only component that was possible to observe in the present experiment is the elastic + quasielastic channel, i.e. elastically scattered ^{238}U products, see Figure 2.8 for the calculated Rutherford cross section and the energies of the ^{238}U + ^{238}U reaction. It overwhelms all other reaction channels of interest as it was discussed in Section 5.2.2. To quantitatively understand the contribution of the elastic channel, one can obtain the associated cross sections and angular distributions making use of Equation 6.1.

The missing parameter for the determination of the cross section is the transmission efficiency ($\varepsilon_{tr}(\theta_{\text{lab}})$) of the VAMOS++ spectrometer as a function of scattering angle (θ_{lab}). This information was deduced using the same method described in the previous section, by gating on θ_{lab}, provided by the DPS-MWPC detector, in addition. The resulting angle dependent transmission efficiencies

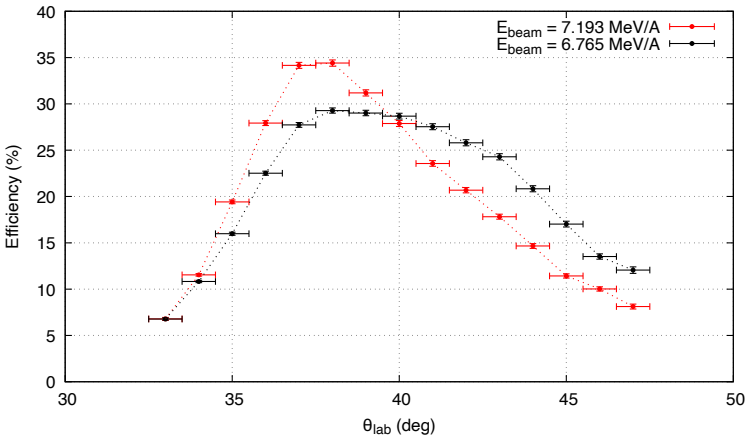

Figure 6.2: Transmission efficiency as a function of scattering angle of the uranium-like products for the measurements at two beam energies with the aluminum degrader. VAMOS++ was placed at 40°. Dotted lines serve as a guide to the eye.

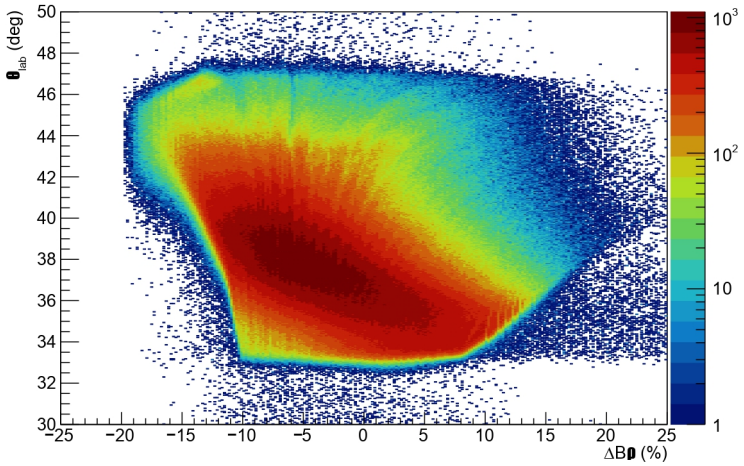

Figure 6.3: Spectrum of the relative magnetic rigidity $\Delta B\rho$ as a function of scattering angle θ_{lab} for the reaction products transmitted through VAMOS++ for 7.193 MeV/A. The $\Delta B\rho$ is equal to $((B\rho/B\rho_0 - 1)\times 100$ with $B\rho_0$ being reference magnetic rigidity for the the products along the central trajectory of the spectrometer.

$\varepsilon_{\mathrm{tr}}(\theta_{\mathrm{lab}})$ of VAMOS++ for the two beam energies are shown in Figure 6.2. The maximum efficiency $\varepsilon_{\mathrm{tr}}$ is observed at 38°, for both of the energies, with a decrease towards the edges due to the shape of the quadrupole cutting the acceptance of the spectrometer. The difference in the shape of the distribution at two energies is attributed to the strong dependence of the detected product on the magnetic rigidity (Bρ), see an example of relative Bρ versus θ_{lab} spectrum shown in Figure 6.3. The reference magnetic rigidity Bρ_0 for the measurements at 7.193 and 6.765 MeV/A was set to 0.97 and 0.85 Tm, respectively.

The number of detected ^{238}U products $\mathrm{N_d}$ reaching the IC detector are extracted by gating on the scattering angle (θ_{lab}) of the products from 33° to 47° with a step of 1 degree. To determine the corresponding numbers at the entrance of the spectrometer, the aforementioned angle dependent transmission efficiency $\varepsilon_{\mathrm{tr}}(\theta_{\mathrm{lab}})$ was used. The cross sections as a function of scattering angle θ_{lab} are obtained from the extracted yields which are used to compare with the calculated ones provided by the GRAZING program. Figure 6.4 shows the angular distribution of the elastic cross section normalized to the calculated value at 37°. The deviation of the value at 33° from the main trend is due to the inefficiency associated with the field inhomogenities occuring at the edges of the DPS-MWPC detector. At both energies, the decrease of the distribution at around 40° is evident, confirming the grazing angle predicted by the GRAZING program, see Figure 6.4. For 7.193 MeV/A, the calculation reproduces the data with a small deviation at backward angles. However, for 6.765 MeV/A, the calculated angular distribution is much wider than the data, particularly, for more backward angles the experimental values are significantly lower. This might be due to reduced efficiencies for those angles associated with instrumental features. This, however, contradicts the previously measured transmission efficiencies of VAMOS++.

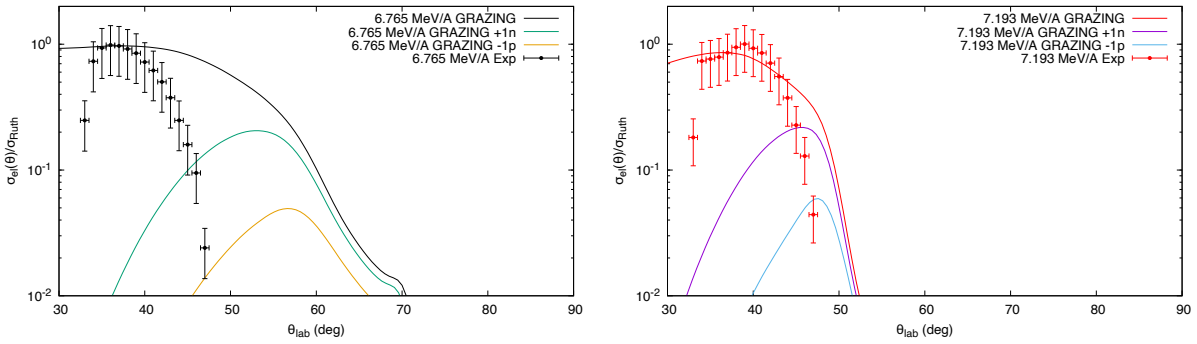

Figure 6.4: Experimental and calculated, using the GRAZING program [Szi20, Win], differential cross sections for the elastic+inelastic scattering, as well as one nucleon transfer, normalized to Rutherford. Statistical and systematic errors are included. The results for only the runs with the same settings of the VAMOS++ spectrometer, e.g. the pressure of the DPS-MWPC and MWPPAC detectors is 3 mbar.

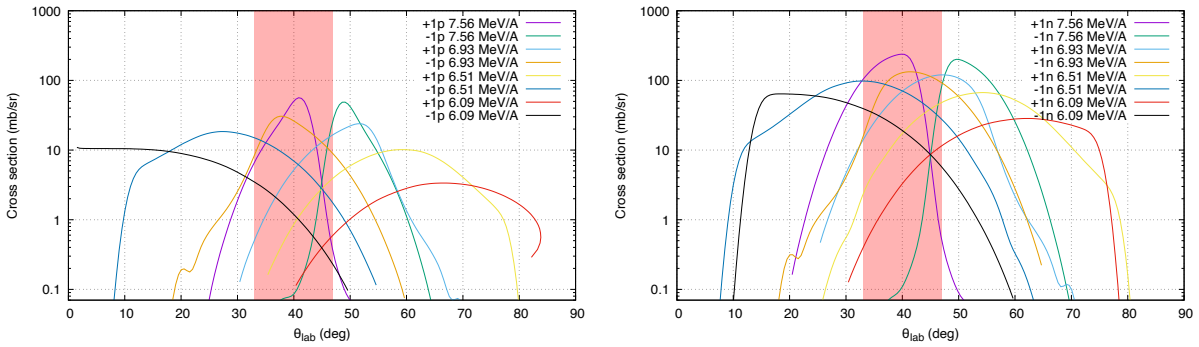

Figure 6.5: One nucleon transfer as a function of scattering angle for ^{238}U + ^{238}U reaction at various beam energies calculated using the GRAZING program [Szi20, Win]. The peak for two highest beam energy can be seen at around 40°. The shaded area is the region covered with VAMOS++ placed at 40°.

Figure 6.5 shows the calculated cross sections for one nucleon transfer as a function of scattering angle for various beam energies. The maximum cross sections of around 10 mb/sr are calculated for for two highest beam energy for θ_{lab} 40°. The calculation shows the angular distribution gets wider as the energy decreases. Depending on the beam energy a significant amount of loss of the distribution is evident for the measurement with VAMOS++.

6.3 Post-experiment catcher foil measurement

The aluminum degrader, used to slow down the reaction products, served as a catcher foil at angles $\theta_{\mathrm{lab}} > 52.5°$ with respect to the beam axis for $\mathrm{E_{beam}}$ = 6.765 MeV/A. To search for the decay of long-lived products stopped in the aluminum degrader, emitted γ-rays and x-rays were measured after the experiment using ID-Fix. Figure 6.6 shows single and coincident spectra. ^{237}Np and ^{239}Pu nuclei were identified by gating on the associated γ-rays and observing the coincident K and L x-rays of neptunium and plutonium. They were produced via β decay of ^{237}U ($\mathrm{T_{1/2}}$ = 6.75 d) $\rightarrow$ ^{237}Np, and ^{239}U ($\mathrm{T_{1/2}}$ = 23 min) $\rightarrow$ ^{239}Np ($\mathrm{T_{1/2}}$ = 2.35 d) $\rightarrow$ ^{239}Pu confirming that the strongest ($\pm 1n$) transfer channels were populated in the present experiment.

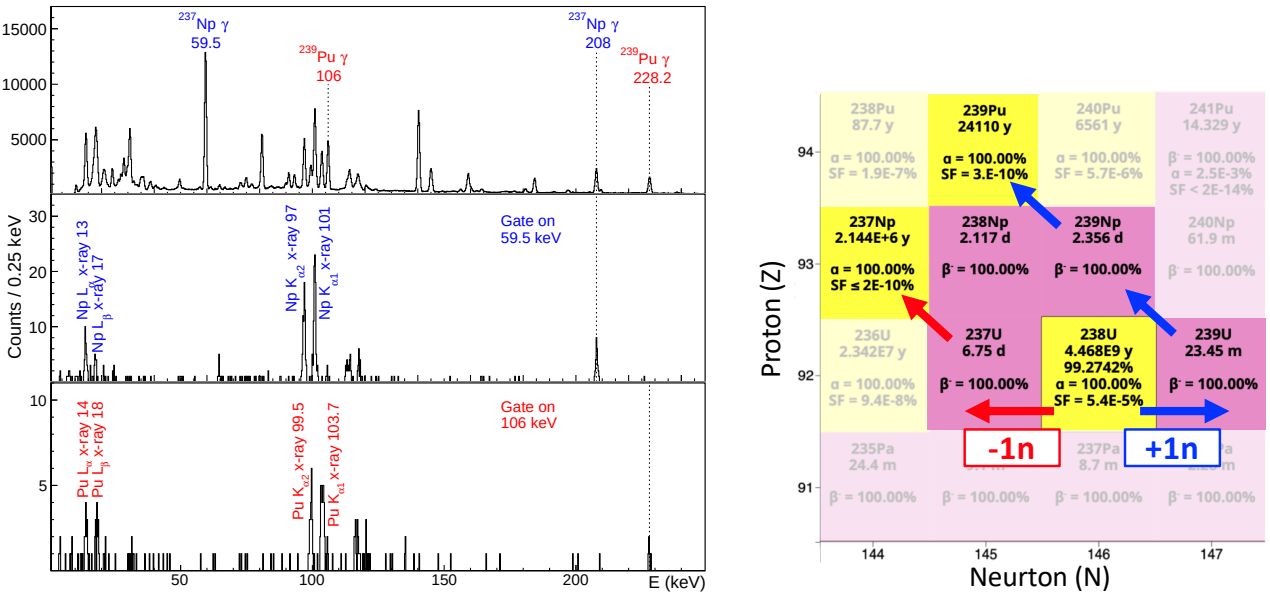

Figure 6.6: Right: Post-experiment measurement of the aluminum degrader carried out with the ID-Fix array. Single LEPS spectra (top). L and K x-rays detected in coincidence with 59.5 and 106 keV γ-rays of ^{237}Np (middle) and ^{239}Pu (bottom), respectively. Left: nuclear chart illustrating the origin and decay path of the observed products. X-rays and γ-rays, emitted from the reaction products implanted into the Al degrader, measured with ID-Fix. Top panel: Single spectrum. Spectra gated on the 59.5 keV γ-ray of ^{237}Np and 106 keV γ-ray of ^{239}Pu are shown in the middle and the bottom panel, respectively (see text for details).

Chapter 7

Conclusion and Outlook

Understanding the production mechanism and also nuclear structure properties of neutron-rich light actinide nuclei in the region of the N = 152 deformed shell gap could provide a valuable input for theoretical and experimental investigations to approach the region of spherical shell stabilized superheavy nuclei. The present work reports on an attempt to measure multinucleon transfer (MNT) cross sections in the ^{238}U + ^{238}U reaction to verify the predicted cross sections of a few tens of μbarn [Kar16, Szi20, ZOIG06, ZG13] and to investigate the possibility of producing as well as identifying these difficult to access nuclei. The reaction products were measured in the VAMOS++ magnetic spectrometer for the atomic mass identification while the coincident photons were detected in the AGATA γ-ray spectrometer and the ID-Fix x-ray detector array for the identification of the atomic number through x-ray spectroscopy.

For the efficient x-ray spectroscopy, a preparation work was carried out optimizing the use of the ID-Fix array, in terms of the required pulse processing parameters and photon absorber thicknesses, under experimental conditions of high count rate of photons stemming from the ^{238}U + ^{238}U reaction. From the source test, it was concluded that the risetime of 5 μs is an optimum value for the trapezoidal filter of the employed NUMEXO2 digital electronics used for the pulse processing, allowing to keep a reasonable resolving power of around 1 keV (FWHM) and an efficiency of around 50% at 30 kHz of count rate. It was observed that, at the same rate, other parameters such as the flat top, the average energy window and the computing delay influence less the detectors response within $\pm$0.2 keV (FWHM) in resolution and $\pm$5% in efficiency. The same configuration was chosen for the AGATA signal processing. From the in-beam test using the ^{238}U + ^{238}U reaction at 3.8 MeV/A, it was concluded that to sufficiently reduce the amount of photons and to keep the energy threshold as low as possible an absorber of aluminum with a thickness of 1.5 mm is required for the LEPS detectors. In the actual experiment, this thickness was used in the beginning, but later a 0.5 mm titanium absorber was placed additionally as the

count rate at nominal beam energies and at the experimental conditions with the actual (new) VAMOS target chamber was higher than the expected one.

The experiment was performed at two beam energies of 7.193 and 6.765 MeV/A. It suffered from various technical issues on the accelerator side. Nevertheless, it was possible to accumulate around 19% of the requested beam dose on target and collect the data with the unique combination of VAMOS + AGATA + ID-Fix. The most time-consuming part of the thesis work was the calibration of the VAMOS++ detectors due to two main reasons.

i) The focal plane MWPPAC detectors were newly installed. To reconstruct the A/q of the reaction products, the position of these detectors had to be properly set in the VAMOS++ frame, in which the trajectory simulation is performed. The proper position finding requires a scrupulous scanning in horizontal coordinate and in the coordinate along the central trajectory of VAMOS++ for both MWPPAC detectors as well as the scanning in time offsets.

ii) The calibration of the newly configurated IC detector was performed using directly the ^{238}U + ^{238}U reaction data. The uranium-like products lose around 30 to 70% of energy, depending on the scattering angle, in the different layers of the material prior to the IC detector making it challenging to determine the total energy of the products which is required for the atomic mass identification.

Despite the abovementioned issues, the A/q and the masses of the fission fragments as well as the uranium-like products were reconstructed. Moreover, information on the velocity, accounting for the energy lost in the aluminum degrader and the various detector materials, and the scattering angles of the reaction products was obtained. Using this information, it was possible to perform the Doppler correction (DC) for the energies of the coincident photons detected in AGATA and ID-Fix. In the Doppler corrected ID-Fix and AGATA spectra, the characteristic x-rays and the γ-rays of the rotational band of ^{238}U recoils was clearly seen. Without the DC, the photons, from the reaction partner measured with VAMOS++, detected with ID-Fix were not subject to Doppler shift of the peak energy as ID-Fix were mounted under $\sim$90 degrees to the central trajectory of VAMOS++. The same is true for AGATA but for the photons emitted from the respective partner instead. In the both spectra, the x-rays and γ-rays contributing from both partners are overlapping making it challenging to disentangle them.

Although the post-experiment measurement of the decay of long-lived products confirmed that the strongest ($\pm$1n) transfer channels were populated in the present experiment, the obtained limit cross sections of 11(4) and 5(2) μbarn were not sufficient to observe the products of the different transfer channels in the VAMOS + AGATA (+ID-Fix) coincidence spectra. This suggests that the values predicted for the transfer of $\pm$5 uranium-like nucleons overestimate the required cross sections. The measured (quasi-)elastic angular distribution at two beam energies confirms that the grazing angle for the ^{238}U + ^{238}U reaction is 40° as predicted by the GRAZING model.

In future, another attempt to investigate the production cross sections of the MNT reactions in ^{238}U + ^{238}U can be pursued, accumulating the minimum beam dose of 1.89×10^{15} assumed in the experiment proposal, which was not our case, to make the measurement ±5 uranium-like nucleon transfer possible, at VAMOS++ plus an alternative γ-ray detection setup or at the PRISMA magnetic spectrometer [SCM+02] at LNL combined with AGATA and ID-Fix.

Appendix A

Complements to the ID-Fix tests

The complete details of the in-beam test was provided in Section 4.2. The calibration of the silicon detector with the 3-line α source is given in the following section.

A.1 Silicon detector calibration

The 3-line α source emits α particles of ^{239}Pu, ^{241}Am and ^{244}Cm with energies and intensities given in Table A.1. The energies of the most intense α lines were associated to the mean of the three peaks extracted from the non-calibrated α spectra. The result of a linear fit obtained with a first-order polynomial is shown in Figure A.2. Figure A.1 shows the spectra before and after the calibration procedure with the 3-line α source. The resolution of the detector, was not of high importance and therefore was not optimized for α spectroscopy, is found to be $\sim$190 keV (FWHM) with 4% error bars in an energy range from 5.1 MeV to 5.8 MeV (see Table A.1).

Table A.1: Energies of the α decays of the 3-line α source obtained after the calibration of the silicon detector at 21.5°. The values of the FWHM as well as the literature energy and intensity values for the corresponding transitions are given.

Radionuclide	This work		Ref. [Ziea]	
	E_α (keV)	FWHM (keV)	E_α (keV)	Intensity (%)
^{239}Pu	5147(2)	188	5105	11.5
			5143	15.1
			5155	**73.4**
^{241}Am	5480(3)	192	5388	1.4
			5443	12.8
			5486	**85.2**
^{244}Cm	5791(3)	189	5763	23.3
			5805	**76.7**

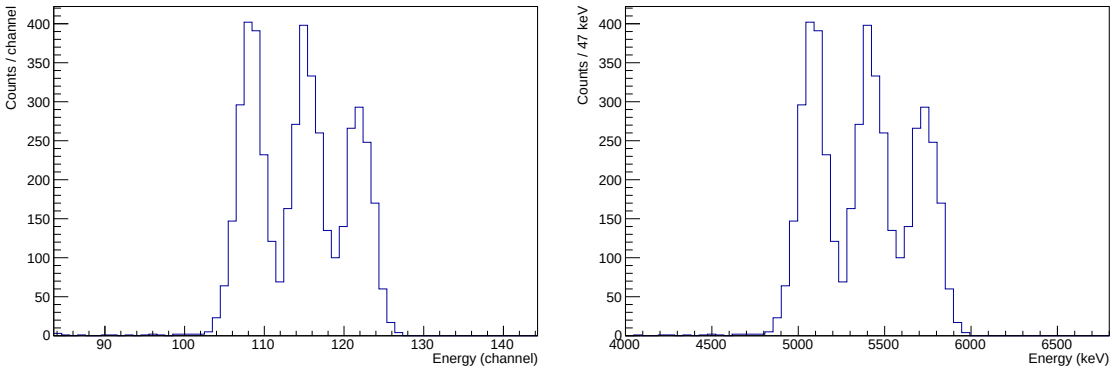

Figure A.1: 3-line α spectra before (left) and after (right) the calibration procedure of the silicon detector at 21.5°.

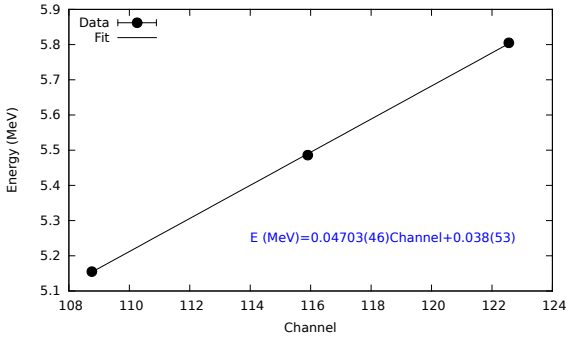

Figure A.2: Energy-to-channel calibration curve of the silicon detector at 21.5° with the 3-line α source. The statistical errors are smaller than the symbol size.

Bibliography

[AAA+12] S. Akkoyun, A. Algora, B. Alikhani, F. Ameil, et al. Agata—advanced gamma tracking array. *Nuclear Instruments and Methods in Physics Research Section A: Accelerators, Spectrometers, Detectors and Associated Equipment*, 668:26–58, 2012.

[ABB+08] F. Azaiez, D. Beaumel, B. Blank, W. Catford, F. Chautard, S. Galeás, G. Gaubert, et al. GANIL / SPIRAL - 2001-2007 - Achievements, Highlights and Perspectives. *in2p3-00336915*, 2008.

[ABC+21] D. Ackermann, B. Blank, L. Caceres, M. Caamaño, G. De France, B. Gall, S. Grévy, C. Grygiel, E. Lamour, X. Ledoux, V. Manea, Ch. Peaucelle, J. Rangama, N. Redon, I. Stefan, Ch. Stodel, B. Sulignano, and Ch. Theisen. NEWGAIN White Book - Science Requirements - Work Package Physics. Technical report, GANIL - document link: https://www.ganil-spiral2.eu/scientists/ganil-spiral-2-facilities/accelerators/newgain/, June 2021.

[ACL+21] M. Assié, E. Clément, A. Lemasson, D. Ramos, A. Raggio, I. Zanon, F. Galtarossa, C. Lenain, J. Casal, F. Flavigny, A. Matta, D. Mengoni, D. Beaumel, Y. Blumenfeld, R. Borcea, D. Brugnara, W. Catford, F. de Oliveira, F. Delaunay, N. De Séréville, F. Didierjean, C.Aa. Diget, J. Dudouet, B. Fernández-Domínguez, C. Fougères, G. Frémont, V. Girard-Alcindor, A. Giret, A. Goasduff, A. Gottardo, J. Goupil, F. Hammache, P.R. John, A. Korichi, L. Lalanne, S. Leblond, A. Lefevre, F. Legruel, L. Ménager, B. Million, C. Nicolle, F. Noury, E. Rauly, K. Rezynkina, E. Rindel, J.S. Rojo, M. Siciliano, M. Stanoiu, I. Stefan, and L. Vatrinet. Oct 2021.

[Afa14] A V Afanasjev. Microscopic description of rotation: from ground states to the extremes of ultra-high spin. *Physica Scripta*, 89(5):054001, apr 2014.

[AT17] D. Ackermann and Ch. Theisen. Nuclear structure features of very heavy and superheavy nuclei—tracing quantum mechanics towards the ‘ island of stability ’. *Physica Scripta*, 92:083002, 08 2017.

[ATK+16] M. Asai, K. Tsukada, Y. Kasamatsu, Y. Ishii, A. Toyoshima, T.K. Sato, Y. Nagame, I. Nishinaka, H. Haba, and T. Ishii. Measurement of the first excited 2^+ state in ^{252}fm. *JAEA-Review*, 025:9, 10 2016.

[Bas80] R. Bass. *Nuclear reactions with heavy ions*. Berlin, Heidelberg, New York, Springer-Verlag, 1980.

[BBC+13] M Bellato, D Bortolato, J Chavas, R Isocrate, G Rampazzo, A Triossi, D Bazzacco, D Mengoni, and F Recchia. Sub-nanosecond clock synchronization and trigger management in the nuclear physics experiment AGATA. *Journal of Instrumentation*, 8(07):P07003–P07003, jul 2013.

[BFD+98] L. Bex, J. L. Flambard, M. Dupuis, P. Lehérissier, and J. P. Rataud. Production of metallic ions with an ecris at ganil. *Review of Scientific Instruments*, 69(2):792–794, 1998.

[BH13] Michael Bender and Paul-Henri Heenen. Structure of superheavy nuclei. *Journal of Physics: Conference Series*, 420(1):012002, mar 2013.

[BHR03] Michael Bender, Paul-Henri Heenen, and Paul-Gerhard Reinhard. Self-consistent mean-field models for nuclear structure. *Rev. Mod. Phys.*, 75:121–180, Jan 2003.

[Bla10] Bas Blank. The desir facility at spiral2. *Pramana*, 75:343–353, 08 2010.

[BNR01] M. Bender, W. Nazarewicz, and P.-G. Reinhard. Shell stabilization of super- and hyperheavy nuclei without magic gaps. *Physics Letters B*, 515(1-2):42–48, aug 2001.

[Bou] A. Boujrad. Retour d'Expériences au GANIL, [Online]. Available: https://docplayer.fr/10362225-Retour-d-experiences-au-ganil.html.

[BR25] Patrick Maynard Stuart Blackett and Ernest Rutherford. The ejection of protons from nitrogen nuclei, photographed by the wilson method. *Proceedings of the Royal Society of London. Series A, Containing Papers of a Mathematical and Physical Character*, 107(742):349–360, 1925.

[BS00] A. Boujrad and F. Saillant. The new ganil data acquisition system. In *2000 IEEE Nuclear Science Symposium. Conference Record (Cat. No.00CH37149)*, volume 2, pages 12/192–12/193 vol.2, 2000.

[BVG+15] B. Birkenbach, A. Vogt, K. Geibel, F. Recchia, P. Reiter, J. J. Valiente-Dobón, D. Bazzacco, M. Bowry, A. Bracco, B. Bruyneel, L. Corradi, F. C. L. Crespi, G. de Angelis, P. Désesquelles, J. Eberth, E. Farnea, E. Fioretto, A. Gadea, A. Gengelbach, A. Giaz, A. Görgen, A. Gottardo, J. Grebosz, H. Hess, P. R. John, J. Jolie, D. S. Judson, A. Jungclaus, W. Korten, S. Lenzi, S. Leoni, S. Lunardi, R. Menegazzo, D. Mengoni, C. Michelagnoli, T. Mijatović, G. Montagnoli, D. Montanari, D. Napoli, L. Pellegri,

G. Pollarolo, A. Pullia, B. Quintana, F. Radeck, D. Rosso, E. Şahin, M. D. Salsac, F. Scarlassara, P.-A. Söderström, A. M. Stefanini, T. Steinbach, O. Stezowski, S. Szilner, B. Szpak, Ch. Theisen, C. Ur, V. Vandone, and A. Wiens. Spectroscopy of the neutron-rich actinide nucleus ^{240}U following multinucleon-transfer reactions. *Phys. Rev. C*, 92:044319, Oct 2015.

[BWW08] K. Bethge, G. Walter, and B. Wiedemann. *Kernphysik: eine Einführung*. Springer-Verlag, 2008.

[Cle21] E. Clement. Private Communication, 2021.

[CLL+05] Catford, W. N., Lemmon, R. C., Labiche, M., Timis, C. N., Orr, N. A., Caballero, L., Chapman, R., Chartier, M., Rejmund, M., Savajols, H., and the TIARA Collaboration. First experiments on transfer with radioactive beams using the tiara array. *Eur. Phys. J. A*, 25:245–250, 2005.

[CLR02] GREGORY R. CHOPPIN, JAN-OLOV LILJENZIN, and JAN RYDBERG. Chapter 11 - nuclear structure. In GREGORY R. CHOPPIN, JAN-OLOV LILJENZIN, and JAN RYDBERG, editors, *Radiochemistry and Nuclear Chemistry (Third Edition)*, pages 299–333. Butterworth-Heinemann, Woburn, third edition edition, 2002.

[CMd+17] E. Clément, C. Michelagnoli, G. de France, H.J. Li, A. Lemasson, C. Barthe Dejean, M. Beuzard, P. Bougault, J. Cacitti, J.-L. Foucher, G. Fremont, P. Gangnant, J. Goupil, C. Houarner, M. Jean, A. Lefevre, L. Legeard, F. Legruel, C. Maugeais, L. Ménager, N. Ménard, H. Munoz, M. Ozille, B. Raine, J.A. Ropert, F. Saillant, C. Spitaels, M. Tripon, Ph. Vallerand, G. Voltolini, W. Korten, M.-D. Salsac, Ch. Theisen, M. Zielińska, T. Joannem, M. Karolak, M. Kebbiri, A. Lotode, R. Touzery, Ch. Walter, A. Korichi, J. Ljungvall, A. Lopez-Martens, D. Ralet, N. Dosme, X. Grave, N. Karkour, X. Lafay, E. Legay, I. Kojouharov, C. Domingo-Pardo, A. Gadea, R.M. Pérez-Vidal, J.V. Civera, B. Birkenbach, J. Eberth, H. Hess, L. Lewandowski, P. Reiter, A. Nannini, G. De Angelis, G. Jaworski, P. John, D.R. Napoli, J.J. Valiente-Dobón, D. Barrientos, D. Bortolato, G. Benzoni, A. Bracco, S. Brambilla, F. Camera, F.C.L. Crespi, S. Leoni, B. Million, A. Pullia, O. Wieland, D. Bazzacco, S.M. Lenzi, S. Lunardi, R. Menegazzo, D. Mengoni, F. Recchia, M. Bellato, R. Isocrate, F.J. Egea Canet, F. Didierjean, G. Duchêne, R. Baumann, M. Brucker, E. Dangelser, M. Filliger, H. Friedmann, G. Gaudiot, J.-N. Grapton, H. Kocher, C. Mathieu, M.-H. Sigward, D. Thomas, S. Veeramootoo, J. Dudouet, O. Stézowski, C. Aufranc, Y. Aubert, M. Labiche, J. Simpson, I. Burrows, P.J. Coleman-Smith, A. Grant, I.H. Lazarus, P.S. Morrall, V.F.E. Pucknell, A. Boston, D.S. Judson, N. Lalović, J. Nyberg, J. Collado, V. González, I. Kuti, B.M. Nyakó, A. Maj, and M. Rudigier. Conceptual design of the agata 1π array at ganil. *Nuclear Instruments and Methods in Physics Research Section A: Accelerators, Spectrometers, Detectors and Associated Equipment*, 855:1–12, 2017.

[CPS09] L. Corradi, G. Pollarolo, and S. Szilner. Multinucleon transfer processes in heavy-ion reactions. *Journal of Physics G: Nuclear and Particle Physics*, 36:113101–113143, 2009.

[CTL+03] W. N. Catford, C. N. Timis, M. Labiche, R. C. Lemmon, G. Moores, and R. Chapman. The TIARA Array for the Study of Nucleon Transfer Reactions. In *AIP Conference Proceedings*, volume 680, page 329, 2003.

[DDE+86] J.P. Dufour, R. Del Moral, H. Emmermann, F. Hubert, D. Jean, C. Poinot, M.S. Pravikoff, A. Fleury, H. Delagrange, and K.-H. Schmidt. Projectile fragments isotopic separation: Application to the lise spectrometer at ganil. *Nuclear Instruments and Methods in Physics Research Section A: Accelerators, Spectrometers, Detectors and Associated Equipment*, 248(2):267–281, 1986.

[DU19] K.. Diaz and A. Utepov. Test and Characterisation of an α-X-ray detection set-up. Master Degree Internship Report, University of Caen-Normandie, 2019.

[ECGT+15] F. J. Egea Canet, V. González, M. Tripon, M. Jastrząb, A. Triossi, A. Gadea, G. de France, J. J. Valiente-Dobón, D. Barrientos, E. Sanchis, A. Boujrad, C. Houarner, M. Blaizot, P. Bourgault, G. de Angelis, M. N. Erduran, S. Ertürk, T. Hüyük, G. Jaworski, X. L. Luo, V. Modamio, M. Moszyński, A. Di Nitto, J. Nyberg, P.-A. Söderström, M. Palacz, and R. Wadsworth. A new front-end high-resolution sampling board for the new-generation electronics of exogam2 and neda detectors. *IEEE Transactions on Nuclear Science*, 62(3):1056–1062, 2015.

[ECHB+15] F. J. Egea Canet, C. Houarner, A. Boujrad, V. González, M. Tripon, M. Jastrząb, A. Triossi, G. de France, A. Gadea, J. J. Valiente-Dobón, D. Barrientos, E. Sanchis, M. Blaizot, P. Bourgault, G. de Angelis, M. N. Erduran, S. Ertürk, T. Hüyük, G. Jaworski, X. L. Luo, V. Modamio, M. Moszyński, A. Di Nitto, J. Nyberg, P-A. Söderström, M. Palacz, and R. Wadsworth. Digital front-end electronics for the neutron detector neda. *IEEE Transactions on Nuclear Science*, 62(3):1063–1069, 2015.

[FAC+19] M.O. Fregeau, D. Ackermann, L. Caceres, K.V. Diaz Hernandez, and A. Utepov. Report on R&D on studies on X-ray emission and detector material. Report id: 15.7, ENSAR2 654002, 2019.

[FJM+12] M. O. Frégeau, D. Jacquet, M. Morjean, E. Bonnet, A. Chbihi, J. D. Frankland, M. F. Rivet, L. Tassan-Got, F. Dechery, A. Drouart, L. Nalpas, X. Ledoux, M. Parlog, C. Ciortea, D. Dumitriu, D. Fluerasu, M. Gugiu, F. Gramegna, V. L. Kravchuk, T. Marchi, D. Fabris, A. Corsi, and S. Barlini. X-ray fluorescence from the element with atomic number $z = 120$. *Phys. Rev. Lett.*, 108:122701, Mar 2012.

[F.R19] Professor Sir E. Rutherford F.R.S. Liv. collision of α particles with light atoms. iv. an anomalous effect in nitrogen. *The London, Edinburgh, and Dublin Philosophical Magazine and Journal of Science*, 37(222):581–587, 1919.

[Fre11] M.O. Fregeau. *Fluorescence X appliquèe à l'ètude du temps de fission de l'element Z=120*. PhD thesis, Universitè de Caen Basse-Normandie, 2011.

[Gam30] G. Gamow. Mass Defect Curve and Nuclear Constitution. *Proceedings of the Royal Society of London Series A*, 126(803):632–644, March 1930.

[GANa] GANIL. AGATA at GANIL : seven years of success-story. https://www.ganil-spiral2.eu/2021/09/13/agata/.

[GANb] GANIL. Available beams at GANIL. https://u.ganil-spiral2.eu/chartbeams/.

[GANc] GANIL. GANIL/SPIRAL2 News. https://www.ganil-spiral2.eu/2021/12/19/spiral2-linac-nfs-is-now-fully-operational/.

[GCC+05] X. Grave, R. Canedo, J.-F. Clavelin, S. Du, and E. Legay. Narval a modular distributed data acquisition system with ada 95 and rtai. In *14th IEEE-NPSS Real Time Conference, 2005.*, pages 5 pp.–, 2005.

[GFVD+11] A. Gadea, E. Farnea, J.J. Valiente-Dobón, B. Million, D. Mengoni, D. Bazzacco, F. Recchia, A. Dewald, Th. Pissulla, W. Rother, G. de Angelis, A. Austin, S. Aydin, S. Badoer, M. Bellato, G. Benzoni, L. Berti, R. Beunard, B. Birkenbach, E. Bissiato, N. Blasi, C. Boiano, D. Bortolato, A. Bracco, S. Brambilla, B. Bruyneel, E. Calore, F. Camera, A. Capsoni, J. Chavas, P. Cocconi, S. Coelli, A. Colombo, D. Conventi, L. Costa, L. Corradi, A. Corsi, A. Cortesi, F.C.L. Crespi, N. Dosme, J. Eberth, S. Fantinel, C. Fanin, E. Fioretto, Ch. Fransen, A. Giaz, A. Gottardo, X. Grave, J. Grebosz, R. Griffiths, E. Grodner, M. Gulmini, T. Habermann, C. He, H. Hess, R. Isocrate, J. Jolie, P. Jones, A. Latina, E. Legay, S. Lenzi, S. Leoni, F. Lelli, D. Lersch, S. Lunardi, G. Maron, R. Menegazzo, C. Michelagnoli, P. Molini, G. Montagnoli, D. Montanari, O. Möller, D.R. Napoli, M. Nicoletto, R. Nicolini, M. Ozille, G. Pascovici, R. Peghin, M. Pignanelli, V. Pucknell, A. Pullia, L. Ramina, G. Rampazzo, M. Rebeschini, P. Reiter, S. Riboldi, M. Rigato, C. Rossi Alvarez, D. Rosso, G. Salvato, J. Strachan, E. Sahin, F. Scarlassara, J. Simpson, A.M. Stefanini, O. Stezowski, F. Tomasi, N. Toniolo, A. Triossi, M. Turcato, C.A. Ur, V. Vandone, R. Venturelli, F. Veronese, C. Veyssiere, E. Viscione, O. Wieland, A. Wiens, F. Zocca, and A. Zucchiatti. Conceptual design and infrastructure for the installation of the first agata sub-array at lnl. *Nuclear Instruments and Methods in Physics Research Section A: Accelerators, Spectrometers, Detectors and Associated Equipment*, 654(1):88–96, 2011.

[GHM+10] C. Golabek, S. Heinz, Wolfgang Mittig, F. Rejmund, A. Villari, S. Bhattacharyva, D. Boilley, Gilles de France, A. Drouart, L. Gaudefroy, Giot Lydie, and V. Maslov.

Investigation of deep inelastic reactions in ^{238}U+^{238}U at coulomb barrier energies. *European Physical Journal A*, 43:251–259, 03 2010.

[Gol06] C. Golabek. *A la recherche d'une signature de la formation et décroissance du système gèant "Z=184"*. PhD thesis, Universitè de Caen Basse-Normandie, 2006.

[HJS49] Otto Haxel, J. Hans D. Jensen, and Hans E. Suess. On the "magic numbers" in nuclear structure. *Phys. Rev.*, 75:1766–1766, Jun 1949.

[IMA+07] T. Ishii, H. Makii, M. Asai, H. Koura, S. Shigematsu, K. Tsukada, A. Toyoshima, M. Matsuda, A. Makishima, J. Kaneko, H. Toume, I. Hossain, T. Shizuma, S. Ichikawa, T. Kohno, and M. Ogawa. Ground-state bands of neutron-rich ^{236}Th and ^{242}U nuclei and implication of spherical shell closure at $n = 164$. *Phys. Rev. C*, 76:011303, Jul 2007.

[IN2] IN2P3. GANIL Chronology. https://50ans.in2p3.fr/timeline-ganil/.

[JK94] Valentin T. Jordanov and Glenn F. Knoll. Digital synthesis of pulse shapes in real time for high resolution radiation spectroscopy. *Nuclear Instruments and Methods in Physics Research Section A: Accelerators, Spectrometers, Detectors and Associated Equipment*, 345(2):337–345, 1994.

[Joh15] Philipp Rudolf John. *Study of shape evolution in the neutron-rich osmium isotopes with the advanced gamma-tracking array AGATA*. PhD thesis, Università di Padova, 2015.

[KAB+20] W. Korten, A. Atac, D. Beaumel, F. Ameil, et al. Physics opportunities with the Advanced Gamma Tracking Array: AGATA. *The European Physical Journal A*, 56:137, 2020.

[KAH+08] Birgit Kindler, Dieter Ackermann, Willi Hartmann, Fritz Peter Heßberger, Sigurd Hofmann, Annett Hübner, Bettina Lommel, Rido Mann, and Jutta Steiner. Uranium fluoride and metallic uranium as target materials for heavy-element experiments at ship. *Nuclear Instruments and Methods in Physics Research Section A: Accelerators, Spectrometers, Detectors and Associated Equipment*, 590(1):126–130, 2008. Toward the Realization of Target and Stripper Foil Technologies for High-Power Proton and Radioactive Ion Accelerators.

[Kar16] A. Karpov. Private Communication, 2016.

[KCS16] O. Kamalou, F. Chautard, and A. Savalle. Stable and exotic beams produced at ganil. *Proceedings of Cyclotrons2016*, 2016.

[KL19] Korichi, A. and Lauritsen, T. Tracking γ rays in highly segmented hpge detectors: A review of agata and gretina. *Eur. Phys. J. A*, 55(7):121, 2019.

[KLR+17] Y. H. Kim, A. Lemasson, M. Rejmund, A. Navin, S. Biswas, C. Michelagnoli, I. Stefan, R. Banik, P. Bednarczyk, S. Bhattacharya, S. Bhattacharyya, E. Clément, H. L. Crawford, G. De France, P. Fallon, J. Goupil, B. Jacquot, H. J. Li, J. Ljungvall, A. O. Macchiavelli, A. Maj, L. Ménager, V. Morel, R. Palit, R. M. Pérez-Vidal, J. Ropert, and C. Schmitt. Prompt-delayed γ -ray spectroscopy with agata, exogam and vamos++. *The European Physical Journal A*, 53(8):1–8, 8 2017. Communicated by A. Gade.

[Kno79] G. F. Knoll. *Radiation detection and measurement*, volume 1. New York, John Wiley and Sons, Inc., 1979.

[KSG13] J. V. Kratz, M. Schädel, and H. W. Gäggeler. Reexamining the heavy-ion reactions ^{238}u+^{238}u and ^{238}u+^{248}cm and actinide production close to the barrier. *Phys. Rev. C*, 88:054615, Nov 2013.

[LAA+17] X Ledoux, M Aïche, M. Avrigeanu, Vlad Avrigeanu, Emmanuel Balanzat, B Ban-d'Etat, G. Ban, E Bauge, G Bélier, Pavel Bem, Catalin Borcea, Tiphaine Caillaud, A Chatillon, S Czajkowski, P Dessagne, D Doré, U Fischer, M Frégeau, J Grinyer, and C Varignon. The Neutrons for Science Facility at SPIRAL-2. *Radiation protection dosimetry*, 180:1–5, 11 2017.

[LBC+04] P. Leherissier, C. Barue, C. Canet, M. Dubois, M. Dupuis, J. L. Flambard, G. Gaubert, P. Jardin, N. Lecesne, F. Lemagnen, R. Leroy, J.Y. Pacquet, and F. Pellemoine-Landre. Status report on ECR ion source operation at GANIL. *Review of Scientific Instruments*, 75(5):1488–1491, 2004.

[LCH+20] Lommel, Bettina, Celik Ayik, Elif, Hübner, Annett, Kindler, Birgit, Steiner, Jutta, and Yakusheva, Vera. Uranium targets for heavy-ion accelerators. *EPJ Web Conf.*, 229:03006, 2020.

[LCL+10] M. Labiche, W.N. Catford, R.C. Lemmon, C.N. Timis, R. Chapman, N.A. Orr, B. Fernández-Domínguez, G. Moores, N.L. Achouri, N. Amzal, S. Appleton, N.I. Ashwood, T.D. Baldwin, M. Burns, L. Caballero, J. Cacitti, J.M. Casadjian, M. Chartier, N. Curtis, K. Faiz, G. de France, M. Freer, J.M. Gautier, W. Gelletly, G. Iltis, B. Lecornu, X. Liang, C. Marry, Y. Merrer, L. Olivier, S.D. Pain, V.F.E. Pucknell, B. Raine, M. Rejmund, B. Rubio, F. Saillant, H. Savajols, O. Sorlin, K. Spohr, Ch. Theisen, G. Voltolini, and D.D. Warner. TIARA: A large solid angle silicon array for direct reaction studies with radioactive beams. *Nuclear Instruments and Methods in Physics Research Section A: Accelerators, Spectrometers, Detectors and Associated Equipment*, 614(3):439–448, 2010.

[LMHK+04] A. Lopez-Martens, K. Hauschild, A. Korichi, J. Roccaz, and J-P. Thibaud. γ-ray tracking algorithms: a comparison. *Nuclear Instruments and Methods in Physics Research Section A: Accelerators, Spectrometers, Detectors and Associated Equipment*, 533(3):454–466, 2004.

[LP95] Kwong Lau and Jörg Pyrlik. Optimization of centroid-finding algorithms for cathode strip chambers. *Nuclear Instruments and Methods in Physics Research Section A: Accelerators, Spectrometers, Detectors and Associated Equipment*, 366(2):298–309, 1995.

[LQB+85] M. Langevin, E. Quiniou, M. Bernas, J. Galin, J.C. Jacmart, F. Naulin, F. Pougheon, R. Anne, C. Détraz, D. Guerreau, D. Guillemaud-Mueller, and A.C. Mueller. Production of neutron-rich nuclei at the limits of particles stability by fragmentation of 44 mevu 40ar projectiles. *Physics Letters B*, 150(1):71–74, 1985.

[M.A13] H.G.J. Moseley M.A. Xciii. the high-frequency spectra of the elements. *The London, Edinburgh, and Dublin Philosophical Magazine and Journal of Science*, 26(156):1024–1034, 1913.

[M.A14] H.G.J. Moseley M.A. Lxxx. the high-frequency spectra of the elements. part ii. *The London, Edinburgh, and Dublin Philosophical Magazine and Journal of Science*, 27(160):703–713, 1914.

[May49] Maria Goeppert Mayer. On closed shells in nuclei. ii. *Phys. Rev.*, 75:1969–1970, Jun 1949.

[May50] Maria Goeppert Mayer. Nuclear configurations in the spin-orbit coupling model. i. empirical evidence. *Phys. Rev.*, 78:16–21, Apr 1950.

[MHS+17] M. Morjean, D. J. Hinde, C. Simenel, D. Y. Jeung, M. Airiau, K. J. Cook, M. Dasgupta, A. Drouart, D. Jacquet, S. Kalkal, C. S. Palshetkar, E. Prasad, D. Rafferty, E. C. Simpson, L. Tassan-Got, K. Vo-Phuoc, and E. Williams. Evidence for the role of proton shell closure in quasifission reactions from x-ray fluorescence of mass-identified fragments. *Phys. Rev. Lett.*, 119:222502, Nov 2017.

[MIA+07] H. Makii, T. Ishii, M. Asai, K. Tsukada, A. Toyoshima, M. Matsuda, A. Makishima, J. Kaneko, H. Toume, S. Ichikawa, S. Shigematsu, T. Kohno, and M. Ogawa. z dependence of the $n = 152$ deformed shell gap: In-beam γ-ray spectroscopy of neutron-rich $^{245,246}\mathrm{Pu}$. *Phys. Rev. C*, 76:061301, Dec 2007.

[Mij22] Tea Mijatović. Multinucleon transfer reactions: a mini-review of recent advances. *Frontiers in Physics*, 10, 2022.

[MSIS16] P. Möller, A.J. Sierk, T. Ichikawa, and H. Sagawa. Nuclear ground-state masses and deformations: Frdm(2012). *Atomic Data and Nuclear Data Tables*, 109-110:1–204, 2016.

[Mé99] François Méot. The ray-tracing code zgoubi. *Nuclear Instruments and Methods in Physics Research Section A: Accelerators, Spectrometers, Detectors and Associated Equipment*, 427(1):353–356, 1999.

[Nil55] S. G. Nilsson. Binding states of individual nucleons in strongly deformed nuclei. *Kong. Dan. Vid. Sel. Mat. Fys. Med.*, 29N16:1–69, 1955.

[nis] National Institute of Standards and Technology. http://physics.nist.gov.

[nnd] National Nuclear Data Center at Brookhaven National Laboratory. https://www.nndc.bnl.gov/nudat2//.

[PCJ+08] Sugathan Pullanhiotan, A. Chatterjee, B. Jacquot, A. Navin, and Maurycy Rejmund. Improvement in the reconstruction method for vamos spectrometer. *Nuclear Instruments and Methods in Physics Research Section B: Beam Interactions with Materials and Atoms*, 266:4148–4152, 10 2008.

[Pet11] E. Petit. Progress of the SPIRAL2 Project. Proceedings of IPAC2011, San Sebastian, Spain, 2011.

[PPA+20] Vincenzo Patera, Yolanda Prezado, Faical Azaiez, Giuseppe Battistoni, Diego Bettoni, Sytze Brandenburg, Aleksandr Bugay, Giacomo Cuttone, Denis Dauvergne, Gilles France, Christian Graeff, Thomas Haberer, Taku Inaniwa, Sebastien Incerti, Elena Nasonova, Alahari Navin, Marco Pullia, Sandro Rossi, Charlot Vandevoorde, and Marco Durante. Biomedical research programs at present and future high-energy particle accelerators. *Frontiers in Physics*, 8, 10 2020.

[PRN+08] Sugathan Pullanhiotan, Maurycy Rejmund, Alahari Navin, Wolfgang Mittig, and Swarnapratim Bhattacharyya. Performance of vamos for reactions near the coulomb barrier. *Nuclear Instruments & Methods in Physics Research Section A-accelerators Spectrometers Detectors and Associated Equipment*, 593:343–352, 2008.

[PSAS89] Zygmunt Patyk, Adam Sobiczewski, Peter Armbruster, and Karl-Heinz Schmidt. Shell effects in the properties of the heaviest nuclei. *Nuclear Physics A*, 491(2):267–280, 1989.

[PV19] R. M. Perez Vidal. *Collectivity along N = 50: Nuclear Structure studies on the newutron-magic nuclei ^{92}Mo and ^{94}Ru with AGATA and VAMOS++*. PhD thesis, University of Valencia, October 2019.

[Ram16] D. Ramos. *Fragment Distributions of Transfer- and Fusion-Induced Fission from 238U+12C Reactions Measured Through Inverse Kinematics*. PhD thesis, Universidad de Santiago de Compostela, 2016.

[RCG+19] D. Ralet, E. Clément, G. Georgiev, A.E. Stuchbery, M. Rejmund, P. Van Isacker, G. de France, A. Lemasson, J. Ljungvall, C. Michelagnoli, A. Navin, D.L. Balabanski, L. Atanasova, A. Blazhev, G. Bocchi, R. Carroll, J. Dudouet, E. Dupont, B. Fornal, S. Franchoo, C. Fransen, C. Müller-Gatermann, A. Goasduff, A. Gadea,

P.R. John, D. Kocheva, T. Konstantinopoulos, A. Korichi, A. Kusoglu, S.M. Lenzi, S. Leoni, R. Lozeva, A. Maj, R. Perez, N. Pietralla, C. Shand, O. Stezowski, D. Wilmsen, D. Yordanov, D. Barrientos, P. Bednarczyk, B. Birkenbach, A.J. Boston, H.C. Boston, I. Burrows, B. Cederwall, M. Ciemala, J. Collado, F. Crespi, D. Cullen, H.J. Eberth, J. Goupil, L. Harkness, H. Hess, A. Jungclaus, W. Korten, M. Labiche, R. Menegazzo, D. Mengoni, B. Million, J. Nyberg, Zs. Podolyák, A. Pullia, B. Quintana Arnés, F. Recchia, P. Reiter, F. Saillant, M.D. Salsac, E. Sanchis, C. Theisen, J.J. Valiente Dobon, and O. Wieland. Evidence of octupole-phonons at high spin in 207pb. *Physics Letters B*, 797:134797, 2019.

[RCnF+18] D. Ramos, M. Caamaño, F. Farget, C. Rodríguez-Tajes, L. Audouin, J. Benlliure, E. Casarejos, E. Clement, D. Cortina, O. Delaune, X. Derkx, A. Dijon, D. Doré, B. Fernández-Domínguez, G. de France, A. Heinz, B. Jacquot, A. Navin, C. Paradela, M. Rejmund, T. Roger, M.-D. Salsac, and C. Schmitt. Isotopic fission-fragment distributions of ^{238}U,^{239}Np,^{240}Pu,^{244}Cm, and ^{250}Cf produced through inelastic scattering, transfer, and fusion reactions in inverse kinematics. *Phys. Rev. C*, 97:054612, May 2018.

[RGS+17] D Ralet, G Georgiev, A E Stuchbery, E Clément, A Lemasson, C Michelagnoli, M Rejmund, L Atanasova, D L Balabanski, G Bocchi, R Carroll, A Dewald, J Dudouet, B Fornal, G de France, S Franchoo, C Fransen, C Müller-Gatermann, A Goasduff, A Gadea, B Jacquot, P R John, D Kocheva, T Konstantinopoulos, A Korichi, A Kusoglu, S M Lenzi, S Leoni, J Ljungvall, R Lozeva, A Maj, A Navin, R Perez, N Pietralla, C Shand, O Stezowski, and D Yordanov. Toward lifetime and *g* factor measurements of short-lived states in the vicinity of ^{208}pb. *Physica Scripta*, 92(5):054004, apr 2017.

[RLN+11] M. Rejmund, B. Lecornu, A. Navin, C. Schmitt, S. Damoy, O. Delaune, J.M. Enguerrand, G. Fremont, P. Gangnant, L. Gaudefroy, et al. Performance of the improved larger acceptance spectrometer: VAMOS++. *Nuclear Instruments and Methods in Physics Research Section A: Accelerators, Spectrometers, Detectors and Associated Equipment*, 646(1):184–191, 2011.

[SAA+97] J.N Scheurer, M Aiche, M.M Aleonard, G Barreau, F Bourgine, D Boivin, D Cabaussel, J.F Chemin, T.P Doan, J.P Goudour, M Harston, A Brondi, G La Rana, R Moro, E Vardaci, and D Curien. Improvements in the in-beam γ-ray spectroscopy provided by an ancillary detector coupled to a ge γ-spectrometer: the diamant-eurogam ii example. *Nuclear Instruments and Methods in Physics Research Section A: Accelerators, Spectrometers, Detectors and Associated Equipment*, 385(3):501–510, 1997.

[SAdF+00] John Simpson, F. Azaiez, G. de France, J. Fouan, J. Gerl, R. Julin, Wolfram Korten, P.J. Nolan, Barna Nyakó, G. Sletten, P.M. Walker, and EXOGAM Collaboration. The

exogam array: A radioactive beam gamma-ray spectrometer. *Acta Physica Hungarica A*, 11:159–188, 05 2000.

[Sav99] Hervé Savajols. Vamos: a variable mode high acceptance spectrometer. *Nuclear Physics A*, 654(1, Supplement 1):1027c–1032c, 1999.

[Sav03] H. Savajols. VAMOS: A variable mode high acceptance spectrometer for identifying reaction products induced by SPIRAL beams. *Nuclear Instruments and Methods in Physics Research Section B: Beam Interactions with Materials and Atoms*, 204:146–153, 2003.

[SBB+94] Jean-Claude Santiard, Werner Beusch, Steven Buytaert, Christian Enz, Erik Heijne, P. Jarron, F. Krummenacher, Katrien Marent, and Francois Piuz. Gasplex: a low-noise analog signal processor for readout of gaseous detectors. 06 1994.

[SBG+82] M. Schädel, W. Brüchle, H. Gäggeler, J. V. Kratz, K. Sümmerer, G. Wirth, G. Herrmann, R. Stakemann, G. Tittel, N. Trautmann, J. M. Nitschke, E. K. Hulet, R. W. Lougheed, R. L. Hahn, and R. L. Ferguson. Actinide production in collisions of $^{238}\mathrm{U}$ with $^{248}\mathrm{Cm}$. *Phys. Rev. Lett.*, 48:852–855, Mar 1982.

[SCM+02] A.M. Stefanini, L. Corradi, G. Maron, A. Pisent, M. Trotta, A.M. Vinodkumar, S. Beghini, G. Montagnoli, F. Scarlassara, G.F. Segato, A. De Rosa, G. Inglima, D. Pierroutsakou, M. Romoli, M. Sandoli, G. Pollarolo, and A. Latina. The heavy-ion magnetic spectrometer prisma. *Nuclear Physics A*, 701(1):217–221, 2002. 5th International Conference on Radioactive Nuclear Beams.

[SDD+15] S3 Collaboration, Déchery, F., Drouart, A., Savajols, H., Nolen, J., Authier, M., Amthor, A. M., Boutin, D., Delferriére, O., Gall, B., Hue, A., Laune, B., Le Blanc, F., Manikonda, S., Payet, J., Stodel, M. -H., Traykov, E., and Uriot, D. Toward the drip lines and the superheavy island of stability with the Super Separator Spectrometer S3. *Eur. Phys. J. A*, 51(6):66, 2015.

[SKA+78] M. Schädel, J. V. Kratz, H. Ahrens, W. Brüchle, G. Franz, H. Gäggeler, I. Warnecke, G. Wirth, G. Herrmann, N. Trautmann, and M. Weis. Isotope distributions in the reaction of $^{238}\mathrm{U}$ with $^{238}\mathrm{U}$. *Phys. Rev. Lett.*, 41:469–472, Aug 1978.

[SM01] Jean-Claude Santiard and K Marent. The Gassiplex0.7-2 Integrated Front-End Analog Processor for the HMPID and the Dimuon Spectrometer of ALICE. page 6 p, Oct 2001.

[SMP01] A. Sobiczewski, I. Muntian, and Z. Patyk. Problem of "deformed" superheavy nuclei. *Physical Review C*, 63:034306, Feb 2001.

[SP07] Adam Sobiczewski and Krzysztof Pomorski. Description of structure and properties of superheavy nuclei. *Progress in Particle and Nuclear Physics*, 58(1):292–349, 2007.

[Str67] V.M. Strutinsky. Shell effects in nuclear masses and deformation energies. *Nuclear Physics A*, 95(2):420–442, 1967.

[Szi20] S. Szilner. Private Communication, 2020.

[TB] O. Tarasov and D. Bazin. LISE++. http://lise.nscl.msu.edu/lise.html.

[TGK+15] Ch. Theisen, P.T. Greenlees, T.-L. Khoo, P. Chowdhury, and T. Ishii. In-beam spectroscopy of heavy elements. *Nuclear Physics A*, 944:333–375, 2015. Special Issue on Superheavy Elements.

[Tri] M. Tripon. EXOGAM2 Technical specifications, Jan 2012 [Online]. Available: http://wiki.ganil.fr/gap/GAMMA/attach-ment/wiki/EXOGAM2/Developpement/Hardware/FADC_Mezza-nine/Docs/CdC_technique.pdf.

[UNI] UNICAEN. UNICAEN Research. https://www.unicaen.fr/unicaen-partenaire-de-4-nouveaux-equipex/.

[VALR05] D. Vretenar, A.V. Afanasjev, G.A. Lalazissis, and P. Ring. Relativistic hartree–bogoliubov theory: static and dynamic aspects of exotic nuclear structure. *Physics Reports*, 409(3):101–259, 2005.

[VB04] R. Venturelli and D. Bazzacco. Adaptive Grid Search as Pulse Shape Analysis Algorithm for γ-Tracking and Results. Technical report, Laboratori Nazionali di Legnaro, 2004.

[VBR+15] A. Vogt, B. Birkenbach, P. Reiter, L. Corradi, T. Mijatović, D. Montanari, S. Szilner, D. Bazzacco, M. Bowry, A. Bracco, B. Bruyneel, F. C. L. Crespi, G. de Angelis, P. Désesquelles, J. Eberth, E. Farnea, E. Fioretto, A. Gadea, K. Geibel, A. Gengelbach, A. Giaz, A. Görgen, A. Gottardo, J. Grebosz, H. Hess, P. R. John, J. Jolie, D. S. Judson, A. Jungclaus, W. Korten, S. Leoni, S. Lunardi, R. Menegazzo, D. Mengoni, C. Michelagnoli, G. Montagnoli, D. Napoli, L. Pellegri, G. Pollarolo, A. Pullia, B. Quintana, F. Radeck, F. Recchia, D. Rosso, E. Şahin, M. D. Salsac, F. Scarlassara, P.-A. Söderström, A. M. Stefanini, T. Steinbach, O. Stezowski, B. Szpak, Ch. Theisen, C. Ur, J. J. Valiente-Dobón, V. Vandone, and A. Wiens. Light and heavy transfer products in $^{136}\mathrm{Xe} + ^{238}\mathrm{U}$ multinucleon transfer reactions. *Phys. Rev. C*, 92:024619, Aug 2015.

[VDJG+19] J.J. Valiente-Dobón, G. Jaworski, A. Goasduff, F.J. Egea, V. Modamio, T. Hüyük, A. Triossi, M. Jastrząb, P.A. Söderström, A. Di Nitto, G. de Angelis, G. de France, N. Erduran, A. Gadea, M. Moszyński, J. Nyberg, M. Palacz, R. Wadsworth, R. Aliaga, C. Aufranc, M. Bézard, G. Baulieu, E. Bissiato, A. Boujrad, I. Burrows, S. Carturan, P. Cocconi, G. Colucci, D. Conventi, M. Cordwell, S. Coudert, J.M. Deltoro, L. Ducroux, T. Dupasquier, S. Ertürk, X. Fabian, V. González, A. Grant, K. Hadyńska-Klęk, A. Illana, M.L. Jurado-Gomez, M. Kogimtzis, I. Lazarus, L. Legeard, J. Ljungvall,

G. Pasqualato, R.M. Pérez-Vidal, A. Raggio, D. Ralet, N. Redon, F. Saillant, B. Sayğı, E. Sanchis, M. Scarcioffolo, M. Siciliano, D. Testov, O. Stezowski, M. Tripon, and I. Zanon. Neda—neutron detector array. *Nuclear Instruments and Methods in Physics Research Section A: Accelerators, Spectrometers, Detectors and Associated Equipment*, 927:81–86, 2019.

[VLR+16] M. Vandebrouck, A. Lemasson, M. Rejmund, G. Fremont, J. Pancin, A. Navin, C. Michelagnoli, J. Goupil, C. Spitaels, and B. Jacquot. Dual position sensitive mwpc for tracking reaction products at vamos++. *Nuclear Instruments and Methods in Physics Research Section A: Accelerators, Spectrometers, Detectors and Associated Equipment*, 812:112–117, 2016.

[Wei35] C. F. V. Weizsäcker. Zur Theorie der Kernmassen. *Zeitschrift fur Physik*, 96(7-8):431–458, July 1935.

[WHB+10] Andreas Wiens, Herbert Hess, Benedikt Birkenbach, Bart Bruyneel, Jürgen Eberth, Daniel Lersch, Gheorghe Pascovici, Peter Reiter, and Heinz-Georg Thomas. The agata triple cluster detector. *Nuclear Instruments and Methods in Physics Research Section A: Accelerators, Spectrometers, Detectors and Associated Equipment*, 618(1):223–233, 2010.

[Win] A. Winther. Winther A program GRAZING. http://personalpages.to.infn.it/~nanni/grazing/.

[Win94] A. Winther. Grazing reactions in collisions between heavy nuclei. *Nuclear Physics A*, 572(1):191–235, 1994.

[ZG13] V. I. Zagrebaev and Walter Greiner. Production of heavy trans-target nuclei in multi-nucleon transfer reactions. *Phys. Rev. C*, 87:034608, Mar 2013.

[Ziea] Eckert & Ziegler. Alpha Spectroscopy Sources. https://www.ezag.com/home/products/isotope_products/isotrak_calibration_sources/reference_sources/alpha_spectroscopy_sources/.

[Zieb] Eckert & Ziegler. Recommended Nuclear Decay Data: ^{152}Eu. https://www.ezag.com/fileadmin/ezag/user-uploads/isotopes/isotopes/Isotrak/isotrak-pdf/Decay_Schema_Data/Eu-152.pdf.

[ZKG15] Zagrebaev, V.I., Karpov, A.V., and Greiner, Walter. Synthesis of superheavy nuclei: Obstacles and opportunities. *EPJ Web of Conferences*, 86:00066, 2015.

[ZOIG06] V. I. Zagrebaev, Yu. Ts. Oganessian, M. G. Itkis, and Walter Greiner. Superheavy nuclei and quasi-atoms produced in collisions of transuranium ions. *Phys. Rev. C*, 73:031602, Mar 2006.

Title: Multinucleon transfer reactions in the ^{238}U + ^{238}U system studied with the VAMOS + AGATA + ID-Fix

Keywords: Multinucleon transfer reactions, heavy-ion reactions, reaction mechanism, superheavy nuclei, uranium

Neutron-rich light actinide nuclei near the N = 152 deformed shell closure are of special interest as they can yield important nuclear structure features related to shell effects and deformation. However, due to experimental challenges concerning production and identification, the data available on these nuclei are rather limited. The potential possibility to investigate neutron-rich nuclei in the region of our interest using multinucleon transfer (MNT) reactions has regained attention thanks to the improved performances of large acceptance magnetic spectrometers, e.g. the mass resolution of $\Delta A/A \simeq 1/263$ achieved at VAMOS++. Theoretically, cross sections of the order of a few tens of μbarn are predicted for MNT processes in collisions of actinide nuclei. This value, being beyond reach for other reaction mechanisms like fusion-evaporation, awaits experimental verification. Within this context, an experiment aiming to investigate the production cross sections of exotic neutron-rich heavy nuclei in the uranium region was carried out using reactions of ^{238}U + ^{238}U at 7.193 and 6.765 MeV/A. The measurement of the products was performed employing the VAMOS++ magnetic spectrometer for the atomic mass identification, the AGATA γ-ray spectrometer and the x-ray detection array ID-Fix for the identification of the atomic number through x-ray spectroscopy. The present manuscript reports on the work done for preparation of the detection setup as well as the analysis of the collected data and the obtained results of this experiment.

Titre: Réactions de transfert de multinucléons dans le système ^{238}U + ^{238}U étudiées avec VAMOS + AGATA + ID-Fix

Mots clés: Réactions de transfert de multinucléons, réactions d'ions lourds, mécanisme de réaction, noyaux superlourds, uranium

Les noyaux d'actinides légers riches en neutrons proches de la fermeture de couche déformée N = 152 présentent un intérêt particulier car ils peuvent fournir d'importantes informations sur la structure nucléaire associée aux effets de couche et à la déformation. Cependant, en raison des défis expérimentaux concernant la production et l'identification, les données disponibles sur ces noyaux sont plutôt limitées. La possibilité d'étudier les noyaux riches en neutrons dans la région qui nous intéresse en utilisant les réactions de transfert de multinucléons (MNT) a suscité un regain d'intérêt grâce à l'amélioration des performances des grands spectromètres magnétiques de larges acceptance, par exemple avec la résolution de masse de $\Delta A/A \simeq 1/263$ obtenue à VAMOS++. Théoriquement, des sections efficaces de l'ordre de quelques dizaines de μbarn sont prédites pour les processus MNT dans les collisions de noyaux d'actinides. Cette valeur, hors de portée pour d'autres mécanismes de réaction comme la fusion-évaporation, nécessite une vérification expérimentale. Dans ce contexte, une expérience ayant pour objectif d'étudier les sections efficaces de production de noyaux lourds exotiques riches en neutrons dans la région de l'uranium a été menée en utilisant la réaction ^{238}U + ^{238}U aux énergies de 7.193 et 6.765 MeV/A. La mesure des produits a été effectuée à l'aide du spectromètre magnétique VAMOS++ pour l'identification de la masse atomique, du spectromètre de photons γ AGATA et du système de détection de photons X ID-Fix pour l'identification du numéro atomique au moyen de la spectroscopie des rayonnements X. Le présent manuscrit rend compte du travail effectué pour la préparation du dispositif de détection ainsi que de l'analyse des données recueillies et des résultats obtenus dans le cadre de cette expérience.